Technical Physics Letters, Vol. 29, No. 5, 2003, pp. 353–356. Translated from Pis'ma v Zhurnal Tekhnicheskoĭ Fiziki, Vol. 29, No. 9, 2003, pp. 1–8.

The Surface Mode of a Dielectric Waveguide with Metal Substrate

D. G. Sannikov and D. I. Sementsov*

Ul'yanovsk State University, Ul'yanovsk, Russia

** e-mail: sementsovdi@ulsu.ru*

Received October 22, 2002

Abstract—The conditions of excitation and the waveguide characteristics are determined in an analytical form for the TM_0 mode of a planar waveguide with metal substrate. This mode has a surface character, in contrast to other (bulk) modes excited in the system. The propagation and damping constants and the energy flux density distributions are compared for the TM_0 and TE_0 modes. © *2003 MAIK "Nauka/Interperiodica".*

Introduction. The characteristics of waveguide and radiative modes in planar waveguide structures with absorption have been extensively investigated [1–5]. However, some features in the propagation and localization of guided modes in systems are still insufficiently studied. The presence of a complex component in the permittivity of one layer of a waveguide structure renders the waveguide mode propagation constant a complex quantity as well. As a result, the character of mode distribution in the structure cross section changes as compared to the case of a nonabsorbing waveguide [6]. Of special interest are the properties of surface modes, which are realized under certain conditions at the metal–dielectric interface [7].

The aim of this study was to determine the conditions for excitation of such a surface mode in a planar waveguide with metal substrate and to analyze by numerical methods the corresponding waveguide and energy characteristics.

Description of the model. Consider a planar waveguide structure comprising the metal substrate, the nonabsorbing waveguide layer, and the coating medium. The dielectric permittivities of the waveguide layer (ε_2) and the coating material (ε_3) are assumed to be real, while the substrate possesses a complex permittivity $\varepsilon_1 = (n + i\kappa)^2$ in the frequency range studied (where n is the refractive index and κ is the extinction coefficient) [8]. Let the structure be arranged so that the x axis is perpendicular to the boundaries between layers of the structure and the interface of the substrate and waveguide layers coincides with the plane $x = -L$, while the interface of the waveguide layer and coating medium coincides with the plane $x = 0$.

The electromagnetic field components of a waveguide mode propagating along the z axis can be presented in the following form:

$$F_\alpha(x, z, t) = \Phi_\alpha(x)\exp[i(\omega t - \beta z)], \quad \alpha = x, y, z, \quad (1)$$

where $\beta = \beta_1 + i\beta_2$ is the complex propagation constant and $\Phi_\alpha(x)$ are the components of the vector profile function describing the mode field distribution in the waveguide cross section. The real part (β_1) of the complex quantity β is usually called the propagation constant of the absorbing (amplifying) waveguide. The field component F_y denotes the electric field component E_y for a TE mode, and the magnetic field component H_y for a TM mode. In the waveguide geometry chosen, this component is transverse with respect to the propagation direction and tangential with respect to the layer boundaries. The corresponding component of the vector profile function is as follows:

$$\Phi_y(x) = A\begin{cases}\exp(-qx), & x \ge 0,\\ \left[\cosh x - \dfrac{\zeta q}{h}\sinh x\right], & -L \le x \le 0,\\ \left(\cosh L + \dfrac{\zeta q}{h}\sinh L\right)\exp[p(x + L)], & x \le -L,\end{cases} \quad (2)$$

where A is the normalization constant, $\zeta = 1$ for TE modes, and $\zeta = \varepsilon_2/\varepsilon_3$ for TM modes. In the case under consideration, the transverse components of the wave vector (p, h, and q) in each layer of the structure are complex quantities with the real and imaginary parts defined as

$$\begin{aligned}(p', h', q') &= \frac{1}{\sqrt{2}}[(u_j^2 + v_j^2)^{1/2} + u_j]^{1/2},\\ (p'', h'', q'') &= \pm\frac{1}{\sqrt{2}}[(u_j^2 + v_j^2)^{1/2} - u_j]^{1/2}.\end{aligned} \quad (3)$$

Here, the subscripts j = 1–3 in the right-hand part cor-

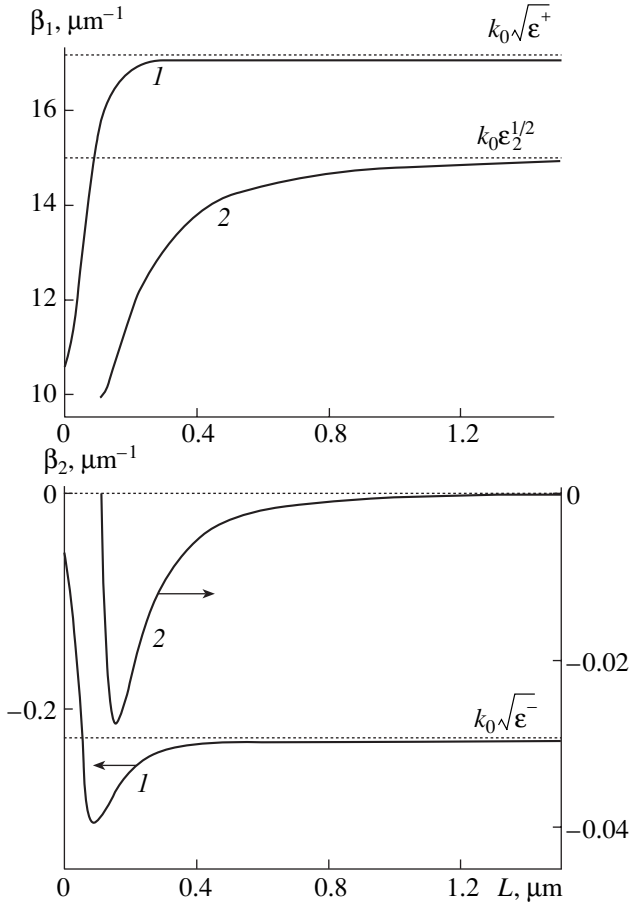

Fig. 1. Plots of the mode propagation constant β_1 and damping β_2 versus the waveguide layer thickness for the (*1*) TM_0 and (*2*) TE_0 modes.

respond to the parameters *p*, *h*, and *q*, respectively, and

$$u_j = (-1)^j(k_0^2\varepsilon_j' - \beta_1^2 + \beta_2^2),$$
$$v_j = (-1)^j(k_0^2\varepsilon_j'' - 2\beta_1\beta_2), \quad (4)$$

where $k_0 = \omega/c$ and *c* is the light speed in vacuum. For *z* components of the waveguide mode field, the Maxwell equations yield the following relations: $\Phi_z(x) = \pm(i/\gamma k_0)\frac{d\Phi_y}{dx}$, where the upper sign and $\gamma(x) = 1$ for all layers of the waveguide structure correspond to the H_z component of the TE modes, while the lower sign and $\gamma(x) = \varepsilon_j$ correspond to the E_z component of the TM modes.

The relation between the propagation constant of a given mode and the waveguide structure and radiation parameters is determined by a dispersion equation that coincides in form with the analogous equation for a nonabsorbing waveguide, except that the parameters *p*, *q*, *h* are complex:

$$hL = \arctan\left(\frac{\eta p}{h}\right) + \arctan\left(\frac{\xi q}{h}\right) + m\pi, \quad (5)$$

where $\eta = 1$ for TE modes and $\varepsilon_1/\varepsilon_2$ for TM modes.

Solution of the problem. An analysis of Eq. (5) shows that, in the waveguide regime, the mode propagation constants fall within an interval

$$(\beta_{1q}, \beta_{1p}) \le \beta_1 \le k_0\sqrt{\varepsilon_2}, \quad (6)$$

where

$$\beta_{1q} = k_0\sqrt{\varepsilon_3}, \ \beta_{1p} = (k_0/\sqrt{2})\sqrt{\varepsilon_1' + \sqrt{\varepsilon_1'^2 + \varepsilon_1''^2}}.$$

These conditions refer to the bulk waveguide modes characterized by zig-zag propagation in the ray approximation [2].

The waveguide properties of a nonabsorbing structure are lost under the cutoff conditions, whereby a bulk mode can be radiated into the substrate or coating. In addition, a mode becomes radiative provided that $h^2 \le 0$, in which case trigonometric solutions describing bulk modes in the waveguide layer change to hyperbolic solutions corresponding to the surface modes. However, for real positive ε_j, these solutions cannot obey the condition of continuity for tangential field components at the boundaries of the waveguide layer.

In the case when the substrate has a complex permittivity with negative real part ($\varepsilon_1' = n^2 - \kappa^2 < 0$), the solution of Eq. (5) corresponding to the TM wave with $m = 0$ describes a waveguide mode of the surface type. In contrast to the bulk modes (for which $\beta_1^2 - \beta_2^2 < k_0^2\varepsilon_2$), the surface modes must no longer obey conditions (6) and can meet the condition $\beta_1^2 - \beta_2^2 > k_0^2\varepsilon_2$, for which a TM_0 mode region with $\beta_1 > k_0\sqrt{\varepsilon_2}$ appears in the dispersion curve describing the mode propagation constants. The main parameters of this mode can be determined from Eq. (5) upon replacing *h* with *ih*. Unlike the bulk modes, this surface mode has no finite cutoff thickness. For $L = 0$, the real and imaginary parts of the propagation constant obey the relation

$$(\beta_{10}^s, \beta_{20}^s) = k_0\sqrt{\varepsilon_3/2g}(\sqrt{a^2 + b^2} \pm a)^{1/2}, \quad (7)$$

where $g = |\varepsilon_1|^2 + 2\varepsilon_1'\varepsilon_3 + \varepsilon_3^2$, $a = \varepsilon_1'\varepsilon_3 + |\varepsilon_1|^2$, and $b = \varepsilon_1''\varepsilon_3$ (the signs plus and minus refer to β_{10}^s and β_{20}^s, respectively). For $L \longrightarrow \infty$, the real and imaginary parts

of the propagation constant asymptotically tend to the values $\beta^s_{1\infty}$ and $\beta^s_{2\infty}$, which can be determined using relation (7) with ε_3 replaced by ε_2.

Results and discussions. Figure 1 presents the plots of the propagation constant β_1 and the mode damping β_2 for the surface (TM_0, curve *1*) and the bulk (TE_0, curve *2*) modes versus waveguide layer thickness L, which reveal a difference in the behavior of these modes. The curves were constructed using a numerical solution of Eq. (5) for the following values of the waveguide structure and radiation parameters: $\varepsilon_1 = (0.15 - i \times 3.2)^2$, $\varepsilon_2 = 2.30$, $\varepsilon_3 = 1.00$; these values correspond to real waveguide structures with metal (Au, Cu) substrates and a glass-based waveguide layer for a wavelength of $\lambda = 0.6328$ μm [1, 2]. As can be seen from these data, the bulk mode (TE_0) exhibits a cutoff at $L \cong 0.11$ μm that corresponds to the appearance of a radiative mode in the coating material. The surface mode (TM_0) has no cutoff: the propagation constant and mode damping for $L \longrightarrow 0$ are determined by relations (7). As the waveguide layer thickness increases, the real part of the propagation constant asymptotically tends to $k_0\sqrt{\varepsilon_2}$ for the TE_0 mode and to $k_0\sqrt{\varepsilon^+}$ for the TM_0 mode, where $\varepsilon^+ > \varepsilon_2$. The mode damping sharply increases in the region of small waveguide layer thickness, passes through a maximum, and then decreases to zero for the TE_0 mode and to $k_0\sqrt{\varepsilon^-}$ for the TM_0 mode. Here,

$$\varepsilon^{\pm} = \frac{\varepsilon_2}{2}\left(\frac{\sqrt{(\varepsilon_1'\varepsilon_2 + |\varepsilon_1|^2)^2 + (\varepsilon_1''\varepsilon_2)^2} \pm \sqrt{(\varepsilon_1'\varepsilon_2 + |\varepsilon_1|^2)}}{(\varepsilon_1' + \varepsilon_2)^2 + (\varepsilon_1'')^2}\right) \quad (8)$$

and, for the parameters indicated above, $\beta^s_{1\infty} \cong 17.08$ μm^{-1} and $\beta^s_{2\infty} \cong -0.23$ μm^{-1}. A minimum difference in damping between the TM_0 and TE_0 modes takes place in the region of small thicknesses L. A mode decays e times upon traveling a distance of $l = 1/\beta_2$ (characteristic pathlength [7]). Near the cutoff, the surface mode has a maximum pathlength on the order of 18 μm. For the maximum damping, the l values for the TM_0 and TE_0 modes are estimated at 3.3 and 36.3 μm, respectively; these pathlengths differ most significantly far from the cutoff (at large L values), reaching 4.3 and 1923 μm, respectively.

The energy flux distribution in the waveguide cross section is described by the expression $\mathbf{S} = (c/8\pi)\mathrm{Re}[\mathbf{EH}^*]$. Taking into account the waveguide geometry and the configuration of fields **E** and **H**, the z component of this energy flux can be expressed as

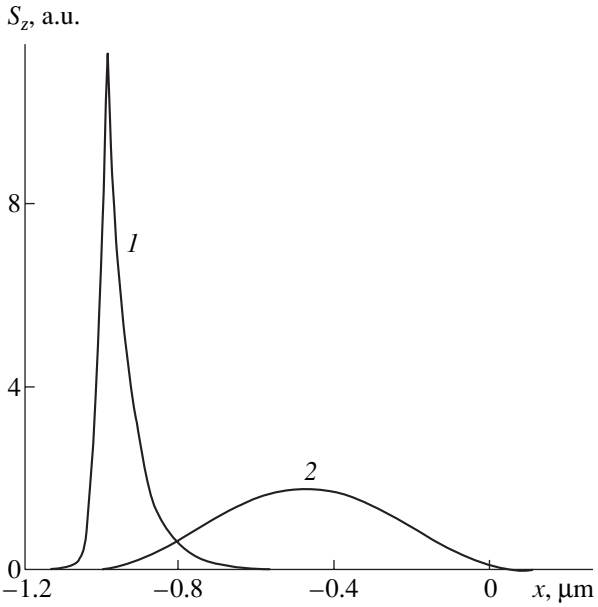

Fig. 2. The normalized energy flux distribution in the waveguide cross section for the (*1*) TM_0 and (*2*) TE_0 modes.

$$S_z(x) = \frac{c}{8\pi k_0} S_0 \Phi_y^2(x) \mathrm{Re}\left(\frac{\beta}{\gamma}\right), \quad (9)$$

where S_0 is the energy flux density (per unit length in the y axis) entering the waveguide. Figure 2 shows the normalized energy flux distribution along the z axis for the TM_0 (curve *1*) and TE_0 (curve *2*) modes of a waveguide with $L = 1$ μm. As can be seen, the TM_0 mode energy is localized at the metal–dielectric interface, whereas the TE_0 mode field distribution exhibits a pronounced volume character with localization inside the waveguide layer.

An analysis of expression (9) shows that, for the waveguide structure and medium parameters, the energy flux density maximum for the bulk mode takes place at $x_m \approx -0.47$ μm (which corresponds to the center of the waveguide layer), and for the surface mode, at $x_m = -1$ μm (the mode is localized at the metal–dielectric interface). The degree of localization can be evaluated as

$$\Gamma(x_m) = \int_{x_m - \Delta x}^{x_m + \Delta x} S_z(x)dx \Big/ \int_{-\infty}^{\infty} S_z(x)dx,$$

where x_m is the coordinate of the energy flux density maximum of a given mode. This expression yields $\Gamma(x_m) = 99.99$ and 34.80% at $\Delta x = 0.1$ μm and 91.10 and 3.57% at $\Delta x = 0.01$ μm for the surface and bulk modes,

respectively. The analysis showed that the energy flux density distribution of the TM_0 mode in a waveguide with small L (such that $\beta_1^s < k_0\sqrt{\varepsilon_2}$) is essentially the same as that presented above, so that the mode retains a surface character.

REFERENCES

1. A. Reisinger, Appl. Opt. **12** (5), 1015 (1973).
2. M. Adams, *Introduction to Optical Waveguides* (Wiley, New York, 1981; Mir, Moscow, 1984).
3. D. G. Sannikov and D. I. Sementsov, Pis'ma Zh. Tekh. Fiz. **28** (20), 42 (2002) [Tech. Phys. Lett. **28**, 857 (2002)].
4. Sh. She, J. Wang, and L. Qiao, Opt. Commun. **90** (4–6), 238 (1992).
5. J. Xiaoqing, Y. Jianjyi, and W. Minghua, Opt. Commun. **129** (3–4), 173 (1996).
6. J.-J. Claire, *Introduction to Integrated Optics* (Sov. Radio, Moscow, 1980).
7. J. J. Burke, G. L. Stegeman, and T. Tamir, Phys. Rev. B **33**, 5186 (1986).
8. M. Born and E. Volf, *Principles of Optics* (Pergamon, Oxford, 1969; Nauka, Moscow, 1973).

Translated by P. Pozdeev

Technical Physics Letters, Vol. 29, No. 5, 2003, pp. 357–360. Translated from Pis'ma v Zhurnal Tekhnicheskoĭ Fiziki, Vol. 29, No. 9, 2003, pp. 9–17.

The Structure of a Turbulent Boundary Layer

L. N. Pyatnitsky

Associated Institute for High Temperatures, Russian Academy of Sciences, Moscow, Russia

e-mail: pyat7@mail.ru

Received November 25, 2002

Abstract—According to the wave mechanism of turbulence, pulsation in the hydrodynamic parameters results from a superposition of perturbations arising at the wall and then spreading in the flow in the form of spherical wave packets. At the flow boundary, where the fluid velocity is characterized by a large gradient, the acoustic rays of these waves exhibit bending and reversal toward the wall, whereby the trajectories with various initial orientations are interweave and the wave packets are broken. The pulsation of parameters in the region of wave packet breakage results in the formation of a turbulent boundary layer. Upon the reflection of waves, the flow velocity oscillations immediately at the wall cease that corresponds to a laminar sublayer of the turbulent boundary layer. *© 2003 MAIK "Nauka/Interperiodica".*

The motion of a fluid in the boundary layer of a turbulent flow can be studied based on the Prandtl equations (see, e.g., [1]), which provide for a good description of averaged values of the hydrodynamic parameters. A closed system of equations for the laminar boundary layer is obtained using Newton's law of friction, in which the coefficient of viscosity η is determined by the momentum transfer across the flow as a result of the molecular collisions. In particular, $\eta = \rho\lambda v/3$ in gases, where λ and v are the mean free path and the thermal velocity of molecules, respectively.

However, the molecular mechanism of momentum transfer cannot describe oscillations in the hydrodynamic parameters observed in a turbulent boundary layer. In order to describe this phenomenon, the coefficient η is replaced by the turbulent exchange coefficient A_t, and the mean free path λ, by the turbulent exchange pathlength L [2]. In this formal approach, the momentum transfer is generally not related to any physical processes. However, in real liquids and gases, the momentum transfer can take place by means of wave propagation during the evolution of perturbations. It should be noted that the wave equation, as well as the Prandtl equations, follow from the Navier–Stokes equations and the continuity conditions.

Previously [3, 4], the wave mechanism of pulsation was experimentally justified and the concept of turbulence was formulated. This concept is based on the notion of perturbations in the hydrodynamic parameters arising in the region of flow drag at the wall. These perturbations propagate in the flow in the form of wave packets, the superposition of which leads to the formation of a spatiotemporal field of oscillating parameters. A similar process of wave generation and superposition takes place during the motion of bodies over the surface of a liquid.

The problem of describing the evolution of perturbations in a resting unbounded medium is well known. Following [6], let a perturbation represent a ball of radius $r \le a$ possessing an excess density of $f(r)$. The perturbation spreads at the speed of sound c in the form of a spherical wave packet with a thickness of $2a$, traveling over a distance of l for the time t. Within the limits of the packet, $|l - ct| \le a$, the velocity, pressure, and other parameters (u, p, ρ, etc.) exhibit pulsation in accordance with the shape of the function $f(r)$. The amplitude of this pulsation is inversely proportional to the distance traveled by the wave:

$$u, p, \rho \sim f\left(\frac{l-ct}{a}\right)\frac{1}{l}. \quad (1)$$

The motion of a medium in a channel of finite cross section produces deformation of the wave front. This is related, first, to the wave reflections from the wall and, second, to a complicated wave velocity profile in the channel cross section. The methods for calculating the spatiotemporal field of oscillating parameters in the flow core, the structure, and the behavior of pulsation with allowance for the reflections from boundaries were described in [5].

For comparison, Fig. 1a shows the configurations of waves spreading in a half-space $z > 0$ and in a flat channel of height d formed by two parallel plane walls. In both cases, the wave center is situated at the point $\mathbf{rp}(xp, yp, zp)$ (in our case, $yp = zp = 0$). In the half-space, the wave front position relative to the center $\mathbf{rp}$ is described by the radius vector $\mathbf{r}(\xi, \eta, \zeta)$. Moving in the channel, the wave exhibits repeated reflections from the walls, which gives rise to a pattern of gradually decaying pulsation (Fig. 1b) at the point of observation $\mathbf{r}_0(x, y, z)$. It is the superposition of such waves that produces an impression of a chaotic pulsation, although the process in fact does not possess this character.

1063-7850/03/2905-0357$24.00 © 2003 MAIK "Nauka/Interperiodica"

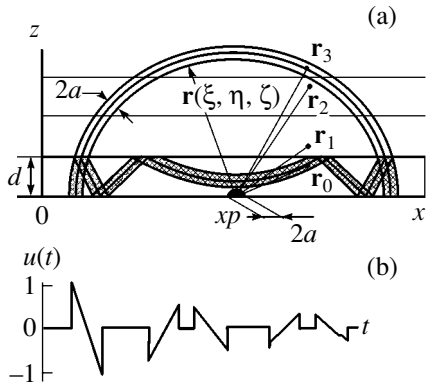

Fig. 1. Schematic diagrams showing (a) the wave configuration in a flat channel and (b) the pattern of velocity oscillations at a given point of observation r_0.

Let us study how the character of pulsation depends on the wave velocity profile in the channel cross section. The wave velocity is given by the well-known formula $\mathbf{V} = \partial\omega/\partial\mathbf{k}$, where $\mathbf{k}$ is the wavevector and $\omega(\mathbf{k})$ is the dispersion law. For a medium moving at a velocity $\mathbf{U}$, the dispersion law is described by a simple relation

$$\omega = ck + \mathbf{U}\mathbf{k}. \tag{2}$$

Let $\mathbf{s}$ be a unit vector in the direction of wave propagation at the point $\mathbf{r}$, which is equivalent to an acoustic ray in terms of the geometric acoustics. The change in the ray direction at this point is described by the equation [6]

$$\frac{d\mathbf{s}}{dl} = \frac{1}{c}[\mathrm{curl}\,\mathbf{U}, \mathbf{s}], \tag{3}$$

where dl is the element of the ray trajectory.

For a resting medium, $\mathbf{U} = 0$ and $\mathbf{V} = c\mathbf{k}/k$. Accordingly, $\mathbf{s} = \mathbf{r}/r$, so that a given point of the wave moves along a straight line and the wave remains spherically symmetric. If the medium moves at a constant velocity ($\mathbf{U} = \mathrm{const}$), then $\mathbf{V} = c\mathbf{k}/k + \mathbf{U}$ and the direction of vector $\mathbf{s}$ remains unchanged: the wave is translated as a whole with the flow, also retaining the spherical symmetry. Under these conditions, we consider the process of wave propagation in the flow core, where the velocity can be regarded as constant to the first approximation. However, we cannot ignore the change in the flow velocity $\mathbf{U}$ at the wall. Let us estimate the total angle of the acoustic ray rotation in this region of the field $U(z)$ according to Eq. (3).

Let the flow in the flat channel be directed along the x axis. We will assume that the flow velocity depends only on the coordinate z and increases with the distance from the wall: $U = 0$ and $dU/dz > 0$ at $z = 0$. Denoting the initial acoustic ray direction by subscript 0 and integrating Eq. (3), we obtain the following expressions for the components of vector $\mathbf{s}$ ($U \ll c$):

$$\begin{aligned} s_x &= s_{x0} + M(z), \quad s_y = s_{y0}, \\ s_z &= \sqrt{1 - s_x^2 - s_y^2}, \quad M(z) = \frac{U(z)}{c}. \end{aligned} \tag{4}$$

In order to simplify the formulas, let us restrict the consideration to the acoustic rays in the vertical cross section with an azimuthal angle of $\varphi = 0$ and a polar angle of $\vartheta \in [-\pi/2, \pi/2]$. The average velocity in a turbulent flow can be expressed as

$$\begin{aligned} U(z) &= U_0[4z(1-z)]^{1/m} \\ \text{or} \quad M(z) &= M_0[4z(1-z)]^{1/m}, \end{aligned} \tag{5}$$

where U_0 is the velocity in the middle of the channel (between the two walls), M_0 is the average Mach number, and m is a parameter characterizing the flow regime: $m = 1$ for the laminar flow, $m \gg 1$ (e.g., $m = 5$, 10, etc.) for a turbulent flow, and $m = \infty$ in the case of a constant flow velocity across the channel. Selecting the angle $\varphi = 0$, expressing the components of vector $\mathbf{s}$ through the polar angle ϑ and using formulas (4) and (5), we arrive at the relation

$$\vartheta = \arcsin(\sin\vartheta_0 + M_0[4z(1-z)]^{1/m}). \tag{6}$$

Relation (6) allows us to obtain a differential equation describing the ray trajectory in an explicit form as $z(x)$ and the parametric differential equations determining the ray pathlength l to the point of observation with the coordinates $\{x, z\}$:

$$dz/dx = 1/\tan\vartheta(z, \vartheta_0, M_0, m), \tag{7}$$

$$\begin{aligned} \frac{dx}{dl} &= \sin\vartheta(z, \vartheta_0, M_0, m), \\ \frac{dz}{dl} &= \cos\vartheta(z, \vartheta_0, M_0, m). \end{aligned} \tag{8}$$

The corresponding boundary conditions are as follows: $z(0) = 0$, $(dz/dx)|_{x=0} = 1/\tan\vartheta_0$; and $x(0) = z(0) = 0$, $(dx/dl)|_{l=0} = \sin\vartheta_0$, $(dz/dl)|_{l=0} = \cos\vartheta_0$. Thus, under otherwise equal conditions, the ray orientation and the direction of pulsation depend on the initial angle ϑ_0: the greater $|\vartheta_0|$, the stronger the deviation. In the direction opposite to the flow ($\vartheta_0 < 0$), the beam trajectory deviates from the wall; otherwise ($\vartheta_0 > 0$), the trajectory deviates toward the wall. There is a certain initial angle $\vartheta_0 = \vartheta_*$ for which $\vartheta = \pi/2$ and the ray never deviates from the wall by a distance exceeding a certain finite value z_*. Past the maximum z_*, the ray declines toward the wall again, thus following an arclike trajectory, of a cyclic kind. Since the angle of incidence $-\vartheta$ in this cycle is equal to the angle of reflection, this character is retained until the wave damping.

Under the condition $\vartheta = \pi/2$, formula (6) describes the dependence of z_* on the angle ϑ_* and the flow parameters m and M_0 (the minus sign corresponds to the bottom wall):

$$z_* = \frac{1}{2}\left(1 - \sqrt{1 - \left(\frac{1 - \sin\vartheta_*}{M_0}\right)^m}\right). \qquad (9)$$

Note that the M_0 value depends on the parameter m. For example, the Reynolds number for an air flow in a flat channel of height $d = 1$ cm reaches a critical level at $M_0 \approx 0.01$. Therefore, a laminar flow ($m = 1$) corresponds to the interval of $M_0 \in [0, 0.01]$, while a turbulent regime ($m \gg 1$) takes place for $M_0 > 0.01$. For $m = 1$, a cyclic ray motion proceeds within a small sector $\vartheta_* > 85°$, whereas for $m \gg 1$, the sector may expand to $\vartheta_* > 60°$. In addition, as m increases, the function $z_*(m, M_0, \vartheta_*)$ exhibits more sharp variations.

Each value of z_* corresponds to a certain limiting angle ϑ_* (depending on m and M_0). Figure 2 shows the ray trajectories for a flow with the parameters $m = 5$, and $M_0 = 0.05$ (with the limiting angles ϑ_* indicated for the trajectories passing through the maximum values of $z_* = \{0.484, 0.463, 0.422, 0.341, 0.186, 0.075\}$).

The surface $z_*(m, M_0, \vartheta_*)$ determines a region of the initial beam orientations, $-\pi/2 \le \vartheta_0 < \vartheta_*$, which z_* cannot take real values. In this region, the rays freely reach any point $z > z_*$, at which the superposition of perturbations leads to the formation of a spatiotemporal field of oscillating hydrodynamic parameters. This field, while being analogous to that formed in the flow core, possesses certain characteristic features. Figure 3, illustrating these peculiarities for a flow with $M_0 = 0.05$ and $m = 5$, shows the ray trajectories (with neglect of reflected waves) passing through two observation points, $\{x, z\} = \{0, 0.5\}$ and $\{0, 0.1\}$, at different distances from the wall. As can be seen from these plots, the interval of xp in which the waves whose acoustic rays produce perturbations at the indicated observation points are generated is relatively small and is axisymmetric with respect to $x = 0$. The upstream part (xp^-, with $xp < 0$) of this interval is significantly greater than the downstream part (xp^+, with $xp > 0$). The $M(z)$ profile is manifested by that the perturbations from xp^+ points increase the u_z pulsation component, while those from xp^- increase the u_x component. Therefore, allowance of the flow velocity profile leads to the pulsation being predominantly oriented along the flow.

Let us compare the process of pulsation for the points occurring at various heights. The region of parameter xp^+ in both cases is limited by the angle $\vartheta_0 = -\pi/2$, while differences are related to the parameter xp^-. For the observation point at $\{x, z\} = \{0, 0.5\}$, the xp^- values are limited by the angle $\vartheta_* = 71.8°$ ($z = z_* = 0.5$).

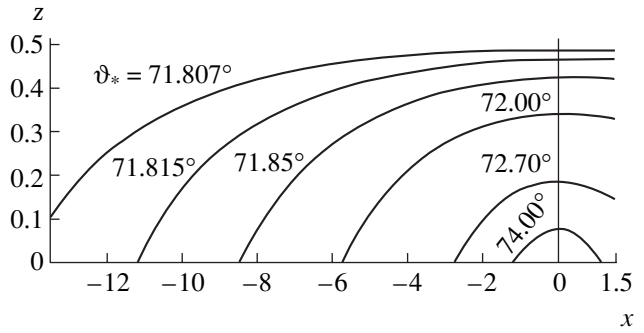

Fig. 2. Ray trajectories for various limiting angles ϑ_* in a flow with $m = 5$ and $M_0 = 0.05$. The value of ϑ_* correspond to $z_* = \{0.075, 0.186, 0.341, 0.422, 0.463, 0.484\}$.

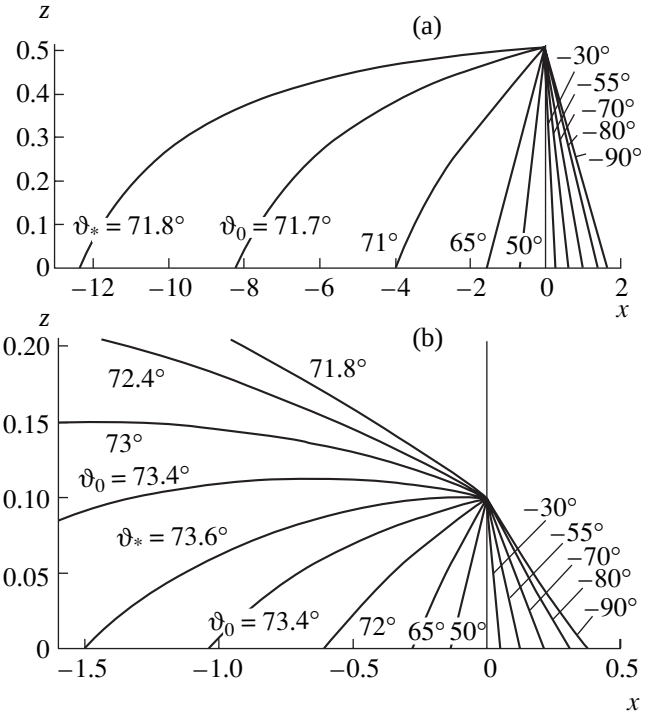

Fig. 3. Ray trajectories passing via observation points $\{x, z\} = \{0, 0.5\}$ (a) and $\{0, 0.1\}$ (b).

The process of pulsation at $\{x, z\} = \{0, 0.1\}$, where the limiting angle is $\vartheta_* = 73.6°$, is also influenced by perturbations whose acoustic rays pass via the points situated above the level of $z_* = 0.1$. In the interval $z_* \in [0.1, 0.5]$, these points correspond to the angles $\vartheta_* \in [73.6°, 71.8°]$. Therefore, the u_x component increases further on approaching the wall. This agrees with the experimental results obtained by H. Reihardt and P.S. Klebanov (see [2, Ch. 18, §4]).

Now consider the propagation of perturbations within a narrow interval of $z \in [0. 0.1]$ for rays with initial directions $\vartheta_0 = \{70°, 73°, 75°, 76°, 77°\}$. Figure 4 shows the corresponding trajectories for a flow with the

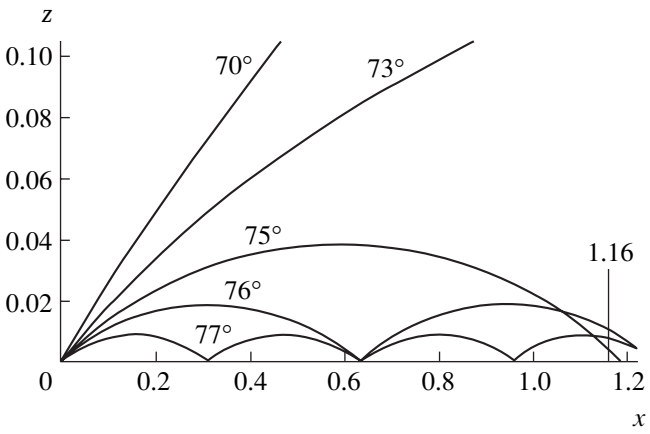

Fig. 4. The pattern of acoustic rays propagating near the wall for $\vartheta_0 = 70°$, 73°, 75°, 76°, and 77°.

same parameters ($m = 5$, $M_0 = 0.05$). As is clear from the above examples, the ray with $\vartheta_0 = 70°$ (retaining the initial direction almost unchanged) goes to the flow core. The ray with $\vartheta_0 = 73°$ follows a cyclic trajectory with $z_* \approx 0.15$ and $l \approx 4.5$. Over this length, the initial perturbation decays almost completely, and the ray trajectory appears at a vortexlike arc. The separated layer only retains the rays with $\vartheta_0 = \{75°, 76°, 77°\}$ and a pathlength of $l \approx 1.2$.

Depending on the initial angle ϑ_0, a trajectory with $l = 1.2$ contains two to four cycles, so that the rays due to the same perturbation exhibit interweaving. For example, the cross section at $x = 1.16$ shows a sequence of 75°–77°–76° rays instead of the anticipated order 77°–76°–75°. Of course, the value of ϑ_0 in a wave varies continuously, so that complete interweaving of the rays takes place in the layer with a height of $z_*(75°) \approx 0.04$ ($\vartheta_0 \in [75°, 90°]$). The interaction between waves in this layer leads to the formation of a spatiotemporal field of oscillating parameters. This field, while being analogous to that in the flow core, is formed via a different mechanism. Indeed, the approximation of geometric acoustics and the acoustic ray concept are no longer applicable and the pattern of pulsation should be calculated using the Kirchhoff–Fresnel integral. Taking this into account, the layer with a height of $z_*(75°) \approx 0.04$ can be considered as the boundary layer.

The pulsation of velocity in a wave packet is related to an energy flux of $c\rho u^2$. When the wave is reflected from a wall, the rate of pulsation is zero within a narrow layer near the wall. The energy of pulsation is transferred to that of oscillations in the pressure and density. In the absence of velocity oscillations, this layer can be considered as a laminar sublayer of the turbulent boundary layer. The corresponding height δ varies within $(0.1– 0.2)a$, depending on the form of the $f(r)$ function.

According to the wave mechanism of turbulence, the spatiotemporal field of oscillating hydrodynamic parameters is formed as a result of the superposition of perturbations arising at the wall and propagating in the form of wave packets. In the flow core, where the gradients of parameters can be considered as negligibly small, this field represents a superposition of spherical wave packets. In the zone where the gradients of parameters are significant, the trajectories of acoustic rays exhibit reflection from the wall and interweaving, the spherical wave front no longer exists, and the approximation of geometric acoustics becomes inapplicable. A change in the mechanism of pulsation and predominantly longitudinal orientation of the oscillations determine the formation of a boundary layer. A decrease in magnitude of the wave velocity pulsation during reflection leads to the formation of a laminar sublayer in the turbulent boundary layer. The main parameter influencing the properties of a boundary layer is the Mach number (despite the condition that $M_0 \ll 1$).

REFERENCES

1. H. Schlichting, *Grenzschicht–Theorie* (V.G. Braun, Karlsruhe, 1960; Nauka, Moscow, 1969).
2. L. Prandtl, Über Flüssigkeitsbewegung bei sehr kleiner Reibung, *Int. Math. Kongr., Heidelberg, 1904*, Verhandlg. III, pp. 484–491.
3. L. N. Pyatnitsky, Zh. Éksp. Teor. Fiz. **113**, 191 (1998) [JETP **86**, 107 (1998)].
4. L. N. Pyatnitsky, Phys. Vibr. **8** (3), 185 (2000).
5. L. N. Pyatnitsky, Zh. Éksp. Teor. Fiz. **119**, 665 (2001) [JETP **92**, 576 (2001)].
6. L. D. Landau and E. M. Lifshits, *Course of Theoretical Physics*, Vol. 6: *Fluid Mechanics* (Nauka, Moscow, 1988; Pergamon, New York, 1987).

Translated by P. Pozdeev

Technical Physics Letters, Vol. 29, No. 5, 2003, pp. 361–363. Translated from Pis'ma v Zhurnal Tekhnicheskoĭ Fiziki, Vol. 29, No. 9, 2003, pp. 18–23.

The Barkhausen Effect and Percolation Threshold in Amorphous Metal–Dielectric Nanocomposites

Yu. E. Kalinin[a], A. V. Sitnikov[a], N. E. Skryabina[b], L. V. Spivak[b,*], and A. A. Shadrin[b]

[a] *Voronezh State Technical University, Voronezh, Russia*

[b] *Perm State University, Perm, Russia*

* *e-mail: levspivak@permonline.ru*

Received November 29, 2002

Abstract—A new percolation situation has been found in metal–dielectric nanocomposites containing ferromagnetic components. For a certain concentration of metal atoms, the vectors of spontaneous magnetization of individual nanoparticles exhibit a correlated behavior. As a result, a structure containing a very large number of ferromagnetic nanoparticles shows magnetization reversal in a macroscopic nanocomposite volume in a single giant Barkhausen jump. © *2003 MAIK "Nauka/Interperiodica".*

Introduction. In recent years, much attention has been given to the properties of condensed media with a characteristic size of the structural components (granules) comparable with interatomic distances. Examples are offered by nanocrystalline fractal aggregates, nanocomposites, etc. The properties of such systems are determined to a considerable extent by the character of interfaces and the size of granules rather than by the properties of alloys and other structural elements [1, 2].

Anomalous physical properties (magnetic, optical, magnetooptical, etc.) were mostly observed in granulated composites with a metal phase concentration near the percolation concentration (X_c), at which metal nanoparticles form a conducting cluster structure in the dielectric matrix [3–7]. This threshold eventually determines the possibility of obtaining a granulated metal–dielectric nanocomposite possessing a unique combination of physical properties. The accuracy of determination of the percolation threshold is among the most important factors of progress in this direction of science and technology.

The results of experimental and theoretical investigations into the magnetic properties of ferromagnetic metal–dielectric nanocomposites show that compositions with a metal phase concentration below the percolation threshold exhibit superparamagnetic properties at room temperature. A nanodimensional metal granule is considered as a ferromagnetic particle possessing an intrinsic magnetic moment equal to the sum of magnetic moments of the atoms contained in this granule. If the energy of the magnetostatic interaction between granules is below kT, no correlation between the magnetization vectors of such particles takes place, and the composite exhibits paramagnetic properties. When an infinite network of contacting granules is formed, conditions favoring exchange interaction between atoms of the neighboring granules are created, and the material acquires ferromagnetic properties [6].

Methods used to determine the percolation threshold in materials of this type are quite traditional and usually consist in constructing a plot of the electric resistance versus sample composition, which exhibits a characteristic bending at the corresponding point. To our knowledge, the Barkhausen effect (offering an effective means of studying amorphous metal alloys [7–9]) has never been used for the analysis of the magnetic structure of nanocrystalline composites of the type under consideration.

Experimental. The samples of nanocomposites of the metal alloy–dielectric type were prepared by ion beam sputter deposition [10]. The amorphous nanocomposites were deposited upon sputtering a fused composite target made of a $Co_{41}Fe_{39}B_{20}$ compound with aluminum oxide plates (~2 mm thick and ~9 mm wide) fixed on the target surface perpendicularly to its longitudinal axis. By nonuniformly varying the distances between plates, it was possible to control smoothly the volume ratio of sputtered magnetic and dielectric phases in the deposit, thus obtaining a continuous spectrum of sample compositions in a single technological cycle.

The resistivity of samples was measured using a potentiometric technique. The Barkhausen effect was measured in a special setup with an external magnet generating magnetic field in the sample bulk. The Barkhausen transducer was a measuring coil, which detected the magnetic flux variations due to the Barkhausen jumps and converted this signal into the Barkhausen emf ε_B. The frequency of magnetic field switching was 50 Hz. The magnetic field was applied

1063-7850/03/2905-0361$24.00 © 2003 MAIK "Nauka/Interperiodica"

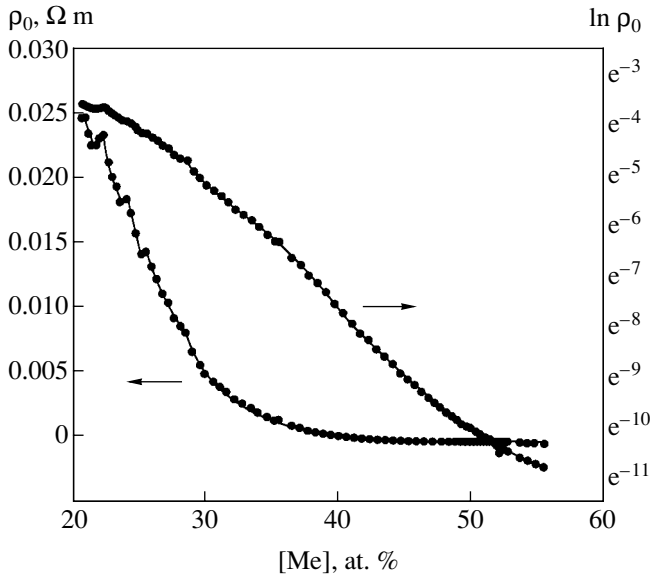

Fig. 1. Plots of the electric resistivity versus metal content in the composite material studied.

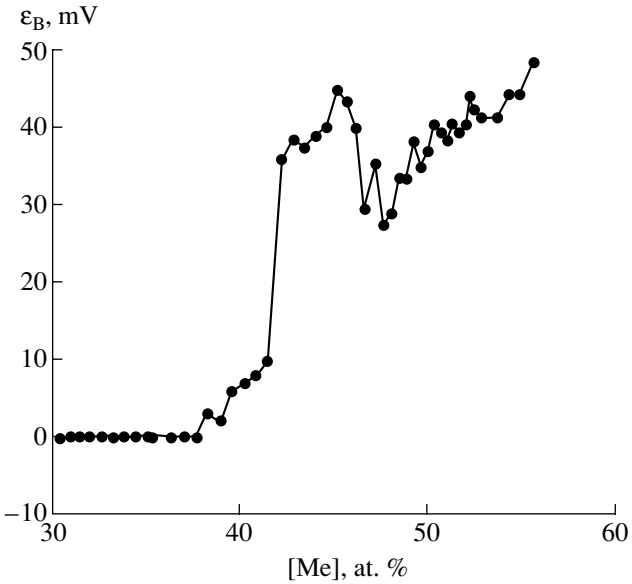

Fig. 2. Integral value of the Barkhausen emf ε_B versus metal content in the composite material studied.

along the composite axis. The sample bulk magnetization reversal exhibited a homogeneous character. The separate Barkhausen jumps and other changes were monitored using a PCS641 oscilloscope. The experimental data were processed using a special computer software. The structure of amorphous nanocomposites was studied by electron microscopy.

Results and discussion. Figure 1 presents data on the effect of the metal concentration on the resistivity ρ_0, plotted on both a linear and a logarithmic scale. As can be seen, this plot does not provide for unambiguous determination of the percolation threshold, despite the fact that the resistivity changes by several orders of magnitude upon transition via this threshold.

The structure of separate Barkhausen jumps observed during the magnetization reversal in composites with various concentrations of metal atoms shows evidence of a magnetic structure featuring the same or close orientations of the spontaneous magnetization of granules. As the metal content increases, the structure of jumps becomes more complicated, showing small satellites on both sides of a giant Barkhausen magnetization jump. In our samples, the volume of the composite material involved in the magnetization reversal process was on the order of 0.2 mm^3. According to the electron-microscopy data, the size of granules did not exceed 10 nm. Therefore, the process of magnetization reversal involved 10^{17}–10^{18} granules. This is a manifestation of an unusual situation. A synchronous behavior of the spontaneous magnetization vectors of individual nanoparticles is evidence of a new percolation situation related to a certain mechanism ensuring the collective and self-consistent response in a very large number of virtually immobile particles, rather than a change in the electric conductivity type, in response to the external magnetic field. As a result, the spontaneous magnetization vectors of these particles rotate synchronously with the applied field, and the entire aggregation of ferromagnetic particles behaves as a single macroscopic magnetic domain.

A necessary conclusion from the above results is that the Barkhausen jumps observed in the system studied are related to more complicated factors (e.g., the Néel mechanism), rather than to a jumplike displacement of magnetic domain boundaries. The transition of the composite material into this new state takes place within a rather narrow and sufficiently exactly determined interval (about $X_c \approx 43$ at. %) of metal concentrations (Fig. 2). However, the proposed method of determining the percolation threshold is also sensitive to the initial stages of the percolation cluster formation (beginning at $X_c \approx 38$ at. %), where separate magnetic aggregates tend to form and grow with increasing metal content.

Thus, we have observed a new percolation situation related to collective rotation of the spontaneous magnetization vectors of individual nanoparticles involved entering into a percolation cluster in a granulated metal–dielectric nanocomposite. It was shown that the Barkhausen effect can be used as an alternative method of determining the percolation threshold in composites containing ferromagnetic nanoparticles.

REFERENCES

1. Yu. E. Kalinin, S. B. Kushchev, P. V. Neretin, *et al.*, Zh. Prikl. Khim. **73**, 439 (2000).

2. I. V. Zolotukhin, B. G. Sukhodolov, A. S. Andreenko, *et al.*, Pis'ma Zh. Éksp. Teor. Fiz. **66**, 556 (1997) [JETP Lett. **66**, 594 (1997)].
3. I. V. Bykov, E. A. Gan'shina, A. B. Granovskiĭ, and V. S. Gushchin, Fiz. Tverd. Tela (St. Petersburg) **42**, 487 (2000) [Phys. Solid State **42**, 498 (2000)].
4. Yu. E. Kalinin, A. V. Sitnikov, O. V. Stognei, *et al.*, Mater. Sci. Eng. **304-306**, 941 (2001).
5. E. A. Gan'shina, A. B. Granovskiĭ, B. Dieny, *et al.*, Fiz. Tverd. Tela (St. Petersburg) **42**, 1860 (2000) [Phys. Solid State **42**, 1911 (2000)].
6. O. V. Stognei, Yu. E. Kalinin, A. V. Sitnikov, *et al.*, Fiz. Met. Metalloved. **91** (1), 24 (2001).
7. N. E. Skryabina, L. V. Spivak, A. S. Kinev, *et al.*, Pis'ma Zh. Tekh. Fiz. **26** (21), 26 (2000) [Tech. Phys. Lett. **26**, 947 (2000)].
8. L. V. Spivak and A. S. Kinev, Vestn. Perm. Univ., Ser. Fiz., No. 6, 9 (2000).
9. N. E. Skryabina, L. V. Spivak, A. S. Kinev, and N. V. Pimenova, Materialovedenie, No. 6, 29 (2001).
10. Yu. E. Kalinin, A. T. Ponomarenko, A. V. Sitnikov, *et al.*, Fiz. Khim. Obrab. Mater., No. 5, 14 (2001).

Translated by P. Pozdeev

Technical Physics Letters, Vol. 29, No. 5, 2003, pp. 364–366. Translated from Pis'ma v Zhurnal Tekhnicheskoĭ Fiziki, Vol. 29, No. 9, 2003, pp. 24–28.

A Bidirectional Ring Fiber Laser with a 90° Faraday Rotator as the Nonreciprocal Phase Element. I. Theory

R. V. Kiyan, A. A. Fotiadi, and O. V. Shakin*

Ioffe Physicotechnical Institute, Russian Academy of Sciences, St. Petersburg, 194021 Russia

** e-mail: oshakin@spbtlg.ru*

Received October 23, 2002

Abstract—The scheme of a bidirectional ring fiber laser with a 90° Faraday rotator in the cavity has been theoretically studied. The Faraday rotator is employed as a nonreciprocal phase element producing splitting of natural frequencies of the laser cavity modes propagating in opposite directions. The theory predicts two possible regimes of bidirectional operation. According to this, the laser generates a pair of modes propagating in opposite directions with either complex-conjugate or orthoconjugate polarization states. In the former case, the frequency shift between the modes propagating in opposite directions is independent of the reciprocal birefringence of the laser cavity and amounts to half of the free spectral band of this cavity. © *2003 MAIK "Nauka/Interperiodica".*

Introduction. Consider a ring laser gyroscope (RLG) representing a bidirectional ring laser. Rotation of the laser cavity in the plane of the natural mode propagation leads to the splitting of frequencies of the modes propagating in opposite directions, which is related to the Sagnak effect. The magnitude of this splitting is proportional to the angular rotation speed. Thus, the angular rotation speed can be measured and represented in the most convenient form: as a frequency difference of the natural modes propagating in opposite directions. This representation ensures ultimate sensitivity and maximum dynamic range of the angular rotation speed measurement [1].

At the same time, successful use of Er-doped optical waveguides in fiber amplifiers and lasers [2] makes the idea of creating an RLG based on the Er-doped fiber bidirectional ring laser (Er-FBRL) especially attractive. In order to attain this end, it is necessary to solve two problems: (i) to suppress the effect of frequency locking of the counterpropagating modes, which is related to parasitic backscattering in the cavity and is present in any FBRL, and (ii) provide for the stable generation of only one longitudinal mode propagating in each direction, with a stable frequency difference between the modes propagating in opposite directions. This difference must depend only on the cavity rotation speed, while the influence of all other nonreciprocal effects should be eliminated. Unfortunately, the opposite modes of an Er-FBRL are strongly coupled via the lasing medium because of the significant homogeneous broadening of the line of erbium ion lasing in a quartz glass matrix [3], which hinders stable bidirectional generation without frequency locking of the counterpropagating modes in such lasers.

The problem of ensuring stable bidirectional generation and suppressing undesired frequency locking was successfully solved in [4, 5]. The parasitic coupling was suppressed and the stable single-mode lasing in each direction was achieved by introducing a 45° Faraday rotator into the cavity of a fiber ring laser. The only disadvantage of this solution was that the presence of such an element in the cavity made the frequency shift between the opposite modes highly sensitive with respect to changes in the laser cavity birefringence. Below we will theoretically show that this disadvantage can be eliminated through optimization of the polarization rotation angle with the aid of a Faraday rotator.

Theory. A schematic diagram of the Er-FBRL with a 90° Faraday rotator in the laser cavity is depicted in the figure, with the optical elements forming the cavity being indicated in the legend. Let us consider the principle of this laser operation, assuming that both optical

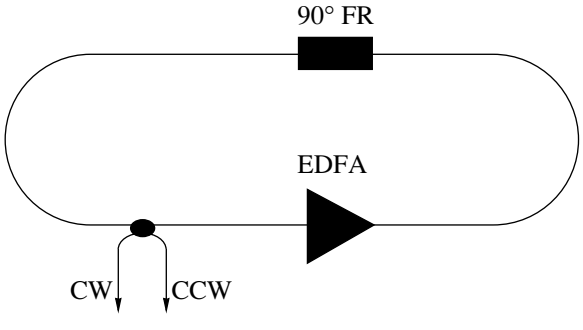

A schematic diagram of the Er-doped fiber bidirectional laser: (FR) 90° Faraday rotator; (EDFA) Er-doped fiber amplifier; (CW, CCW) outputs of laser radiation propagating clockwise and anticlockwise, respectively.

1063-7850/03/2905-0364$24.00 © 2003 MAIK "Nauka/Interperiodica"

losses and gain are polarization-independent. We will also assume that the laser cavity losses are compensated through the light amplification in the activated fiber. The polarization state of light propagating in the cavity clockwise and counterclockwise will be described in the common system of coordinates.

The birefringence of the reciprocal part of the cavity for a light wave propagating clockwise and counterclockwise is described by the unitary Jones matrices M and M^{T}, respectively (superscript T indicates the transposed matrix). In the general case, the Jones matrix M can be written as [6]

$$M = \begin{pmatrix} a & b \\ -b^* & a^* \end{pmatrix},$$

where the asterisk denotes complex conjugate; the matrix elements a and b depend on the birefringence characteristics of the reciprocal cavity part and satisfy the condition $|a|^2 + |b|^2 = 1$. The nonreciprocal part of the cavity consists only of the 90° Faraday rotator, the Jones matrix of which is independent of the light propagation direction and can be written as

$$F = \begin{pmatrix} 0 & 1 \\ -1 & 0 \end{pmatrix}.$$

The Jones matrices describing complete tracing of the cavity clockwise or counterclockwise appear as $F \cdot M$ and $M^{\mathrm{T}} \cdot F$, respectively. The natural modes of the cavity depicted in the figure can be determined from the following system of equations:

$$(F \cdot M) \cdot E_{\mathrm{CW}} = \lambda_{\mathrm{CW}} E_{\mathrm{CW}}, \quad (1)$$

$$(M^{\mathrm{T}} \cdot F) \cdot E_{\mathrm{CCW}} = \lambda_{\mathrm{CCW}} E_{\mathrm{CCW}}. \quad (2)$$

Here, E_{CW} and E_{CCW} denote the Jones vectors representing the natural modes of the cavity, which propagate clockwise or counterclockwise, respectively. Each of Eqs. (1) and (2) has two mutually orthogonal eigenvectors: E_{CW1}, E_{CW2} and E_{CCW1}, E_{CCW2}. The corresponding eigenvalues $\lambda_{\mathrm{CW1,2}}$ and $\lambda_{\mathrm{CCW1,2}}$ are related to the natural frequencies f_{CW} and f_{CCW} of the laser cavity by the equations

$$f_{\mathrm{CW,CCW}j} = (2\pi m + \delta_{\mathrm{CW,CCW}j})c/L,$$

$$\lambda_{\mathrm{CW,CCW}j} = \exp(i\delta_{\mathrm{CW,CCW}j}),$$

where L is the total optical pathlength of the laser cavity, c is the speed of light in vacuum, m is an integer, and $j = 1$ or 2.

Using the property of unitarity for matrix M and the explicit representation for matrix F, Eq. (2) can be transformed to

$$(F \cdot M) \cdot E^*_{\mathrm{CCW}} = -\lambda_{\mathrm{CCW}} E^*_{\mathrm{CCW}}. \quad (3)$$

A comparison of Eqs. (1) and (3) yields the following relation between the eigenvectors and eigenvalues of the opposite modes:

$$E_{\mathrm{CCW1,2}} = E^*_{\mathrm{CW1,2}}, \quad (4)$$

$$\lambda_{\mathrm{CCW1,2}} = -\lambda_{\mathrm{CW1,2}}. \quad (5)$$

Equations (4) and (5) describe the general properties of the Er-FBRL cavity with a 90° Faraday rotator as the nonreciprocal phase element. As can be seen from relation (4), each natural mode of this cavity is complex-conjugate with respect to one of the counterpropagating modes and is orthoconjugate with respect to the other. The phase difference between the orthoconjugate modes propagating in opposite directions accumulated upon complete tracing of the cavity depends on the total birefringence and falls within the interval $(-\pi, \pi)$. This implies that the difference between the natural frequencies corresponding to these opposite modes also depends on this birefringence and varies within the interval from $-\Delta\nu/2$ to $\Delta\nu/2$, where $\Delta\nu$ is the free spectral band of the laser cavity. On the other hand, relation (5) shows that the phase difference between the complex-conjugate modes propagating in opposite directions accumulated upon complete tracing of the cavity is independent of the total birefringence and always amounts to $\pm\pi$. Therefore, the difference between the natural frequencies corresponding to the opposite complex-conjugate modes is also independent of the birefringence and amounts to $\pm\Delta\nu/2$.

The above results show that it is possible to stabilize the difference between the natural frequencies of modes propagating in directions of an Er-FBRL and to eliminate the dependence of this difference on the birefringence of the fiber laser cavity. To this end, it is necessary to introduce a 90° Faraday rotator into the cavity and provide for the generation of complex-conjugate modes propagating in opposite directions.

Conclusion. We have performed a simple theoretical analysis of a bidirectional ring fiber laser with a 90° Faraday rotator in the cavity, playing the role of a nonreciprocal phase element. Two regimes of bidirectional operation have been predicted, according to which the laser generates a pair of modes propagating in opposite directions with either orthoconjugate or complex-conjugate polarization states. In the former case, the nonreciprocal frequency shift between the modes propagating in opposite directions significantly depends on the reciprocal birefringence of the laser cavity. Conversely, the nonreciprocal frequency shift between the opposite modes is independent of the reciprocal birefringence

and amounts to half of the free spectral band of this cavity. The latter regime is of considerable interest for applications such as fiber laser gyroscope.

Acknowledgments. This study was supported by the Russian Foundation for Basic Research, project no. 00-02-16903.

REFERENCES

1. W. W. Chow, J. Gea-Banacloche, L. M. Pedrotti, *et al.*, Rev. Mod. Phys. **57**, 61 (1985).
2. R. J. Mears and S. R. Baker, Opt. Quantum Electron. **24**, 517 (1992).
3. E. Desurvire, *Erbium-Doped Fiber Amplifiers* (Wiley-Interscience, New York, 1994), pp. 225–244.
4. R. Kiyan, S. K. Kim, and B. Y. Kim, in *Proceedings of the OFS-11, Sapporo, Japan, May 21–24, 1996*, Paper Th3-45, pp. 598–601.
5. R. Kiyan, S. K. Kim, and B. Y. Kim, IEEE Photonics Technol. Lett. **8**, 1624 (1996).
6. B. Lamouroux, B. Prade, and A. Orszag, Opt. Lett. **7**, 391 (1982).

Translated by P. Pozdeev

Technical Physics Letters, Vol. 29, No. 5, 2003, pp. 367–369. Translated from Pis'ma v Zhurnal Tekhnicheskoĭ Fiziki, Vol. 29, No. 9, 2003, pp. 29–34.

The Imaginary Components of Dispersion Parameters and the Stokes Mode Dynamics in Stimulated Raman Scattering

I. O. Zolotovskiĭ and D. I. Sementsov*

Ul'yanovsk State University, Ul'yanovsk, Russia

** e-mail: sementsovdi@ulsu.ru*

Received October 22, 2002

Abstract—The Stokes pulse dynamics during stimulated Raman scattering has been studied in the constant pumping approximation. The nonlinear problem of interaction between a pumping wave and the Stokes component is reduced to a linear equation describing propagation of an optical pulse in the amplifying medium with imaginary components of the first- and second-order dispersion parameters, the presence of which leads to the possibility of the pulse envelope propagation at a supraluminal velocity. *© 2003 MAIK "Nauka/Interperiodica".*

Stimulated Raman scattering (SRS) is a nonlinear process whereby a sufficiently intense pumping wave excites a wave of different frequency (the Stokes mode) in a given medium. When the pumping power exceeds a certain threshold level, the Stokes wave component exhibits a nearly exponential buildup [1, 2]. There are numerous SRS applications in which the important factors are the character (dynamics) of development of the Stokes mode and the possibility of its compression.

This paper demonstrates that, in the constant pump approximation [3], the essentially nonlinear problem of Stokes mode generation can be reduced to a quasilinear problem concerning optical pulse propagation in an amplifying medium with imaginary components of the dispersion parameters. These parameters, together with the intermode interaction parameter, determine the radiation dynamics and the conditions of compression of a pulse propagating in an optical waveguide [4–7]. This approach to description of the SRS process significantly simplifies the analysis and reveals some new features of this phenomenon.

Consider the interaction between a quasimonochromatic pumping wave and the Stokes wave in the course of the SRS process. This process can be described using the following system of equations:

$$\begin{aligned}
&\frac{\partial A_n}{\partial z} + \frac{1}{u_n}\frac{\partial A_n}{\partial t} - i\frac{d_n}{2}\frac{\partial^2 A_n}{\partial t^2} + iR(|A_n|^2 + 2|A_s|^2)A_n \\
&\qquad = -\frac{g_n}{2}|A_s|^2 A_n, \\
&\frac{\partial A_s}{\partial z} + \frac{1}{u_s}\frac{\partial A_s}{\partial t} - i\frac{d_s}{2}\frac{\partial^2 A_s}{\partial t^2} + iR(|A_s|^2 + 2|A_n|^2)A_s \\
&\qquad = \frac{g_s}{2}|A_n|^2 A_s,
\end{aligned} \tag{1}$$

where $A_{n,s}$ are the amplitudes of the pumping and Stokes waves, respectively; $u_{n,s} = (\partial\beta_{n,s}/\partial\omega)_0^{-1}$ and $d_{n,s} = (\partial^2\beta_{n,s}/\partial\omega^2)_0$ are the corresponding group velocities and second-order dispersion parameters; $\beta_{n,s}$ are the propagation constants; $g_{n,s}$ are the Raman coefficients; and R is a parameter characterizing the nonlinearity of the optical waveguide.

Let us solve system (1) in the constant pump approximation, assuming that the pumping wave intensity can be considered constant over the propagation length ($|A_n|^2 \cong \text{const}$) and that the Stokes component intensity is relatively small ($|A_s|^2 \ll |A_n|^2$). Under these conditions, the equation describing the amplitude of the Stokes component takes the following form:

$$\frac{\partial A_s}{\partial z} + \frac{1}{u_s}\frac{\partial A_s}{\partial t} - i\frac{d_s}{2}\frac{\partial^2 A_s}{\partial t^2} + 2iR|A_n|^2 A_s = \frac{g_s}{2}|A_n|^2 A_s. \tag{2}$$

Substituting $A_s = C_s\exp[(2iR - g_s/2)I_n z]$, where $I_n = |A_n|^2$, we arrive at a linear equation for the amplitude C_s:

$$\frac{\partial C_s}{\partial z} + \frac{1}{\tilde{u}_s}\frac{\partial C_s}{\partial t} - i\frac{\tilde{d}_s}{2}\frac{\partial^2 C_s}{\partial t^2} = 0, \tag{3}$$

where $\tilde{u}_s = (\partial\tilde{\beta}_s/\partial\omega)_0^{-1}$, $\tilde{d}_s = (\partial^2\tilde{\beta}_s/\partial\omega^2)_0$, and $\tilde{\beta}_s$ is the complex propagation constant of the Stokes wave, defined as $\tilde{\beta}_s = \beta_s' - i\beta_s''$, with $\beta' = \beta_s - 2RI_n$ and $\beta_s'' = -g_s(\omega)I_n/2$. Thus, the initial problem is reduced to the description of a quasilinear wave propagating in an amplifying medium ($g_s > 0$) with an effective gain increment $\gamma_s = -2\beta_s''$ and the imaginary components of dispersion parameters $(\tilde{u}_s'')^{-1} = (\partial\beta_s''/\partial\omega)_0$ and $\tilde{d}_s'' = (\partial^2\beta_s''/\partial\omega^2)_0$. Analogous problems have been considered in sufficient detail in our recent papers [4–6],

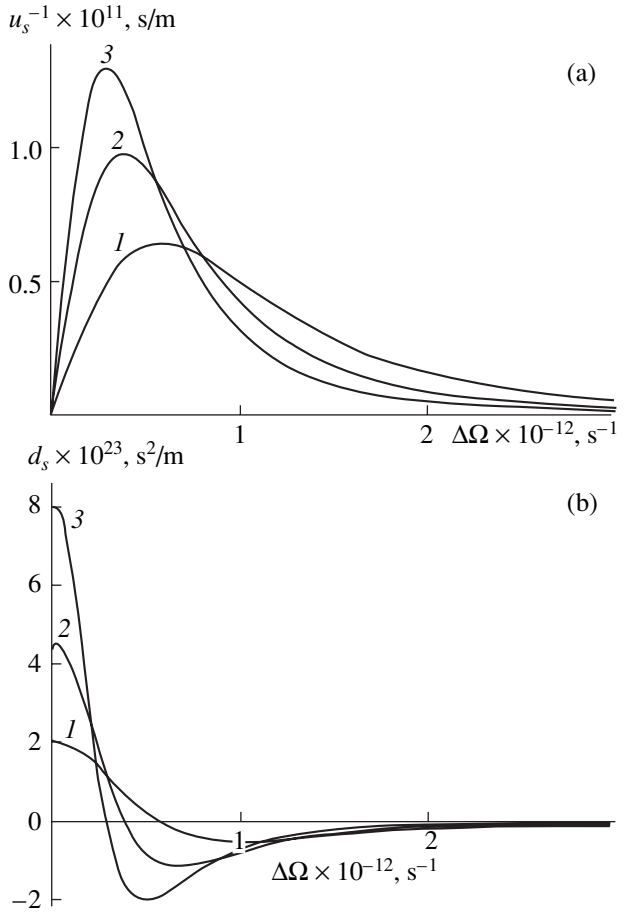

Frequency dependence of the (a) first-order and (b) second-order dispersion parameters calculated for $T_2 = 10^{-12}$ (*1*), 1.5×10^{-12} (*2*), and 2×10^{-12} s (*3*).

where it was demonstrated that an optical waveguide with complex second-order dispersion parameters can feature the compression of light pulses without initial frequency modulation and phase self-modulation (i.e., the self-compression of pulses is possible at an arbitrarily small power level). The general analysis of Eq. (3) shows that compression of the Stokes pulse is possible for $(\partial^2\beta_s''/\partial\omega^2)_0 < 0$, that is, for $(\partial^2 g_s/\partial\omega^2)_0 > 0$. In the case of a Gaussian pulse, the degree of compression is defined as

$$\tau_0/\tau_{\min} = \frac{|\eta|}{\sqrt{2}}\left(\sqrt{\eta^2 + 1} - 1\right)^{-1/2}, \qquad (4)$$

where $\eta = d_s''/\tilde{d}_s'$ and $\tilde{d}_s' = \partial^2\beta'/\partial\omega^2$. For $|\eta| \gg 1$, the degree of compression is also large ($\tau_0/\tau_{\min} = \sqrt{|\eta|/2}$), and a minimum pulse duration is attained over a compression length of $z_{\text{com}} \cong \tau_0^2/|\tilde{d}_s''|$.

Let us estimate the dispersion parameters in the case under consideration. In the approximation of a Lorentzian shape of the Stokes wave amplification band, the frequency dependence of the gain increment is described by the formula

$$\gamma_s(\omega) = g_s(0)I_n/(1 + T_2^2\Delta\Omega^2), \qquad (5)$$

where T_2 is the relaxation time determining the width of the spontaneous Raman scattering line, $\Delta\Omega = \omega_s - \omega_n + \Omega_m$, Ω_m is the natural frequency of molecular vibrations, and $g_s(0)$ is the nonlinear coupling coefficient. Taking into account formula (5) and the relation $\gamma_s = -2\beta_s''$, we obtain the following expression for the imaginary components of the first- and second-order dispersion parameters:

$$\tilde{u}_s''^{-1} = (\partial\beta_s''/\partial\omega)_0 = \frac{g(0)T_2^2\Delta\Omega I_n}{(1 + T_2^2\Delta\Omega^2)^2}, \qquad (6a)$$

$$\tilde{d}_s'' = (\partial^2\beta_s''/\partial\omega^2)_0 = \frac{g(0)T_2^2 I_n(1 - 3T_2^2\Delta\Omega^2)}{(1 + T_2^2\Delta\Omega^2)^3}. \qquad (6b)$$

Since these parameters determine the dynamics of a wave packet formed by the Stokes component, let us obtain some characteristic estimates. For $\Delta\Omega = \pm 1/\sqrt{3}T_2$, the value of $|\tilde{u}_s''|^{-1}$ reaches a maximum of $9g(0)I_nT_2/16\sqrt{3}$, while $\tilde{d}_s''$ passes through zero and changes sign. In contrast, for $\Delta\Omega = 0$, the parameter $(\tilde{u}_s'')^{-1}$ passes through zero and changes sign, while $\tilde{d}_s''$ reaches a maximum positive value of $g(0)I_nT_2^2$. At $\Delta\Omega = \pm T_2^{-1}$, the latter parameter reaches a maximum negative value of $\tilde{d}_s'' = -g(0)I_nT_2^2/4$. The frequency dependences of these quantities are depicted in the figure. Taking into account that $(\tilde{u}_s'')^{-1}$ is odd with respect to $\Delta\Omega$, whereas $\tilde{d}_s''$ is even, these quantities are presented only for $\Delta\Omega > 0$. The plots were calculated for the following parameters: $g(0) = 2 \times 10^{-13}$ m/W, $I_n = 10^{14}$ W/m^2, and $T_2 = (1; 1.5; 2) \times 10^{-12}$ (for curves *1–3*, respectively). Let us evaluate the degree of compression of the Stokes component. Selecting $T_2 \cong 10^{-12}$ s, $\Delta\Omega \cong \sqrt{2/3} \times 10^{12}$ s^{-1}, and $\tilde{d}_s' \cong 10^{-28}$–$10^{-27}$ s^2/m (typically, $\partial^2 R/\partial\omega^2 \cong 0$ and $\tilde{d}_s' \cong d_s$), we obtain $\eta \cong 10^3$–10^4 and $\tau_0/\tau_{\min} \cong 25$–$70$. Still greater degrees of compression can be obtained through phase modulation of the Stokes wave [5, 6].

In addition to determining the degree of compression, the above imaginary components of the dispersion parameters significantly influence the shape of the wave packet envelope. In particular, the wave packet envelope of a Stokes pulse can travel at a supraluminal velocity in a medium with induced amplification. In

this case, the envelope maximum velocity is given by the expression [7]

$$u_s = \tilde{u}_s'(1 + b\tilde{u}_s'/\tilde{u}_s'')^{-1}, \quad (7)$$

where $b = \tilde{d}_s' z(\tau_0^2 + \tilde{d}_s'' z)^{-1}$, while $\tilde{u}_s'$ essentially represents the group velocity. An analysis of expression (7) shows that, for $b/\tilde{u}_s'' < 0$, the envelope maximum velocity of a Stokes pulse propagating in a waveguide can even exceed the speed of light in vacuum.

It should be noted that the imaginary components of dispersion parameters most strongly influence the Stokes pulse dynamics at a certain detuning from resonance, where $\tilde{d}_s'' < 0$, rather than exactly at resonance (where $\Delta\Omega \cong 0$). It is such a detuning that provides for the possibility of compression of the Stokes component. In the contrast, for $\tilde{d}_s'' > 0$, the imaginary components of dispersion parameters favor an additional broadening of the Stokes pulse. This result shows the importance of correctly selecting the working frequency (which does not necessarily correspond to a maximum of the SRS amplification band).

The SRS interaction is not the only nonlinear problem that can be correctly reduced to a quasilinear case. Linear equations of type (3), describing pulse propagation in a medium with induced amplification and complex dispersion parameters, can be obtained in many problems involving energy pumping from a powerful base wave to small perturbation wave via parametric interactions. In particular, an example of this type is offered by the motion of a sequence of breathers—perturbations arising in a medium with induced amplification as a result of the development of a strong modulation instability during the interaction of a high-power quasimonochromatic pumping wave with gain-inducing perturbations.

REFERENCES

1. Y. R. Shen, *The Principles of Nonlinear Optics* (Wiley, New York, 1984; Nauka, Moscow, 1989).
2. S. A. Akhmanov, V. A. Vysloukh, and A. S. Chirkin, *The Optics of Femtosecond Laser Pulses* (Nauka, Moscow, 1988).
3. G. Agrawal, *Nonlinear Fiber Optics* (Academic, San Diego, 1995; Mir, Moscow, 1996).
4. I. O. Zolotovskiĭ and D. I. Sementsov, Zh. Tekh. Fiz. **70** (10), 57 (2000) [Tech. Phys. **45**, 1288 (2000)].
5. I. O. Zolotovskiĭ and D. I. Sementsov, Kvantovaya Élektron. (Moscow) **30** (9), 794 (2000).
6. I. O. Zolotovskiĭ and D. I. Sementsov, Opt. Spektrosk. **91**, 138 (2001) [Opt. Spectrosc. **91**, 127 (2001)].
7. A. V. Zolotov, I. O. Zolotovskiĭ, and D. I. Sementsov, Pis'ma Zh. Tekh. Fiz. **27** (17), 22 (2001) [Tech. Phys. Lett. **27**, 719 (2001)].

Translated by P. Pozdeev

Technical Physics Letters, Vol. 29, No. 5, 2003, pp. 370–372. Translated from Pis'ma v Zhurnal Tekhnicheskoĭ Fiziki, Vol. 29, No. 9, 2003, pp. 35–41.

High-Field Domain Formation in Thyristor Structures at Ultrahigh Current Densities

A. V. Gorbatyuk* and I. E. Panaĭotti

Ioffe Physicotechnical Institute, Russian Academy of Sciences, St. Petersburg, 194021 Russia

** e-mail: agor.pulse@mail.ioffe.ru*

Received November 25, 2002

Abstract—We have studied the mechanism of high-field domain formation in thyristor structures at ultrahigh current densities ($J \gg 100$ A/cm^2) and the related effect of anomalous buildup of the direct residual voltage. The analysis is based on the results of numerical simulation of the process of double injection with allowance for accompanying nonlinear effects. © *2003 MAIK "Nauka/Interperiodica".*

The new field of gigawatt semiconductor electronics arose quite recently for solving the problems of modern pulsed power engineering [1]. The key element in this field is the reverse switched dinistor (RSD), a diode thyristor type device capable of switching current pulses with an amplitude of several hundred of kiloamperes at a pulse duration of tens and hundreds of microseconds—far beyond the limits tolerated by usual pulse thyristors [2–4]. The principles of RSD operation are considered in detail elsewhere [5–7]. Provided a sufficiently powerful control, an RSD structure switches from blocking to conducting state, bypassing the stage of regenerative current buildup. During this, the working space of the RSD structure, initially occupied by a high-field domain, is rapidly and simultaneously filled by an electron–hole plasma. It is believed that the high-conductivity state of this device is retained at a current density amplitude of up to 10 kA/cm^2 (typical of RSDs).

This short communication addresses certain features of the injection processes in structures of the thyristor type operating in microsecond pulse regimes (that is, upon going from a usual level of $J \sim 100$ A/cm^2 to ultrahigh current densities), related to the possibility of repeated high-field domain formation.

The process of double injection observed in thyristor structures under conditions of high currents and voltages exceeding several volts are always associated with separation of the modulated conductivity gap into the anode plasma region and the collector field domain (see [8] and references therein). In a stationary state, such systems obey the relation

$$\alpha_K(J, U) + \alpha_A(J, U) = 1, \quad (1)$$

where $\alpha_K(J, U)$ and $\alpha_A(J, U)$ are the cathode and anode compound transistor current gain, respectively, determined to a considerable extent by the carrier diffusion via quasineutral base layers. The dependences of $\alpha_{K, A}$ on the applied voltage are determined by the effective base thickness, which decreases with increasing collector field domain thickness and the corresponding voltage drop.

Near the switching threshold, where the emitter shunting effect is reduced, the $\alpha_{K, A}$ values increase with the current. This provides for the very existence of states with negative differential resistance (NDR) and ensures bistability of the whole system. However, large currents may also initiate additional mechanisms of the excess charge loss, such as Auger recombination and quadratic carrier leak from the bases (at a high level of injection) into the emitter layers. The tendency of the $\alpha_{K, A}$ growth with the current may change to a decrease, which, by virtue of relation (1), must be compensated by a growth in the sum $\alpha_K(J, U) + \alpha_A(J, U)$ due to an increase in the voltage drop. This, in turn, is possible only at the expense of a partial demodulation of the conductivity, the field domain formation, and a decrease of the diffusion transport regions.

The corresponding effects can be analyzed within the framework of a self-consistent system of the continuity equations for electrons and holes and the Poisson equation, with allowance for factors such as the drift velocity saturation with increasing field strength, the dependence of the carrier recombination rate on the level of injection, and the effect of strong doping of the lifetimes and mobilities of electrons and holes. In order to provide for such a description, we used the special program package ISSLEDOVANIE [9, 10], the physical basis and numerical algorithm of which fully meet the above requirements.

We have modeled a real $n^{++}p^+pn^-p^+$ RSD structure as fabricated using a diffusion technology involving sequential doping with boron, phosphorus, and aluminum (or gallium). The structure has a thickness of 400 μm and is operated by a switching voltage of ~2 kV. The dopant concentration–depth profiles in the

1063-7850/03/2905-0370$24.00

near-cathode region of the structure are presented in Fig. 1 (thick solid curves). The cathode transistor base comprises a narrow p^+ layer with a high surface dopant density $(N_A^+)_S$ and a broader p layer with decreased dopant density. The cathode emitter is shunted with a reduced surface-distributed leak resistance $R_K = 5\ \Omega\ \text{cm}^2$, which must provide for a stable blocking state in case of an occasional voltage jump from zero to 2 kV within a rise time of 1 μs. The presence of distributed (with a period of 30–100 μm) channels of reverse pumping from the side of the anode is modeled by a continuous n' layer, which is somewhat thicker than the p^+ emitter layer. The effective reduced resistance $R_A = 100\ \Omega\ \text{cm}^2$ is significantly greater than R_K. The decrease in the minority carrier lifetime ($\tau_{p,n}$) in strongly doped layers with the corresponding impurity concentrations $N_{A,D}$ is described by the well-known Scharfetter formula

$$\tau_{n,p} = \frac{\tau_{n,p_{\max}}}{1 + N_{A,D}/N^*_{A,D}}.$$

In the case under consideration, $N_A^* = N_D^* = 5 \times 10^{16}\ \text{cm}^{-3}$, $\tau_{n_{\max}} = 11$ μs, and $\tau_{p_{\max}} = 4$ μs.

Since the RSD switching time amounts to a few microseconds, while pulsed heating is manifested upon elapse of a few tens of microseconds [7], we can restrict the consideration to stationary isothermal states. Figure 2 shows the current–voltage characteristics calculated for positive bias (with plus on the right-hand anode contact) in a broad range of current densities J (curves *1–5*). The parameter $(N_A^+)_S$ decreases from $1.2 \times 10^{18}\ \text{cm}^{-3}$ (curve *1*) to $0.6 \times 10^{18}\ \text{cm}^{-3}$ (curve *4*) at a step of $2 \times 10^{17}\ \text{cm}^{-3}$; curve *5* corresponds to $(N_A^+)_S = 0$. All curves display a region corresponding to the collector avalanche breakdown and the branches of negative (NDR) and positive differential resistance (PDR). In the general case, the PDR branch contains intervals with low (normal) and overstated (anomalous) differential resistance $r_d = dU/dJ$ (or the normal and anomalously high residual voltage). A threshold corresponding to the passage from small to large r_d values decreases with increasing $(N_A^+)_S$. For $(N_A^+)_S > 1.2 \times 10^{18}\ \text{cm}^{-3}$, the NDR region is immediately adjacent to the PDR region (featuring increased r_d), while, for $(N_A^+)_S < 0.6 \times 10^{18}\ \text{cm}^{-3}$, no region with large r_d is observed until the current density reaches $10^4\ \text{A/cm}^2$.

Let us consider the peculiarities in the mechanism of formation of a region with anomalously high U values in a typical high-power thyristor structure with a relatively high dopant level in the p base region, $(N_A^+)_S = 10^{18}\ \text{cm}^{-3}$ (Fig. 2, curve *2*). The corresponding injected carrier density profiles for four values of J are presented

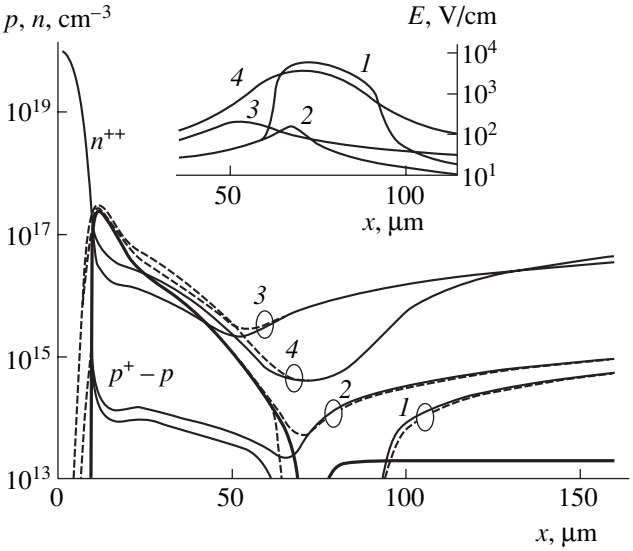

Fig. 1. Depth profiles of dopant concentration (thick solid curves), electron density (solid curves), and hole density (dashed curves) in a model RSD structure at various current densities. The inset shows the field strength profiles near the collector, curves *1–4* corresponding to points J_1–J_4 in the current–voltage characteristics of Fig. 2.

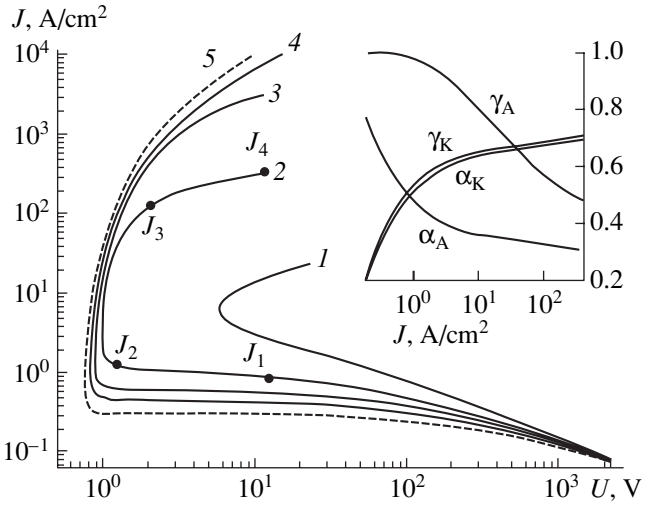

Fig. 2. Forward current–voltage characteristics of model RSD structures with different levels of p base doping. The inset shows the plots of injection coefficients $\gamma_{A,K}$ and current gain $\alpha_{A,K}$ versus current density for the anode and cathode compound transistors.

in Fig. 1. The inset in Fig. 1 shows the corresponding field strength distributions along the current channel. A change in the collector bias voltage sign from minus to plus, conditionally indicating the transition to a branch of conducting states, is observed at $J = J_2 = 1.2\ \text{A/cm}^2$ and $U = 1.2$ V (Fig. 2). As a result, the depleted collector layer vanishes and the internal field of the collector decreases to ~150 V/cm (inset in Fig. 1). As the J value increases from J_2 to $J_3 \sim 100\ \text{A/cm}^2$, the plane of mini-

mum hole density p and the weakly pronounced field maximum E shift leftward to $x = 70$ μm, which corresponds to the region of pronounced doping of the p base. A high injection level is retained almost everywhere to the right from this plane, while the voltage drop across the structure in this interval does not exceed 2 V. However, as the current grows further, the plasma density at the collector begins to decrease (despite an increase in the plasma density on the anode side) and, simultaneously, a high-field domain begins to grow. The voltage drop across this domain increases from a few volts to several tens of volts even for current 2–3 times above the threshold J_3.

The inset in Fig. 2 shows the plots of the injection coefficients $\gamma_{A,K}$ and the current gain $\alpha_{A,K}$ versus current density numerically calculated for the anode and cathode compound transistors. The boundary between transistors is selected at the plane of maximum field strength. The cathode transistor, in which a low injection level is retained in the interval $J_3 < J < J_4$ and the emitter shunting is weak, is characterized by a virtually constant gain of $\alpha_K \approx \gamma_K$. Here, the gain is significantly lower than unity and even smaller than $b/(b + 1) \approx 0.73$ (Si), which is indicative of a considerable decrease in the hole lifetime in the n^+ layer and a significant thermal leak of holes to this layer. The anode transistor gain $\alpha_A = \gamma_A\beta_A = 1 - \alpha_K$ is also almost constant. At the same time, the injection coefficient γ_A of the anode emitter significantly drops with increasing current. This is evidence of a strong increase in the electron loss from the n base plasma and is indicative of the Auger recombination processes initiated when the plasma density in the region of the anode emitter increases above $\sim 10^{18}$ cm^{-3}. A compensating increase in the parameter β_A is related to a decrease of the diffusion transport region with decreasing plasma density in the vicinity of the collector and with repeated high-field domain formation in the near-collector base region.

Apparently, the above phenomenon of repeated high-field domain formation in thyristor structures at high current densities, accompanied by the anomalous growth of energy losses, can be a factor significantly limiting the ultimate characteristics of pulsed semiconductor switches. Elimination of such effects requires a thorough revision of the principles of designing devices operating with ultrahigh current densities (10^3–10^4 A/cm^2 and above).

Acknowledgments. The authors are grateful to I.V. Grekhov for his interest in this study and fruitful discussions and to T.T. Mnatsakanov and A.S. Kyuregyan for kindly providing the possibility of using the ISSLEDOVANIE program package.

REFERENCES

1. I. V. Grekhov, *The 11th IEEE International Pulsed Power Conference, June 29–July 2, 1997, Baltimore, Maryland*, Ed. by G. Cooperstein and I. Vitkovsky (1997), Vol. 1, pp. 425–429.
2. M. E. Savage, IEEE Trans. Plasma Sci. **28**, 1451 (2000).
3. S. Schneider and T. F. Podlesak, IEEE Trans. Plasma Sci. **28**, 1520 (2000).
4. E. R. Brown, Solid-State Electron. **42**, 2119 (1998).
5. A. V. Gorbatyuk, I. V. Grekhov, S. V. Korotkov, *et al.*, Pis'ma Zh. Tekh. Fiz. **8**, 685 (1982) [Sov. Tech. Phys. Lett. **8**, 298 (1982)]; Zh. Tekh. Fiz. **52**, 1369 (1982) [Sov. Phys. Tech. Phys. **27**, 832 (1982)].
6. A. V. Gorbatyuk, I. V. Grekhov, and A. V. Nalivkin, Solid-State Electron. **31**, 1483 (1996).
7. A. V. Gorbatyuk and I. E. Panaĭotti, Zh. Tekh. Fiz. **60** (5), 129 (1990) [Sov. Phys. Tech. Phys. **35**, 612 (1990)]; Zh. Tekh. Fiz. **61** (6), 83 (1991) [Sov. Phys. Tech. Phys. **36**, 635 (1991)].
8. A. V. Gorbatyuk and P. B. Rodin, Radiotekh. Élektron. **35**, 1336 (1990).
9. T. T. Mnatsakanov, I. L. Rostovtsev, and N. I. Filatov, Élektron. Model. **8** (1), 40 (1986).
10. T. T. Mnatsakanov, I. L. Rostovtsev, and N. I. Filatov, Solid-State Electron. **30**, 579 (1987).

Translated by P. Pozdeev

Technical Physics Letters, Vol. 29, No. 5, 2003, pp. 373–376. Translated from Pis'ma v Zhurnal Tekhnicheskoĭ Fiziki, Vol. 29, No. 9, 2003, pp. 42–50.

Barrier Open Discharge at Atmospheric Pressure

A. R. Sorokin

Institute of Semiconductor Physics, Siberian Division, Russian Academy of Sciences, Novosibirsk, 630090 Russia

Received November 13, 2002

Abstract—A barrier open discharge operating under extremely hindered conditions is proposed, in which the working gas (helium) pressure admitting the electron beam formation can be increased up to 0.8 atm (more than ten times as compared to the usual open discharge) without any loss in stability. The anode grid (with 0.17 mm holes) was made separately and then placed on a dielectric substrate ($\varepsilon \approx 1000$), but it can also be formed using vacuum deposition or photolithographic techniques. It is suggested that, by decreasing the diameter of holes in the anode grid, it is possible to provide for a stable discharge operation under still higher gas pressures. *© 2003 MAIK "Nauka/Interperiodica".*

Introduction. In a usual open discharge, the field (either in a cathode region or in the whole interelectrode gap) is sufficiently strong to provide for the "runaway" of electrons, which form electron beams penetrating through a grid anode into a drift region [1].

In a typical discharge gap of d = 0.5–1 mm, the working gas pressure does not exceed several tens of Torr. The main problem is to maintain a sufficiently high potential drop across the cathode layer during the pulse and to provide for a stable discharge. At a helium pressure of p_{He} = 100 Torr, the length of the cathode fall region is as small as l_{cf} = 0.05 mm and the field strength at the cathode (for an applied voltage of U = 5 kV) is $E_c \approx 2U/l_{cf} = 2 \times 10^6$ V/cm; this is about ten times greater than the value necessary for initiating the explosion emission processes on a metal cathode [2]. The equivalent anomalous discharge current density under these conditions would reach about 600 A/cm^2. In a pulsed regime, stable discharge under these conditions can be maintained for several nanoseconds [3].

An additional problem is related to the formation of voltage pulses exciting discharge with a sufficiently steep leading front. Indeed, the leading front duration for $d \gg l_{cf}$ must also be as short as a few nanoseconds, otherwise a breakdown will take place on the leading front at a relatively small voltage. Increasing the possible time of discharge formation under hindered conditions by making the gap width comparable with l_{cf} (i.e., on the order of 50 μm) can hardly be realized in practice.

Electron beams generated under open discharge conditions offer an effective means of pumping gas lasers [4]. It would therefore be very interesting to expand the interval of working pressures toward higher values, in particular, for increasing the output laser power; other applications are possible as well [5].

In order to solve this task, the author suggests using a barrier open discharge between a cathode, representing a metal electrode coated with a dielectric layer, and a grid anode placed immediately on the dielectric surface. Under these conditions, the discharge must be highly stable because of (i) reduced electron emission from the dielectric material providing for a greater cathode fall region and (ii) hindered development of inhomogeneities. The initial current of inhomogeneity rapidly decreases the local field strength and charges a dielectric surface area restricted to a single grid hole (in a usual barrier discharge, the whole surface can be charged). This prevents from the development of a spark gap discharge. In the proposed system, the discharge hindrances (and, hence, the limiting working pressure) must be primarily determined by the size of grid holes, which can be made arbitrarily small.

Recently [6], barrier open discharge was studied between a grid anode (with a hole size of A = 2 mm) 1.5 mm from a ceramic cathode (with a permittivity of ε = 4). This system differs from that proposed above in that the discharge is not extremely hindered. The discharge in [6] was stable up to an atmospheric pressure level, which is quite natural, since the anode holes do not influence the discharge (a stable barrier discharge with laser radiation emission up to a pressure of 17 atm was reported in [7]), but effective electron beam generation with a current density of ~1 A/cm^2 was possible only at a small pressure of 5–20 Torr. Below we will consider the features of operation of the proposed discharge system and discuss the possibility of further increasing the working gas pressure.

Experimental results. The experiments were performed with a ceramic insulator of the KVI-2 type capacitor (68 pF, 16 kV, $\varepsilon \sim 1000$, 10 mm in diameter). The capacitor was ground on one side to leave an area of diameter δ = 2 mm at the center, and the contact on the other side was connected to the minus output of the voltage source. The anode grid had a hole size of 0.17 mm and a geometric transparency of 0.72. The

1063-7850/03/2905-0373$24.00

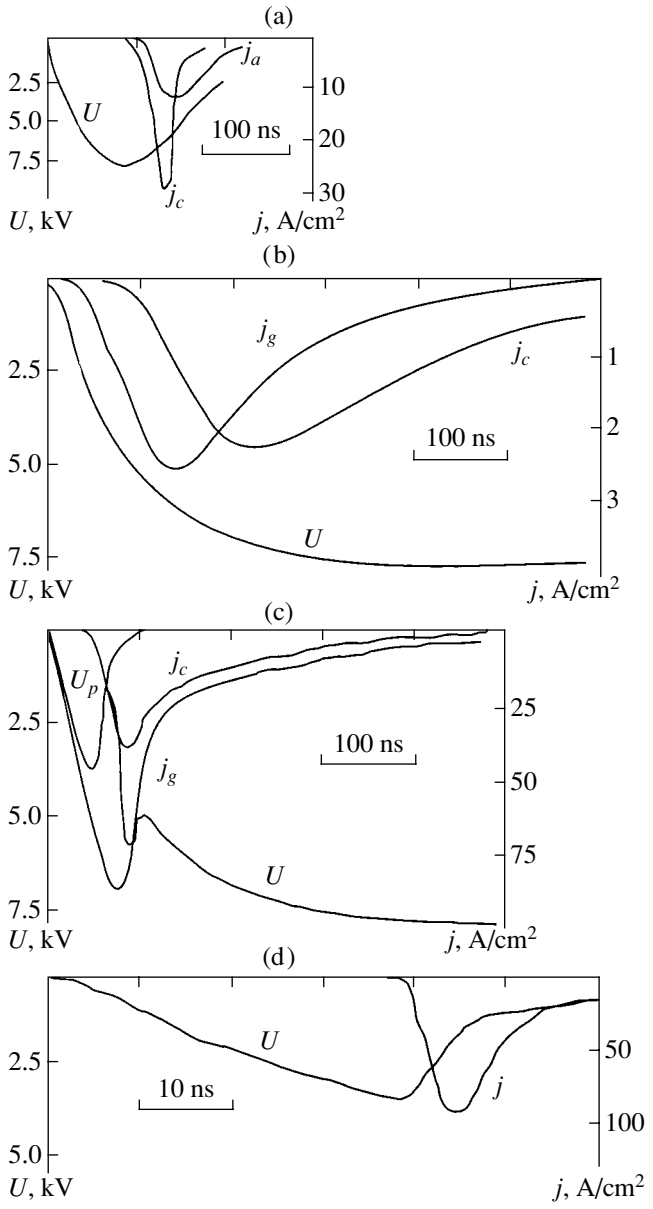

Fig. 1. Voltage and current oscillograms illustrating the kinetics of (a) open discharge, (b, c) hindered barrier discharge, and (d) usual anomalous discharge at a helium pressure of 30 Torr. See the text for explanations.

current density was determined as the ratio of the current to the active cathode surface area, that is, to the total area of holes in the grid ($S = 0.45$ cm^2).

Now let us consider the behavior of a discharge in various gaps, first at a helium pressure of 30 Torr. Figure 1 shows the voltage and current oscillograms measured in a usual open discharge [8] and in the proposed barrier discharge. The beam current was monitored using a collector grid (0.5 mm period; $\mu = 0.65$) and a collector 5 and 10 mm from the cathode, respectively. These elements could influence the discharge. Indeed, although the anode grid with 0.17 mm holes screens the field "sagging" into the drift space and concentrates the field at the insulator, the field strength in the cathode–collector grid gap (5 mm) can be sufficient for the discharge initiation. At pressures not exceeding 30 Torr, this discharge is not hindered, because the parameter $pd_{ag} = 15 > (pd)_{\min} = 4$ Torr cm corresponds to the right-hand branch of the Paschen curve. The discharge starts developing via short field lines to charge the part of the dielectric surface opposite to the collector grid wires (see the curve for j_g in Fig. 1b).

As the cathode fall region is formed, the field concentrates at the cathode to provide for better "runaway" conditions for the electrons forming the electron beam. The discharge current charges the remaining dielectric surface (eventually, the part facing the collector grid holes). Therefore, the discharge current in the final discharge stage is predominantly carried by an electron beam to the collector (j_c), while the current to the collector grid (j_g) rapidly tends to zero (Fig. 1b).

If the collector grid and collector are left at a free potential (disconnected), the discharge becomes more hindered (not being influenced by the cathode–collector grid gap) and the discharge current significantly decreases, as evidenced by a drop in the intensity of emission from the gas. The breakdown delay must also increase, but this is difficult to judge by a change in the oscillogram of the anode current (j_a), because the discharge current is small compared to the current charging the capacitor formed by the metal cathode and the anode grid wires (j_a is the sum of these currents).

A different behavior is observed for the open discharge (Fig. 1a). Under more hindered conditions, $pd = 1.5 < (pd)_{\min}$ (left-hand branch of the Paschen curve), the discharge starts developing via the longest field line (as in the case of a hollow anode [5]). In this initial stage, the discharge current is predominantly carried by an electron beam to the collector; only during the cathode fall formation does the discharge spread (with delay) to the grid wires and the anode current appears. In a typical open discharge, the traces of cathode sputtering are always centered at the grid hole axes.

Another significant difference is that the barrier discharge, despite favorable onset conditions (whereby the discharge is first developed in the long gap between cathode and collector grid and is initiated earlier than the open discharge, cf. Figs. 1a and 1b), is characterized by discharge currents about ten times lower. A question arises as to whether this is explained only by the lower electron emission from the dielectric surface.

Figure 1c shows the oscillograms observed when the anode grid is disconnected and left under a free potential U_p (measured in a high-resistance circuit). This potential first increases (simultaneously with U) until breakdown in the cathode–collector grid gap, after which U_p drops to zero. It is important to note that all the applied voltage even in this case is rapidly concentrated at the cathode.

The growth in the collector grid current is by no means surprising, since this signal includes the current charging the capacitor formed by the metal cathode and the anode grid wires. Under the conditions of Fig. 1b, this current contributes to the anode current j_a (not shown in the figure). An important fact is a tenfold growth in the collector current j_c. Apparently, the electron emission from the dielectric surface is not as small, but the lower current is explained by extremely hindered barrier discharge conditions in the high-current stage (Fig. 1b).

For the sake of completeness, Fig. 1d shows the oscillograms of a direct discharge (i.e., usual anomalous discharge) between the collector (with minus sign) and the collector grid spaced by 5 mm.

High-pressure discharge. Figure 2a shows the voltage oscillograms for the open discharge (d = 0.6 mm) and a barrier discharge in helium at 400 Torr. Under these conditions, the barrier discharge is more hindered than the open discharge. As a result, both the delay ($\tau_{BD} \approx 2\tau_{OD}$) and the breakdown voltage increase in the initial stage despite the connected collected grid. It should also be noted that the open discharge (but not the barrier discharge) loses stability. It should be emphasized that the two factors—extremely hindered conditions and stability of the barrier discharge—are the essence of the proposed method of electron beam generation at high pressures.

Figure 2b presents the voltage oscillograms for barrier discharge without a collector grid, measured at a collector–cathode distance of 10 mm and a pressure of 200 Torr. For the anode current j_a, the dashed curve shows the anode grid charging in vacuum, while the solid branch shows the anode current contribution due to the discharge. As can be seen, the collector current appears before the high-current stage of the latter contribution arising on the background of decaying voltage. It should be noted that, except for the initial portion, the U profile (here and in the other diagrams) does not directly characterize the voltage drop across the discharge gap, since charging of the dielectric surface leads to leveling of the potentials of this surface and the anode grid. Thus, a question arises as to what part of the collector current corresponds to the electron beam current.

It was established that the discharge parameters at high pressures (p > 100 Torr) cease to depend on whether the anode grid and collector are at a free potential or not (i.e., all discharge processes take place near the cathode, where all the applied voltage drops). Therefore, the collector (once it is connected) detects the electron beam current. This is confirmed by observation of the direct (i.e., anomalous) discharge between the collector and collector grid (spaced by 5 mm). At a pressure of 400 Torr and the same applied voltage pulse as in Fig. 2a, this discharge proceeds at a greater delay of 150 ns (cf. Fig. 1d) because the parameter pd_{gs} = 200 Torr cm is greater by two orders of magnitude

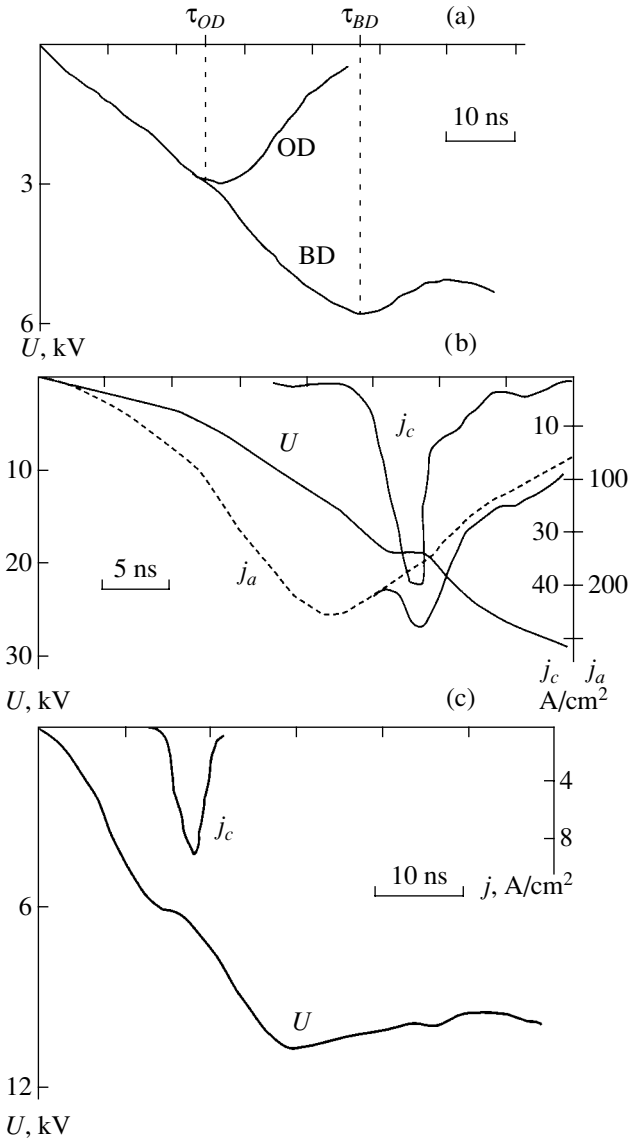

Fig. 2. Voltage and current oscillograms illustrating the kinetics of (a) open discharge (OD) and (a, b, c) hindered barrier discharge (BD) at a helium pressure of p = 400 Torr (a), 200 Torr (b), and 0.8 atm (c). See the text for explanations.

than $(pd)_{\min}$. Here, the breakdown voltage and/or delay increase because of excess pressure.

Thus, for a barrier discharge with connected collector grid under conditions of high pressure, the residual field in the cathode–collector grid gap (in the absence of a grid in the cathode–collector gap) is insufficient to initiate and maintain a discharge, which therefore completely concentrates near the cathode. Thus, in a high-pressure discharge, the collector detects the electron beam current.

Figure 2c shows voltage oscillograms measured at a helium pressure of 0.8 atm and a collector–cathode spacing of 5 mm. Here, the electron beam current is small: only a minor fraction of the beam electrons reach

the collector at $U \approx 6$ kV, since the electron mean free path [9] amounts to $l = 0.2U/p = 2$ mm. For the same reason, a small beam current ($j_c = 3$ A/cm^2) was observed at $U = 9$ kV and $p = 300$ Torr ($l = 6$ mm) with the collector grid and collector 5 and 10 mm from the cathode. In order to increase l further, the discharge should be additionally hindered, so that the breakdown takes place at still greater U.

Unfortunately, no grids with holes smaller than indicated above were available. For comparison, the experiment was performed with a grid of 1 mm period and $\mu = 0.85$. With this grid, the working pressure of helium was lower by a factor of 2–3. Therefore, we can hold that a decrease in the grid mesh ($A < 0.17$ mm) will lead to an increase in the working pressure (or in the l value). The problems of providing for a sufficiently high mechanical strength of the grid (at a given high transparency) and ensuring a tight contact between the grid and the dielectric surface (for large S) can be solved by forming the grid directly on the dielectric surface. This can be achieved, for example, by depositing a metal onto ceramics through a mask or by photolithographic processing of a deposited continuous metal layer.

Conclusions. A stable barrier open discharge operating under extremely hindered conditions in the proposed system allowed the working helium pressure admitting the electron beam formation to be increased by more than one order of magnitude (up to 0.8 atm) without any loss in the discharge stability. The required anode grids on a dielectric surface can also be obtained by vacuum deposition or photolithographic techniques. This will allow the range of working pressures to be extended toward higher values by further hindering the discharge through decreasing the anode grid hole size.

REFERENCES

1. A. R. Sorokin, Pis'ma Zh. Tekh. Fiz. **26** (24), 89 (2000) [Tech. Phys. Lett. **26**, 1114 (2000)].
2. K. A. Klimenko and Yu. D. Korolev, Zh. Tekh. Fiz. **60** (9), 138 (1990) [Sov. Phys. Tech. Phys. **35**, 1084 (1990)].
3. Yu. D. Korolev and G. A. Mesyats, *The Physics of Pulsed Discharge* (Nauka, Moscow, 1991).
4. V. M. Batenin, V. V. Buchanov, M. A. Kazaryan, *et al.*, in *Lasing on Self-Confined Transitions in Metal Atoms* (Nauchnaya Kniga, Moscow, 1998).
5. M. A. Zav'yalov, Yu. E. Kreĭndel', A. A. Novikov, and L. P. Shanturin, *Plasma Processes in Electron Guns* (Énergoatomizdat, Moscow, 1989).
6. A. V. Azarov, S. V. Mit'ko, and V. N. Ochkin, Kvantovaya Élektron. (Moscow) **32**, 675 (2002).
7. V. N. Ishchenko, V. N. Lisitsin, and A. R. Sorokin, Kvantovaya Élektron. (Moscow) **5**, 788 (1976).
8. G. V. Kolbychev, Opt. Atmos. Okeana **6** (6), 635 (1993).
9. A. A. Kudryavtsev and L. D. Tsendin, Pis'ma Zh. Tekh. Fiz. **27** (7), 46 (2001) [Tech. Phys. Lett. **27**, 284 (2001)].

Translated by P. Pozdeev

Technical Physics Letters, Vol. 29, No. 5, 2003, pp. 377–379. Translated from Pis'ma v Zhurnal Tekhnicheskoĭ Fiziki, Vol. 29, No. 9, 2003, pp. 51–57.

Nanometer Vibrations Measured Using a Semiconductor Laser on Quantum-Confined Structures Operating in an Autodyne Regime

D. A. Usanov* and A. V. Skripal'

Saratov State University, Saratov, Russia

** e-mail: UsanovDA@info.sgu.ru*

Received November 18, 2002

Abstract—A method for the quantitative monitoring of nanometer vibrations has been developed based on the autodyne detection effect in a semiconductor laser. It is shown that the semiconductor laser autodyne can be used for measuring the amplitudes of vibrations in a range from one nanometer to 10 μm in a frequency band from a few hertz to several hundred megahertz. With the aid of a lock-in amplifier, the lower threshold of measured vibration amplitudes has been reduced to one ångström. © *2003 MAIK "Nauka/Interperiodica".*

The application of semiconductor lasers operating in the IR range to measuring small-amplitude vibrations was described in [1–3]. Measuring systems of this type require a special device for aiming the laser beam at a given point of the object, which significantly complicates the system design. However, this difficulty can be naturally eliminated by using laser diodes based on quantum-confined structures operating in the visible spectral range [4–8]. This variant was studied in [9], where experiments were performed with a laser diode (SDL-7311-G1) based on an InGaAlP heterostructure.

We have experimentally studied the possibility of measuring vibrations of very small amplitudes using a laser diode of the RLD-650 type based on a quantum-confined structure with diffraction-limited solitary spatial mode. The laser parameters were as follows: output power, 5 mW; working wavelength, 652 nm; threshold current, 20 mA. A shorter wavelength of lasers operating in the visible range, in combination with the methods described in [1–4], gave us hope to reduce the lower threshold of measurable amplitudes of vibrations as compared to that for the systems employing IR lasers.

Figure 1 shows a schematic diagram of the autodyne measuring system based on a semiconductor laser. The semiconductor autodyne employed a laser diode of the RLD-650 type based on a quantum-confined InGaAlP heterostructure. The output radiation of the semiconductor laser *1* power supplied from source *2* strikes reflector *3* mounted on a $BaTiO_3$ piezoceramic transducer *4* excited by a acoustic-frequency generator *5*. The vibrating object can be moved with a micrometric mechanism *6*. A part of the radiation reflected from the object returns to the semiconductor laser cavity. The change in the output power is measured with photodetector *7*. The optical part of the system is mounted on a shockproof base effectively absorbing the external vibrations at frequencies above 5 Hz. The photodetector signal, passed via ac filter *8* and amplified by a broadband amplifier *9*, is processed by an analog-to-digital converter *10* and fed into computer *11* for data processing, storage, and display.

As is known, the wave returned to a laser cavity upon reflection from an external mirror changes the charge carrier density in the active medium. This, in turn, modifies the working optical frequency of the semiconductor laser. At a low feedback level, the relation between the laser diode radiation phase and the wave phase increment in the external resonator is linear [10, 11]. Therefore, the change in the frequency of the semiconductor laser as a result of the reflector motion can be ignored. The nor-

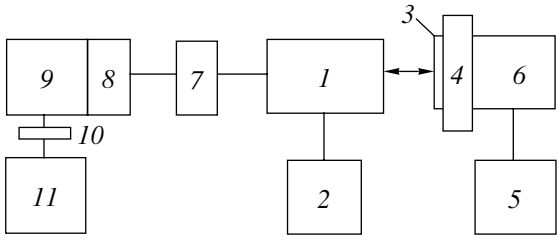

Fig. 1. A schematic diagram of the autodyne measuring system: (*1*) semiconductor laser; (*2*) power supply unit; (*3*) reflector; (*4*) piezoceramic transducer; (*5*) acoustic-frequency generator; (*6*) micrometric mechanism; (*7*) photodetector; (*8*) ac filter; (*9*) broadband amplifier; (*10*) analog-to-digital converter; (*11*) computer.

1063-7850/03/2905-0377$24.00 © 2003 MAIK "Nauka/Interperiodica"

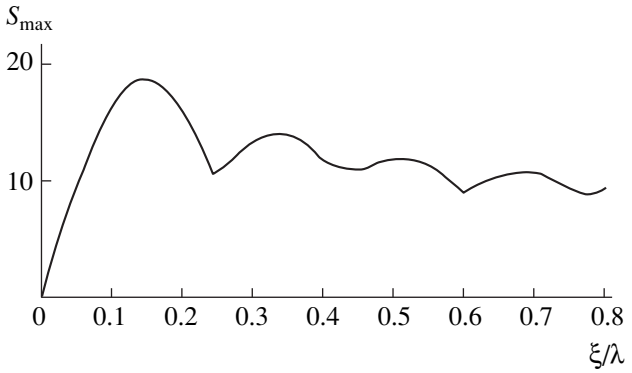

Fig. 2. A plot of the maximum harmonic amplitude S_{max} in the detected signal spectrum versus the normalized amplitude ξ/λ of the object vibrations.

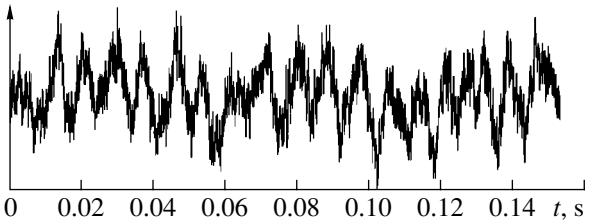

Fig. 3. A typical autodyne output signal from an object vibrating at a nanometer amplitude.

malized ac component of the autodyne signal will coincide with the signal detected in the interference system decoupled from the radiation source.

The radiation power $P(t)$ of a signal detected in the interference system, with one arm performing harmonic oscillations, can be expanded into a series with respect to the Bessel functions [12],

$$P(t) = \cos\theta J_0(\sigma) + 2\cos\theta \sum_{n=1}^{\infty} J_{2n}(\sigma)\cos[2n\omega t + \varepsilon] - 2\sin\theta \sum_{n=1}^{\infty} J_{2n-1}(\sigma)\cos[(2n-1)\omega t + \varepsilon], \quad (1)$$

where $\sigma = \frac{4\pi}{\lambda}\xi$, θ is the phase increment in the interference system, λ is the laser radiation wavelength, ξ and ω are the amplitude and frequency of mechanical vibrations of the object, J_n are the nth-order Bessel functions, n is the number of the harmonic spectral component of the detector signal, ε is the initial phase, and t is the current time.

As can be seen from relation (1), the detected signal comprises a constant component $\cos\theta J_0(\sigma)$, the main harmonic component, and higher order harmonics. For an object performing harmonic oscillations, the amplitudes of spectral components of the output signal of the autodyne system detector are proportional to the Bessel functions $J_{2n}(\sigma)$ and $J_{2n-1}(\sigma)$:

$$S_1 = 2J_1(\sigma)\sin\theta, \quad S_2 = 2J_2(\sigma)\cos\theta,$$
$$S_3 = 2J_3(\sigma)\sin\theta, \quad S_4 = 2J_4(\sigma)\cos\theta, \quad (2)$$
$$S_{2n-1} = 2J_{2n-1}(\sigma)\sin\theta, \quad S_{2n} = 2J_{2n}(\sigma)\cos\theta.$$

An increase in the amplitude ξ of the object vibrations leads to enrichment of the detected signal spectrum [13], whereby a harmonic with the maximum amplitude S_{max} shifts toward greater n. Figure 2 shows a plot of the maximum harmonic amplitude S_{max} in the detected signal spectrum versus the amplitude of the object vibrations normalized to the laser radiation wavelength. As can be seen, the curve exhibits clearly pronounced maxima. In the interval from 0 to 0.23λ, the maximum amplitude is observed for the harmonic coinciding with the frequency of vibrations of the object ($n = 1$); from $\sim 0.23\lambda$ to $\sim 0.44\lambda$, the maximum amplitude is observed for the second harmonic ($n = 2$), and so on. The knowledge of this dependence (in particular, of the positions of extrema) allows it to be used for the normalization of data.

The amplitude of vibrations of the object can be determined using the relation between the amplitudes of spectral components of the output signal of the autodyne system, which follows from Eqs. (2):

$$\frac{S_x}{S_n} = \frac{J_n\left(\frac{4\pi}{\lambda}\xi_x\right)}{J_n\left(\frac{4\pi}{\lambda}\xi\right)}, \quad (3)$$

where S_x is the amplitude of the nth harmonic, coinciding with the frequency of vibrations of the object, for the amplitude ξ_x of the reflector vibrations to be determined; S_n is the amplitude of the nth harmonic for the known reflector amplitude ξ. In the case when the unknown amplitude is smaller than 0.23λ, relation (3) can be rewritten as

$$\frac{S_x}{S_n} = \frac{J_1\left(\frac{4\pi}{\lambda}\xi_x\right)}{J_n\left(\frac{4\pi}{\lambda}\xi\right)}, \quad (4)$$

where J_1 is the first-order Bessel function. Relation (4) can be considered as an equation with respect to the variable ξ_x, since S_x and S_m are measurable quantities and the amplitude ξ is determined from the normalization curve (Fig. 2).

Figures 3 and 4 present examples of a photodetector signal and the corresponding spectrum for an object vibrating with an amplitude to be determined. Using the spectrum of Fig. 4, we have determined the amplitude $S_x = 0.3931$ rel. units of the harmonic corresponding to the object vibration frequency ($n = 1$) and mea-

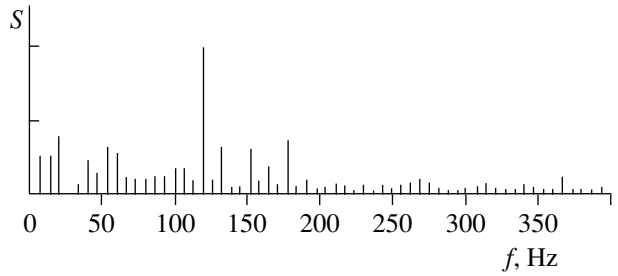

Fig. 4. Spectral representation of the autodyne signal from a vibrating object.

sured this frequency, which was equal to 120 Hz. In order to determine the unknown amplitude of vibrations, the object was subject to an additional mechanical action at a frequency equal to that of the object vibrations. The amplitude of the additional action was gradually increased until reaching the maximum value of the spectral harmonic at the object frequency. Upon determining this value, the amplitude of vibrations of the object under the action of additional mechanical vibrations was found using the theoretical dependence of the maximum harmonic amplitude on the object amplitude (Fig. 2).

Substituting the known amplitude of additional vibrations applied to the object (at the maximum of the first harmonic of the curve in Fig. 2) $\xi = 104$ nm into relation (4), we determine the unknown amplitude of vibrations of the object $\xi_x = 1.02$ nm. The measurement of lower amplitudes was limited by intrinsic noise of the setup schematically depicted in Fig. 1. It was established that the proposed autodyne scheme based on a semiconductor laser allows the amplitude of vibrations to be determined in the range from 1×10^{-3} to 10 μm in a frequency band from a few hertz to several hundred megahertz.

In order to increase the resolving power of the autodyne system based on the semiconductor laser, we used a lock-in amplifier of the U2-8 type. The results of our measurements showed that use of the lock-in scheme allows the lower threshold of measured vibration amplitudes to be reduced by one order of magnitude, so that the minimum level of measurable vibration amplitudes reached about one ångström.

Thus, we have demonstrated the possibility of using an autodyne laser meter for monitoring mechanical vibrations with nanometer amplitudes in a broad frequency range.

Acknowledgments. This study was supported by the Ministry of Education of the Russian Federation within the framework of the Program "Research of Higher School into Priority Directions of Science and Technology."

REFERENCES

1. D. A. Usanov, A. V. Skripal', A. Yu. Vagarin, *et al.*, Pis'ma Zh. Tekh. Fiz. **24** (5), 39 (1998) [Tech. Phys. Lett. **24**, 183 (1998)].
2. D. A. Usanov, Al. V. Skripal', and M. Yu. Kalinkin, Zh. Tekh. Fiz. **70** (2), 125 (2000) [Tech. Phys. **45**, 267 (2000)].
3. S. Donati, G. Giuliani, and S. Merlo, IEEE J. Quantum Electron. **QE-31**, 113 (1995).
4. D. A. Usanov, Al. V. Skripal', An. Skripal', *et al.*, Izv. Vyssh. Uchebn. Zaved., Priklad. Nelin. Dinam. **10** (3), 159 (2002).
5. Zh. I. Alferov, Fiz. Tekh. Poluprovodn. (St. Petersburg) **32**, 3 (1998) [Semiconductors **32**, 1 (1998)].
6. N. N. Ledentsov, V. M. Ustinov, V. A. Shchukin, *et al.*, Fiz. Tekh. Poluprovodn. (St. Petersburg) **32**, 385 (1998) [Semiconductors **32**, 343 (1998)].
7. A. E. Zhukov, A. R. Kovsh, V. M. Ustinov, *et al.*, Fiz. Tekh. Poluprovodn. (St. Petersburg) **33**, 1111 (1999) [Semiconductors **33**, 1013 (1999)].
8. Yu. A. Bykovskiĭ, K. B. Dedushenko, M. V. Zver'kov, and A. N. Mamaev, Kvantovaya Élektron. (Moscow) **9**, 657 (1992).
9. S. Merlo and S. Donati, IEEE J. Quantum Electron. **QE-33**, 527 (1995).
10. N. Shunc and K. Petermann, IEEE J. Quantum Electron. **QE-24**, 1242 (1988).
11. D. A. Usanov, A. V. Skripal', and M. Yu. Kalinkin, Izv. Vyssh. Uchebn. Zaved., Priklad. Nelin. Dinam. **6** (1), 3 (1998).
12. V. P. Koronkevich, V. S. Sobolev, and Yu. N. Dubintsev, *Laser Interferometry* (Nauka, Novosibirsk, 1983).
13. D. A. Usanov, A. V. Skripal', and V. A. Vagarin, Prib. Tekh. Éksp. **37**, 612 (1994).

Translated by P. Pozdeev

Technical Physics Letters, Vol. 29, No. 5, 2003, pp. 380–382. Translated from Pis'ma v Zhurnal Tekhnicheskoĭ Fiziki, Vol. 29, No. 9, 2003, pp. 58–63.

Nanodimensional Carbon Materials Formed in a Gas Discharge Plasma

A. A. Zolotukhin, A. N. Obraztsov*, A. P. Volkov, and A. O. Ustinov

Department of Physics, Moscow State University, Moscow, Russia

** e-mail: obraz@polly.phys.msu.ru*

Received December 15, 2002

Abstract—We have experimentally studied the formation of nanodimensional carbon materials from a methane–hydrogen gas mixture activated by a dc discharge. The range of discharge voltages and currents ensuring stable deposition of carbon films was determined. Data on the carbon-containing components of the activated gas phase were obtained by in situ optical emission spectroscopy of the gas discharge plasma. It is shown that the formation of nanodiamond and nanographite particles, as well as carbon nanotubes, in the deposited films is correlated with the presence of C_2 carbon dimers in the gas phase. A mechanism of the noncatalytic formation of carbon nanotubes from platelike graphite nanoparticles is proposed. © *2003 MAIK "Nauka/Interperiodica".*

We have studied the conditions of formation of nanodimensional carbon materials in the course of deposition from a methane–hydrogen gas mixture activated by a dc discharge. The experimental setup was described in detail elsewhere [1]. The electrical parameters (voltage *V* and total current *I*) of discharge could be varied using a controlled current source. The reaction chamber was provided with quartz windows, which allowed visual observation of the gas discharge plasma and the measurement of optical emission spectra of the plasma. The radiation emitted from plasma was focused onto a monochromator slit so that various regions of the interelectrode gap could be analyzed. The current–voltage characteristics and the optical emission spectra were measured for various gas phase pressures (varied from 10 to 150 Torr) and compositions (the methane content was varied from 0 to 25%).

Figure 1 shows the current–voltage characteristic of a dc discharge measured at a gas pressure of 60 Torr in a mixture containing 2% methane. The curve reveals four clearly distinguished regions, denoted by *A*, *B*, *C*, and *D*. Visual observations in the low-current region *A* (where the curve is characterized by negative slope), showed that the region of glow-discharge emission occupies only a part of the substrate (anode) surface. As the applied voltage increases, the charge "spreads" over the substrate so that the current density remains approximately constant. The negative slope of the *I–V* curve is indicative of a decrease in the total resistance of the interelectrode gap. The passage from region *A* to region *B* on the current–voltage characteristic corresponds to the charge spreading over the entire substrate (anode), followed by an increase in resistance of the anode–cathode gap. The resistance of the plasma column occupying the space between electrodes is determined by the competitive processes of ionization and charge carrier recombination, as well as by a change in the mean free path length (see, e.g., [4]) of charged particles in the gas phase. The interplay of various factors influencing the electric resistance of the plasma column accounts for a nonlinear shape of the *I–V* curve in region *B*. In region *C*, an increase in the discharge current (set by the power supply unit) takes place at a virtually unchanged voltage. This behavior, indicative of a significant decrease in resistance of the anode–cathode gap, can be explained by additional thermal ionization in the gap leading to an increase in the density of free charge carriers. As the current increases further, the *I–V* curve acquires a positive slope again, which corresponds to region *D* (Fig. 1). However, the discharge in this region

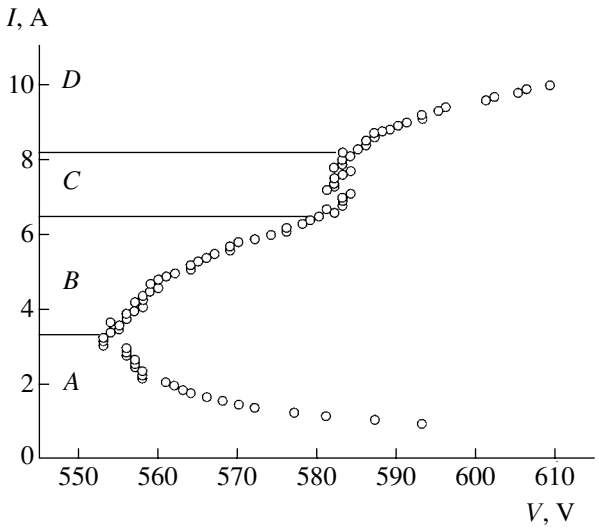

Fig. 1. The current–voltage characteristic of a dc discharge in a methane–hydrogen mixture at a total pressure of 60 Torr and a methane content of 2%.

1063-7850/03/2905-0380$24.00 © 2003 MAIK "Nauka/Interperiodica"

becomes unstable and converts into an arc at a certain combination of voltage and current. This regime depends on the total gas pressure and on the relative content of methane in the gas mixture. For example, in a mixture containing 2% methane at a pressure of 60 Torr, the critical discharge current was 10 A at a voltage of 620 V (Fig. 1).

Thus, regions *B* and *C* in the current–voltage characteristic represent the discharge parameters most favorable for the stable deposition of carbon films. On the whole, the *I–V* curves described above are typical of glow discharges (see, e.g., [2]). However, some characteristic values of the electrical parameters, important from the standpoint of the mechanisms of carbon deposition from the discharge plasma, were not previously reported.

Figure 2 shows the optical emission spectra of a gas discharge plasma measured for various methane concentrations (0 and 10% for Figs. 2a and 2b, respectively) in the same region close to the substrate (anode) surface, and for a mixture containing 25% methane, measured at the periphery of the emitting region (Fig. 2c). As can be seen from these data, the emission from a discharge in pure hydrogen (Fig. 2a) at V = 580 V and I = 6 A is mostly related to recombination transitions in atomic (H_β, 486 nm; H_α, 656 nm) and molecular hydrogen (H_2, 550–650 nm). After the introduction of methane, the discharge region acquires a yellow-green color with the characteristic emission spectrum (Fig. 2b) containing recombination lines due to CH radicals (386 and 422 nm) and C_2 dimers (515 and 560 nm). The shape of this spectrum (measured at V = 650 V and I = 6 A) and the positions of lines agree with the data reported previously for the methane–hydrogen plasma (see, e.g., [3]).

The intensities of lines due to the emission from atomic and molecular hydrogen remained virtually constant in all regions of the plasma column, while the intensities of lines related to the carbon-containing molecules (CH and C_2) significantly increased at the substrate surface as compared to the peripheral regions of discharge. When the content of methane exceeded 15%, the peripheral regions of the plasma column exhibited intense orange-yellow emission. The emission spectrum of such a region in a plasma containing 25% methane, measured at V = 700 V and I = 6 A, is presented in Fig. 2c. The relatively low intensity of the spectral lines and the structureless background emission gradually increasing with the wavelength indicate that the orange-yellow color is probably related to the presence of a condensed substance heated to a high temperature. This substance most likely represents a carbon soot formed as a result of carbon condensation from the gas phase. The condensation process, possible at a high methane content, results from the relatively cold peripheral plasma regions being oversaturated with carbon [3].

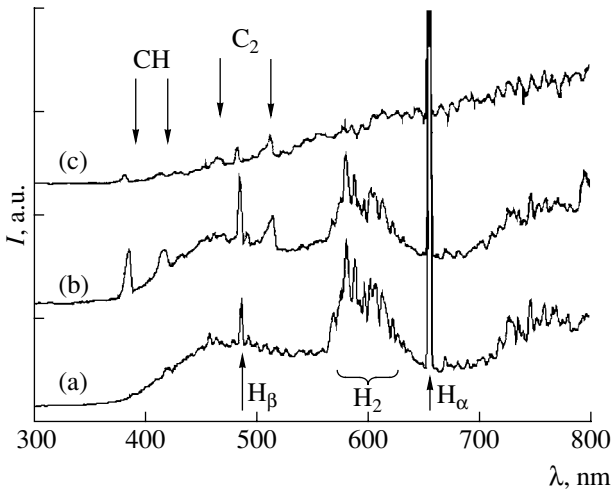

Fig. 2. Optical emission spectra of discharge plasmas in (a) pure hydrogen and (b, c) methane–hydrogen mixtures containing 10 and 25% of methane, respectively, measured at a total gas pressure of 60 Torr, a discharge current of I = 6 A, and a discharge voltage of V = 580 (a), 650 (b), and 700 V (c).

As was demonstrated previously, the concentration of methane in the gas phase is a determining factor for the synthesis of carbon films with various compositions and structures (see, e.g., [1, 2]). For example, polycrystalline diamond films can be obtain at a methane content from 0.1 to 2%. In the region of methane concentrations from 2 to 5%, the plasma deposition process yields so-called nanocrystalline diamond films. A graphitelike material composed of carbon nanotubes and graphite nanoparticles is possible for a methane content of 5–10%. When the methane concentration exceeds 15%, the deposit represents a disordered sootlike carbon material. In addition, the high content of methane in the gas phase makes the plasma deposition process unstable as a result of spontaneous discharge transition into an arc regime. The results of our observations establish conditions for the obtaining of various carbon films and the regions of parameters ensuring the stability of the deposition process.

The presence of carbon dimers revealed by the optical emission spectra may play a decisive role in the growth of nanocrystalline diamond (see, e.g., [5]). During the deposition of such dimers onto a substrate surface, an energetically favorable process is the growth of clusters in the form of linear atomic chains with acetylenelike bonds. Theoretical calculations showed that, after reaching a certain critical size, these clusters can transform into planar graphitelike carbon layers oriented perpendicularly to the substrate [5]. In a definite stage, these graphitelike layers can exhibit spontaneous (or induced by the deposition process parameters) fold-

ing with the formation of objects analogous to carbon nanotubes (or nuclei for the subsequent growth of such structures) [2]. This process, in contrast to the others used for the synthesis of carbon nanotubes (see, e.g., [2, 6]), does not require the presence of any catalysts.

Thus, we have established the relationship between the parameters of an activated methane–hydrogen gas mixture and the phase and structure of carbon films deposited from the related gas discharge plasma. The intervals of parameters of the gas discharge ensuring stable deposition have been determined. Carbon dimers C_2 have been found in the gas phase, and a mechanism of formation of nanostructural carbon particles has been proposed.

Acknowledgments. The work was supported by the INTAS Foundation (project no. 01-254).

REFERENCES

1. Yu. I. Pavlovskiĭ and A. N. Obraztsov, Prib. Tekh. Éksp. **41**, 152 (1998).
2. A. N. Obraztsov, A. P. Volkov, K. S. Nagovitsyn, *et al.*, J. Phys. D: Appl. Phys. **35**, 357 (2002).
3. B. V. Spitsyn, in *Handbook of Diamond Crystal Growth*, Ed. by D. T. J. Hurtle (Elsevier Science, Amsterdam, 1994), Vol. 3, pp. 403–456.
4. Yu. P. Raĭzer, *The Physics of Gas Discharge* (Nauka, Moscow, 1992), p. 536.
5. D. M. Gruen, Ann. Rev. Mater. Sci. **21**, 211 (1999).
6. Yu. E. Lozovik and A. M. Popov, Usp. Fiz. Nauk **167**, 751 (1997) [Phys. Usp. **40**, 159 (1997)].

Translated by P. Pozdeev

Technical Physics Letters, Vol. 29, No. 5, 2003, pp. 383–384. Translated from Pis'ma v Zhurnal Tekhnicheskoĭ Fiziki, Vol. 29, No. 9, 2003, pp. 64–68.

Thin Diamond Films for Integrated Circuits

V. K. Belyĭ, V. P. Varnin, S. A. Gavrilov, É. A. Il'ichev, É. A. Poltoratskiĭ*, G. S. Rychkov, and I. G. Teremetskaya

State Research Institute of Physical Problems, Zelenograd, Moscow oblast, Russia

** e-mail: polt@niifp.ru*

Institute of Physical Chemistry, Russian Academy of Sciences, Moscow, Russia

Received December 16, 2002

Abstract—We propose a technology for the synthesis of thin diamond films, which allows integrated emission elements of the vacuum triode type to be created on a substrate surface. The process includes three main stages: (i) deposition of a thin diamond film onto a silicon substrate; (ii) lithographic procedure with an aluminum mask; and (iii) post-growth in a regime ensuring required emission properties. An emission triode design is presented that can be realized using the proposed technology. *© 2003 MAIK "Nauka/Interperiodica".*

Polycrystalline and nanocrystalline diamond films [1, 2] deposited from a gas phase are of considerable interest from the standpoint of applications in micro- and nanoelectronics. These films possess unique properties, in particular, high values of the secondary and field electron emission. This offers a possibility of implementing the principles of vacuum electronics on the level of micro- and nanoelectronics. To this end, it is necessary to develop a technology for obtaining local micro- and nanodimensional emission regions. This paper proposes a solution of this problem.

The aforementioned problem can be solved by growing thin polycrystalline diamond films from an activated gas phase on a silicon substrate surface, followed by a lithographic procedure and the subsequent deposition of doped diamond or diamondlike layers ensuring effective field electron emission.

The polycrystalline diamond films were grown from a gas phase using a hot filament technique. According to this, the gas phase is activated, and a high concentration of atomic hydrogen is produced by heating a gas mixture up to a temperature of about 2000°C. In our experiments, the activator device comprised six parallel tungsten wires spaced by 3 mm, arranged 9 mm above a molybdenum holder with silicon substrates. The tungsten activator temperature, monitored by an optical micropyrometer, was about 2050°C when measured at a wavelength of $\lambda = 650$ nm. The table had a vertical channel with a diameter of about 1 mm, through which the temperature (typically about 850°C) of the rear surface of a silicon substrate could also be measured using the optical pyrometer.

The diamond films were deposited from a mixture of methane and/or acetone with hydrogen, at a total carbon content in the mixture of about 1%. The total pressure in the gas phase was 4×10^3 Pa at a hydrogen supply rate of 6 liters (STP) per hour. The gas mixture composition was controlled by setting a certain ratio of the mass flow rates of methane and hydrogen through the reactor. For introducing boron into the gas phase and depositing doped diamond films, a solution of trimethylborate in methyl alcohol was added into evaporated acetone. In order to obtain continuous diamond films of submicron thickness, the silicon substrates were inoculated with an ultradisperse diamond powder with an average particle size of about 5–10 nm. The average thickness of a deposit was estimated by measuring a change in the substrate weight before and after deposition to within 10 μg.

After the formation of a continuous diamond film on a silicon substrate, the sample surface was coated with an 0.1-μm-thick aluminum mask by direct or lift-off lithography. The diamond films were plasma-etched in a reactive ion etching setup of the 08PKhT-100T-005 type. The main reactant used for etching of the diamond and diamondlike films is oxygen, which can form volatile compounds with carbon. For this reason, the masking material was aluminum, which is known to form a stable Al_2O_3 surface film in oxygen containing media. The Al_2O_3 film also protected aluminum surface when a fluorine-containing compound (freon) was added to the oxygen plasma for increasing the rate of diamond film etching. The etching process was performed in an $O_2 + CF_4$ mixture (containing about 10% of CF_4) at a discharge power of 1.0 kW, frequency of 5.28 MHz, and a working pressure of 3–5 Pa. Under these conditions, the etching rate was 0.05–0.07 μm/min. The small values of the etching rate are explained by a low discharge density, determined by the large area of the substrate holder that served as the electrode.

In the course of etching the diamond film, it can also be necessary to produce etching of the silicon substrate, oxidize this surface, or cover it with a dielectric layer in order to electrically isolate silicon from metal conduc-

1063-7850/03/2905-0383$24.00 © 2003 MAIK "Nauka/Interperiodica"

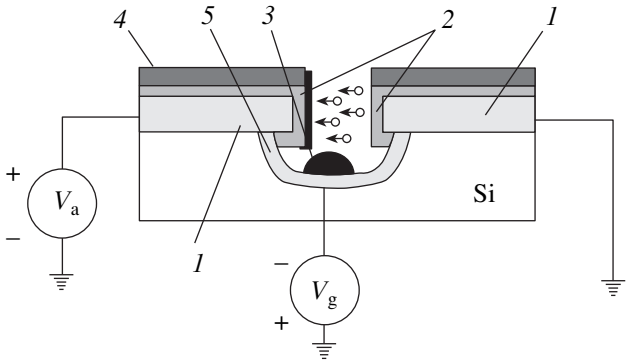

Fig. 1. The structure of a microvacuum transistor (see the text for explanations).

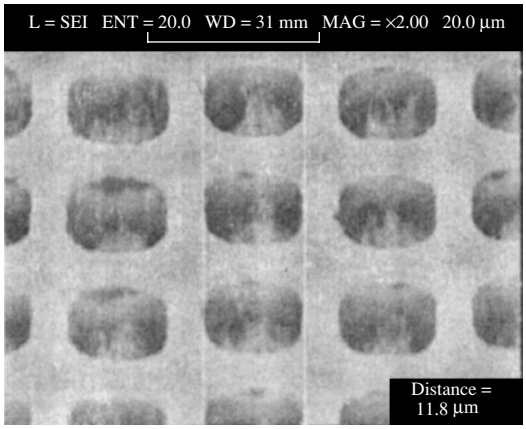

Fig. 2. A porous diamond membrane for two-dimensional electron flux amplifiers.

tors. After forming these conductors, additional diamond films are grown in a regime ensuring good field electron emission [3–5].

Figure 1 shows the structure of a microvacuum transistor that can be obtained using the proposed technology. This device comprises two local undoped diamond film regions *1* on the silicon surface. The free surface of these regions is covered with boron-doped diamond layer *2*, characterized by good electron emission properties. The local regions are separated by a gap, below which a gate *3* is formed during the oblique deposition of metal *4*. During this process, the edge of one local film region remains uncoated with the metal. This region acts as the edge electron emitter. Another local region acts as the anode, collecting electrons injected upon application of a voltage V_a. The gate *3* is situated on dielectric *5* in a cavity under the gap. At a submicron gap width, effective electron emission takes place even at $V_a \sim 1$–10 V. The flux of injected electrons is controlled by applying a negative potential V_g to gate *3*.

The proposed technology was checked by fabricating porous diamond membranes for two-dimensional electron flux amplifiers. In the first stage, a thin diamond film of the *i* type was deposited so as to form a grid (Fig. 2), which was subsequently overgrown by a *p*-type diamond film. The conducting film also covered the edge regions of the undoped diamond film. Thus, we have succeeded in realizing all technological operations necessary for creating microelectronic vacuum integrated circuits.

REFERENCES

1. V. P. Varnin, B. V. Deryagin, D. V. Fedoseev, *et al.*, Zh. Éksp. Teor. Fiz. **69**, 1250 (1975) [Sov. Phys. JETP **42**, 639 (1975)].
2. V. P. Varnin, B. V. Deryagin, D. V. Fedoseev, *et al.*, Kristallografiya **22**, 893 (1977).
3. T. Yamada, A. Sawabe, S. Roizumi, *et al.*, Phys. Status Solidi A, No. 2, 257 (2001).
4. A. R. Krauss, J. Auciello, M. Q. Ding, *et al.*, J. Appl. Phys. **89**, 2958 (2001).
5. A. V. Karabutov, R. A. Khmelnitsky, M. A. Negodaev, *et al.*, Diamond Relat. Mater. **10**, 2178 (2001).

Translated by P. Pozdeev

Technical Physics Letters, Vol. 29, No. 5, 2003, pp. 385–387. Translated from Pis'ma v Zhurnal Tekhnicheskoĭ Fiziki, Vol. 29, No. 9, 2003, pp. 69–74.

Growth of the Total Pressure Recovery Factor in a Flow Behind a Shock Wave Emerging from a Channel with Concave Corners in Cross Section

T. V. Bazhenova*, V. V. Golub, A. L. Kotel'nikov, A. S. Chizhikov, and M. V. Bragin

Institute for High Energy Densities, Associated Institute for High Temperatures, Russian Academy of Sciences, Moscow, Russia

** e-mail: bazhenova@ihed.ras.ru*

Received December 2, 2002

Abstract—Experimental data on the interaction of an obstacle with a shock wave emerging from a square channel with convex and concave corners in the cross section are considered. The flow structure was imaged by high-speed photography of shadow patterns. The total pressure losses in the flow were determined by measuring pressure at an obstacle oriented perpendicularly to the flow. It is established that the total pressure losses as a result of the flow drag upon efflux from the channel with X-shaped cross section are significantly lower as compared to the case of a channel with a round or square cross section. © *2003 MAIK "Nauka/Interperiodica".*

When a shock wave emerging from a channel strikes an obstacle, the first stage of the interaction is determined by the short-time action of the wave reflected from the obstacle, while the second stage is dominated by the action of the outflowing gas stream. As the distanced to the obstacle increases and the shock wave action decreases, the supersonic flow effect begins to prevail. The action of a supersonic flow upon the obstacle is reduced due to pressure losses at the drag shock [1]. Methods for creating an optimum shock wave system ensuring the obtaining of a maximum pressure recovery factor were theoretically studied in [2, 3]. The minimum losses can be attained for a flow geometry in which interaction of the rarefaction and compression waves leads to elimination of the normal shock wave.

It was established [4, 5] that the barrel-shaped structure of a supersonic jet depends on the shape of the nozzle cross section. The shape of the channel determines the structure of rarefaction fans, thus influencing the intensity and dimensions of the normal shock. The results of experiments and calculations for a 3D case showed that the interaction of rarefaction waves and pressure shocks upon the emergence of a shock wave from, for example, a square channel gives rise to a complicated unsteady 3D flow field in which the flow structure changes differently in various directions [6]. The diffraction of strong shock waves on a convex right angle upon emergence from a square channel leads to the formation of reduced pressure zones in the direction of square corners [7]. When a shock wave emerging from a square channel strikes an obstacle, the interference of rarefaction waves outgoing from convex corners of the channel and the increase in the Mach number in front of the drag shock favor an increase in the total pressure losses as compared to the case of a shock wave emerging from a round channel [8, 9].

We have studied the interaction of an obstacle with a shock wave emerging from a square channel with concave corners in the cross section (i.e., with a cross-shaped channel) throughout the length. The experimental setup comprised a shock tube connected to a cylindrical vacuum chamber. A flange with a round, square, or cross-shaped channel was fixed on the edge of the shock tube, so that the channel was accommodated inside the tube. The end of the shock tube was placed in front of the plane-parallel windows of a low-pressure chamber. The chamber contained a flat obstacle with a positioning mechanism that allowed the distance from the channel edge to obstacle to be varied. Initially, the low-pressure chamber and the vacuum chamber were filled with air to a pressure of $p_0 = 4.0$ kPa. The shock wave velocity was measured by the base method to within 1.2%.

For the comparison of the total pressure variation in the flow upon the shock wave emergence from the channels with different cross sections, equivalent distances from the channel edge to the obstacle were determined using the condition of equal effective gauges. For a round channel, the effective gauge d equals the circle diameter d_0; for a square or cross-shaped channel, the effective gauge is the diameter of a circle of equivalent area ($d = 1.125d_0$ and $1.08d_0$, respectively). For studying the interaction between the obstacle and a shock wave emerging from different channels, the obstacle was placed at a distance of four gauges from the channel edge.

1063-7850/03/2905-0385$24.00 © 2003 MAIK "Nauka/Interperiodica"

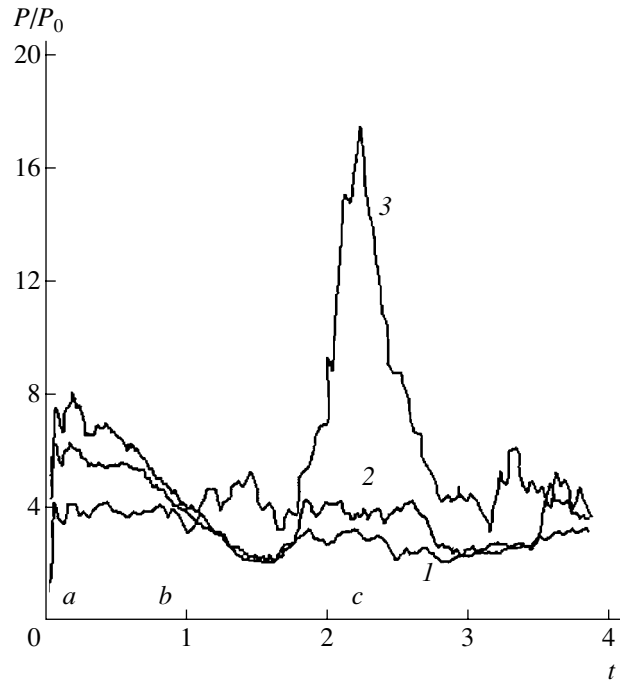

Fig. 1. Pressure oscillograms measured at the center of an obstacle interacting with a shock wave ($M_0 = 3.05$) emerging from a (*1*) square, (*2*) round, and (*3*) cross-shaped channel.

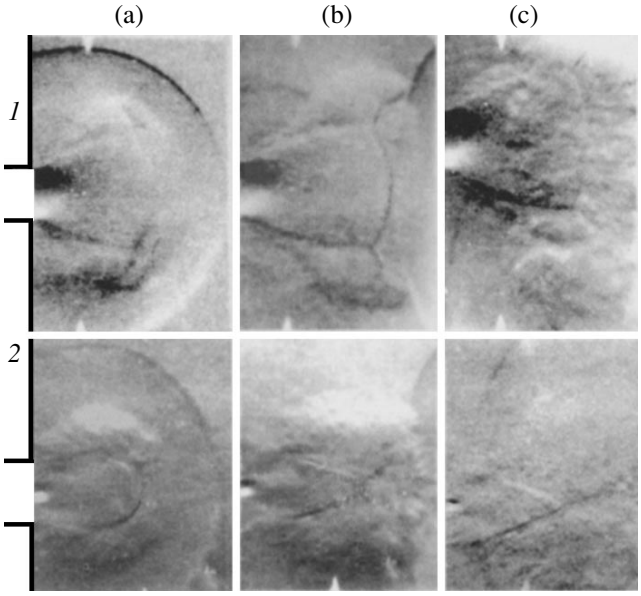

Fig. 2. Schlieren photographs illustrating the interaction of a obstacle with a shock wave emerging from a (*1*) round channel ($M_0 = 3.08$) and (*2*) cross-shaped channel ($M_0 = 2.80$): (a) before interaction; (b, c) at $t = 0.7$ and 2.2 after reflection of the shock wave front from the obstacle.

A pressure sensor of the Kistler 603B type was mounted on the obstacle at the center of the flow. The flow structure was visualized using a shadow device of the IAB-451 type and a high-speed optomechanical camera of the VSK-5 type. In order to determine the influence of the channel geometry on the total pressure losses upon the flow drag at the obstacle, we compared the corresponding pressure oscillograms and the schlieren photographs (Figs. 1 and 2). The comparison was performed in a dimensionless time t related to the dimensional variable as $t = (\tau/d)\sqrt{p_0/\rho_0}$, where p_0 and ρ_0 are the pressure and density of unperturbed gas.

The pressure oscillograms (Fig. 1) observed for the round and square channels exhibit the following common features: (*a*) pressure step, corresponding to the onset of interaction of the primary diffracted shock wave with the obstacle; (*b*) decay stage, corresponding to a change in parameters behind the reflected spherical shock wave; (*c*) constant parameters in a closed subsonic region bounded by the drag wave front, reflected shock wave, and the obstacle. For the shock wave emerging from a cross-shaped channel, the constant pressure in regions *a* and *b* is lower than those in the cases of round and square channels. In the region *c*, the pressure upon efflux from the square channel is 27% lower than that for the round channel (this was previously reported in [10]), while the pressure for the cross-shaped channel in this region is four times the value for the round channel.

A comparison between the pressure oscillograms and the schlieren photographs showed that, by the moment of pressure buildup upon emergence from the cross-shaped channel, the flow structure is free from a normal shock wave (in contrast to the cases of round and square channels (Fig. 2)).

The ratio of the total pressure at the obstacle to that at the channel edge characterized the total pressure loss in the system of shock waves formed during the interaction of an obstacle with a diffracted shock wave and the wake stream. The total pressure in the flow at the channel edge is determined from the Mach number of the cocurrent flow behind the incident shock wave (this number is a known function of the measured initial Mach number in the shock wave). In the case under consideration, the total pressure recovery factor for a shock wave emerging from square, round, and cross-shaped channels was 0.09, 0.12, and 0.6, respectively.

The above relations show the possibility of controlling the total pressure in the flow upon the shock wave emergence from a channel by modifying the shape of the channel cross section.

Acknowledgments. This study was partly supported by the Russian Foundation for Basic Research, project no. 01-01-00664.

REFERENCES

1. V. G. Dulov and G. A. Luk'yanov, *Gasdynamics of Efflux Processes* (Nauka, Novgorod, 1984).

2. A. V. Omel'chenko and V. N. Uskov, Izv. Akad. Nauk, Mekh. Zhidk. Gaza, No. 6, 118 (1995).
3. V. N. Malozemov, A. V. Omel'chenko, and V. N. Uskov, Prikl. Mat. Mekh. **62**, 1014 (1998).
4. V. V. Golub, I. M. Naboko, and A. A. Kulikovskiĭ, Prikl. Mekh. Tekh. Fiz., No. 1, 41 (1976).
5. K. Teshima, *Proceedings of the 1989 National Symposium on Shock Wave Phenomena* (Tohoku University, 1989), pp. 135–143.
6. T. V. Bazhenova, S. B. Bazarov, and V. V. Golub, Izv. Akad. Nauk, Mekh. Zhidk. Gaza, No. 1, 200 (1993).
7. T. V. Bazhenova, V. V. Golub, and T. A. Bormotova, Izv. Akad. Nauk, Mekh. Zhidk. Gaza, No. 3, 114 (1999).
8. T. V. Bazhenova, T. A. Bormotova, and V. V. Golub, Pis'ma Zh. Tekh. Fiz. **27** (16), 10 (2001) [Tech. Phys. Lett. **27**, 669 (2001)].
9. T. V. Bazhenova, V. V. Golub, and T. A. Bormotova, Teplofiz. Vys. Temp. **39** (1), 124 (2001).
10. T. V. Bazhenova, T. A. Bormotova, and V. V. Golub, Teplofiz. Vys. Temp. **40** (2), 250 (2002).

Translated by P. Pozdeev

Technical Physics Letters, Vol. 29, No. 5, 2003, pp. 388–391. Translated from Pis'ma v Zhurnal Tekhnicheskoĭ Fiziki, Vol. 29, No. 9, 2003, pp. 75–82.

Internal Nonlinear Four-Mode Interactions of Capillary Oscillations of a Charged Drop

A. N. Zharov, A. I. Grigor'ev*, and S. O. Shiryaeva

Yaroslavl State University, Yaroslavl, Russia

** e-mail: grig@uniyar.ac.ru*

Received December 2, 2002

Abstract—Analytical expressions for the shape of a charged drop of an incompressible liquid nonlinearly oscillating upon multimode initial deformation have been obtained for the first time to within the third order of smallness. The second-order corrections to oscillation frequencies are calculated depending on the spectrum of modes determining the initial deformation. The third-order calculations show that the fundamental mode amplitude may increase due to the energy exchange with higher modes in a large number of possible four-mode resonance interactions. © *2003 MAIK "Nauka/Interperiodica".*

The nonlinear oscillations of charged drops have been a subject of extensive investigation, which have revealed a number of phenomena not encountered in the linear theory (see, e.g., [1–10] and references therein). However, there are many questions requiring cumbersome calculations that are still beyond the framework of this research. Most of the previous investigations in this direction were performed to within the second order of smallness with respect to the initial perturbation amplitude. Tsamopoulos and Brown [1, 2] accomplished a third-order calculation and obtained nonlinear corrections to the oscillation frequencies in some particular cases of single-mode initial deformations, but the final solution was written only to within the second order of smallness, leaving the four-mode resonances outside the scope of investigation. Moreover, the frequency corrections reported in [1, 2] also cannot be used without refinement, since the papers contain misprints which can be proved only by repeating all computations [2]. Unfortunately, this is hindered by a brief description of the calculation procedure.

Below, we present the results of calculations performed to within the third order of smallness for a drop oscillating upon multimode initial deformation.

Formulation of the problem. Consider a drop of the ideal, incompressible, and perfectly conducting liquid with density ρ and surface tension σ, bearing a total charge of Q and performing axisymmetric oscillations about an equilibrium sphere of radius R. The aim is to obtain an expression describing the drop shape at an arbitrary time.

Mathematical formulation of the problem is completely analogous to that presented in [8–10], where the problem was solved to within the second order of smallness. For this reason, we will only present a final solution that can be obtained by the asymptotic multiscale method. In the dimensionless variables such that $\rho = R = \sigma = 1$, expressions describing the drop surface in a spherical coordinate system (r, ϑ) to within the third order of smallness with respect to the initial perturbation amplitude are as follows:

$$r(\vartheta, t) = 1 + \varepsilon \sum_{n \in \Omega} M_n^{(1)}(t) P_n(\cos\vartheta) + \varepsilon^2 \sum_{n=0}^{\infty} (M_n^{(2)}(t) + \varepsilon M_n^{(3)}(t)) P_n(\cos\vartheta); \quad (1)$$

$$M_n^{(1)}(t) = h_n \cos(\omega_n t + \varepsilon^2 b_n t); \quad n \in \Omega;$$

$$b_n = \frac{1}{2\omega_n}\left\{ \sum_{k \in \Omega} \frac{h_k^2 \Xi_n}{2(2k+1)} + \frac{h_n^2 (2(n-1)\omega_n^2 + \Xi_n)}{4(2n+1)} \right.$$

$$- \frac{\chi_{n-1} h_{n-1}^2}{4} (\beta^{2(+)}_{n-1,\,n,\,1,\,n-1,\,n} + \beta^{2(-)}_{n-1,\,n,\,1,\,n-1,\,n})$$

$$- \frac{\chi_n h_{n+1}^2}{4} (\beta^{1(-)}_{n+1,\,n+1,\,1,\,n,\,n} + \beta^{2(+)}_{n+1,\,n+1,\,1,\,n,\,n})$$

$$- \sum_{k \in \Omega} \frac{h_k^2}{4} [H^{1(-)(+)}_{nkkn} + H^{2(+)(+)}_{knkn} + H^{2(-)(-)}_{knkn}$$

$$\left. + (1 - \delta_{kn})(H^{1(-)(+)}_{kknn} + H^{2(+)(+)}_{kknn} + H^{2(-)(-)}_{nkkn})] \right\};$$

$$n \in \Omega;$$

$$M_0^{(2)}(t) = -\sum_{k \in \Omega} \frac{h_k^2 \cos^2(\omega_k t)}{2k+1};$$

$$M_1^{(2)}(t) = \sum_{k \in \Omega} \chi_k h_k h_{k+1} \cos(\omega_k t) \cos(\omega_{k+1} t);$$

$$M_n^{(2)}(t) = \sum_{k, m \in \Omega} \frac{h_k h_m}{2} (\lambda_{kmn}^{(+)} \cos((\omega_k + \omega_m)t)$$

$$+ \lambda_{kmn}^{(-)} \cos((\omega_k - \omega_m)t) - (\lambda_{kmn}^{(+)} + \lambda_{kmn}^{(-)}) \cos(\omega_n t));$$

$$M_0^{(3)}(t) = -\sum_{k \in \Omega} \frac{2M_k^{(2)}}{2k+1} h_k \cos(\omega_k t)$$

$$- \sum_{k, m, l \in \Omega} \frac{K_{kml} h_k h_m h_l}{3(2l+1)} \cos(\omega_k t) \cos(\omega_m t) \cos(\omega_l t);$$

$$M_1^{(3)}(t) = -\frac{6}{5} M_1^{(2)}(t) h_2 \cos(\omega_2 t)$$

$$- 3 \sum_{k=0}^{\infty} \sum_{m \in \Omega} K_{km1} M_k^{(2)}(t) h_m \cos(\omega_m t)$$

$$- \sum_{g=0}^{\infty} \sum_{k, m, l \in \Omega} K_{kmg} K_{gl1} h_k h_m h_l \cos(\omega_k t)$$

$$\times \cos(\omega_m t) \cos(\omega_l t);$$

$$M_n^{(3)}(t) = -\sum_{k \in \Omega} \frac{h_n h_k^2 (2(n-1)\omega_n \omega_k - \Xi_n)}{16(2k+1)\omega_k(\omega_n + \omega_k)}$$

$$\times (\cos((\omega_n + 2\omega_k)t) - \cos(\omega_n t))$$

$$- \sum_{k \in \Omega} \frac{h_n h_k^2 (2(n-1)\omega_n \omega_k + \Xi_n)}{16(2k+1)\omega_k(\omega_n - \omega_k)}$$

$$\times (\cos((\omega_n - 2\omega_k)t) - \cos(\omega_n t))$$

$$+ \sum_{k=n-1}^{n+1} \sum_{l \in \Omega} \frac{\chi_l h_k h_l h_{l+1}}{4}$$

$$\times \left\{ \frac{\beta_{k, l+1, 1, l, n}^{1(+)} (\cos(\psi_{k, l, l+1}^{(+)(+)} t) - \cos(\omega_n t))}{(\omega_n^2 - (\omega_k + \omega_l + \omega_{l+1})^2)} \right.$$

$$+ \frac{\beta_{k, l+1, 1, l, n}^{1(-)} (\cos(\psi_{k, l, l+1}^{(+)(-)} t) - \cos(\omega_n t))}{(\omega_n^2 - (\omega_k + \omega_l - \omega_{l+1})^2)}$$

$$+ \frac{\beta_{k, l+1, 1, l, n}^{2(+)} (\cos(\psi_{k, l, l+1}^{(-)(-)} t) - \cos(\omega_n t))}{(\omega_n^2 - (\omega_k - \omega_l - \omega_{l+1})^2)}$$

$$\left. + \frac{\beta_{k, l+1, 1, l, n}^{2(-)} (\cos(\psi_{k, l+1, l}^{(+)(-)} t) - \cos(\omega_n t))}{(\omega_n^2 - (\omega_k - \omega_l + \omega_{l+1})^2)} \right\}$$

$$- \sum_{g=2k}^{\infty} \sum_{k, m, l \in \Omega} \frac{h_k h_m h_l (\lambda_{lmg}^{(+)} + \lambda_{lmg}^{(-)})}{4}$$

$$\times \left\{ \frac{H_{kgn}^{0(+)} (\cos((\omega_k + \omega_g)t) - \cos(\omega_n t))}{\omega_n^2 - (\omega_k + \omega_g)^2} \right.$$

$$\left. + \frac{H_{kgn}^{0(-)} (\cos((\omega_k - \omega_g)t) - \cos(\omega_n t))}{\omega_n^2 - (\omega_k - \omega_g)^2} \right\}$$

$$+ \sum_{k, m, l \in \Omega} \frac{h_k h_m h_l}{4} \left\{ \frac{H_{kmln}^{1(+)(-)} (\cos(\psi_{klm}^{(+)(+)} t) - \cos(\omega_n t))}{\omega_n^2 - (\omega_k + \omega_l + \omega_m)^2} \right.$$

$$+ \frac{H_{kmln}^{1(-)(+)} (\cos(\psi_{klm}^{(+)(-)} t) - \cos(\omega_n t))}{\omega_n^2 - (\omega_k + \omega_l - \omega_m)^2}$$

$$+ \frac{H_{kmln}^{2(+)(+)} (\cos(\psi_{klm}^{(-)(-)} t) - \cos(\omega_n t))}{\omega_n^2 - (\omega_k - \omega_l - \omega_m)^2}$$

$$\left. + \frac{H_{kmln}^{2(-)(-)} (\cos(\psi_{kml}^{(+)(-)} t) - \cos(\omega_n t))}{\omega_n^2 - (\omega_k - \omega_l + \omega_m)^2} \right\};$$

$$\psi_{kml}^{(+)(+)} = \omega_k + \omega_m + \omega_l; \quad \psi_{kml}^{(+)(-)} = \omega_k + \omega_m - \omega_l;$$

$$\psi_{kml}^{(-)(-)} = \omega_k - \omega_m - \omega_l;$$

where ε is a small parameter characterizing the amplitude of the initial deformation; $P_n(\cos\vartheta)$ is the Legendre polynomial of the nth order; t is the current time; h_n is a constant describing the partial contribution of the nth mode to the initial deformation of the equilibrium spherical drop; and Ω is the set of mode numbers determining the initial deformation. Determination of the coefficients entering into Eqs. (1) is described in Appendix.

Analysis of the solution. As can be readily seen from expressions (1) for the correction b_n to the oscillation frequency ω_n of the capillary modes, this correction depends not only on the nth mode amplitude in the initial deformation but on the amplitudes of all other modes determining this initial deformation. The expressions for $M_n^{(3)}(t)$, representing the nonlinear third-order corrections to the excited mode amplitudes, exhibit a resonance character manifested by the denominators going to zero under certain conditions. All the new resonances (in addition to those obtained in the quadratic approximation) correspond to the four-mode interaction between capillary oscillations, whereby the frequencies of modes featuring the resonance interaction are related as $\omega_n \pm \omega_k \pm \omega_m \pm \omega_l = 0$ [11].

Among the numerous nonlinear resonances realized in the oscillating drop, of most interest from the stand-

point of the problem of a lighting discharge initiation in a stormy cloud [12] are those for which the fundamental mode ($n = 2$) of the drop with a subcritical charge (i.e., with a small parameter $W = Q^2/4\pi$) grows due to the resonance interaction with the higher modes. Our previous calculation [10] of the nonlinear three-mode resonances to within the second order of smallness showed that, for a drop of an ideal liquid bearing a subcritical charge, the fundamental mode exhibits no resonance interaction with the higher modes. A different pattern is observed for the four-mode interactions calculated to within the third order of smallness. For a drop with subcritical W for the fundamental mode ($W < 4$), for which only interactions of the first nine modes are taken into account ($2 \le n, m, k, l \le 10$) with resonances of the type $\omega_n - \omega_m - \omega_k - \omega_l = 0$, there are 15 resonance situations whereby the fundamental mode is involved into the resonance interaction, and the amplitude of this mode can increase due to the resonance energy pumping from the higher modes.

Conclusion. An analysis of the four-mode interaction of capillary oscillations of a drop, as manifested in the third of order of smallness with respect to the multimode initial perturbation amplitude, reveals the conditions of the resonance buildup of the fundamental mode amplitude due to the energy pumping from higher modes.

APPENDIX

$$H^{1(+)(-)}_{kmln} = \sum_{g=2}^{\infty} \beta^{1(+)}_{kmgln}\lambda^{(+)}_{lmg} + \sum_{g=1}^{\infty} \mu^{1(-)}_{kmgln} + \sum_{g=0}^{\infty} \mu^{0(-)}_{kmgln};$$

$$H^{1(-)(+)}_{kmln} = \sum_{g=2}^{\infty} \beta^{1(-)}_{kmgln}\lambda^{(-)}_{lmg} + \sum_{g=1}^{\infty} \mu^{1(+)}_{kmgln} + \sum_{g=0}^{\infty} \mu^{0(+)}_{kmgln};$$

$$H^{2(+)(+)}_{kmln} = \sum_{g=2}^{\infty} \beta^{2(+)}_{kmgln}\lambda^{(+)}_{lmg} + \sum_{g=1}^{\infty} \mu^{1(+)}_{kmgln} + \sum_{g=0}^{\infty} \mu^{0(+)}_{kmgln};$$

$$H^{2(-)(-)}_{kmln} = \sum_{g=2}^{\infty} \beta^{2(-)}_{kmgln}\lambda^{(-)}_{lmg} + \sum_{g=1}^{\infty} \mu^{1(-)}_{kmgln} + \sum_{g=0}^{\infty} \mu^{0(-)}_{kmgln};$$

$$H^{0(+)}_{kgn} = (\Pi^0_{kgn} - \Pi^1_{kgn}\omega_k\omega_g - \Pi^2_{kgn}\omega_g^2);$$

$$H^{0(-)}_{kgn} = (\Pi^0_{kgn} + \Pi^1_{kgn}\omega_k\omega_g - \Pi^2_{kgn}\omega_g^2);$$

$$\beta^{1(+)}_{kmgln} = \Pi^0_{kgn} - \Pi^1_{kgn}\omega_k(\omega_l + \omega_m) - \Pi^2_{kgn}(\omega_l + \omega_m)^2;$$

$$\beta^{1(-)}_{kmgln} = \Pi^0_{kgn} - \Pi^1_{kgn}\omega_k(\omega_l - \omega_m) - \Pi^2_{kgn}(\omega_l - \omega_m)^2;$$

$$\beta^{2(+)}_{kmgln} = \Pi^0_{kgn} + \Pi^1_{kgn}\omega_k(\omega_l + \omega_m) - \Pi^2_{kgn}(\omega_l + \omega_m)^2;$$

$$\beta^{2(-)}_{kmgln} = \Pi^0_{kgn} + \Pi^1_{kgn}\omega_k(\omega_l - \omega_m) - \Pi^2_{kgn}(\omega_l - \omega_m)^2;$$

$$\mu^{1(-)}_{kmgln} = \Lambda^1_{kmgln} - \Gamma^1_{kmgln}\omega_m\omega_k;$$

$$\mu^{1(+)}_{kmgln} = \Lambda^1_{kmgln} + \Gamma^1_{kmgln}\omega_m\omega_k;$$

$$\mu^{0(-)}_{kmgln} = \Lambda^0_{kmgln} - \Gamma^0_{kmgln}\omega_m\omega_k;$$

$$\mu^{0(+)}_{kmgln} = \Lambda^1_{kmgln} + \Gamma^0_{kmgln}\omega_m\omega_k;$$

$$\Lambda^0_{kmgln}$$

$$= \frac{1}{2k}\Big\{K_{gln}(\alpha_{kmg}(kn(l + 3l^2 - 2(k+2)W) + 2(k-2)\omega_k^2))$$

$$+ K_{kmg}(kn(4 - 6k(k+1) + (k^3 - 2(m+1)(m+2)$$

$$- k^2(n-9) - k(3n + 2m(m+3) - 22))W)$$

$$- (k-1)k(k-n-2)\omega_k^2))$$

$$- 2kn\alpha_{kmg}\sum_{\nu=1}^{[l/2]}(2l - 4\nu + 1)K_{g,\,l-2\nu,\,n}\Big\};$$

$$\Lambda^1_{kmgln} = ((g-n-1)K_{gln} - \alpha_{gln}/g)$$

$$\times((m-1)K_{kmg} - \alpha_{kmg}/m)\omega_m^2$$

$$+ Wnk((g+1)(l+n-g-2)K_{gln} + \alpha_{gln})K_{kmg};$$

$$\Gamma^0_{kmgln} = ((k-1)(k-2(n+1))K_{kmg}/2$$

$$- ((k-1)(m+n) - m)\alpha_{kmg}/(km))K_{gln}$$

$$+ ((k-1)(k-2)K_{kgl}/2 - (k-2)\alpha_{klg}/k)K_{gmn};$$

$$\Gamma^1_{kmgln} = -((g-n-1)K_{gkn} - (n+k)\alpha_{gkn}/(kg))$$

$$\times((m-1)K_{lmg} - \alpha_{lmg}/m) - ((g-n-1)K_{gln} - \alpha_{gln}/g)$$

$$\times((m-1)K_{kmg} - \alpha_{kmg}/m);$$

$$\Pi^0_{kmn} = K_{kmn}(\omega_k^2(n-k+1) + 2kn(k+1)$$

$$+ 2mn(m+1) - 4n + nW((n-k-5)(k-1)$$

$$+ (m+1)(k+n-m-2))) + (\omega_k^2/k + nW)\alpha_{kmn};$$

$$\Pi^1_{kmn} = (m+k-n-2)K_{kmn}$$

$$- (n+k+m)\alpha_{kmn}/(mk);$$

$$K_{mln} = (C^{n0}_{m0l0})^2;$$

$$\Pi^2_{kmn} = (m-n-1)K_{kmn} - \alpha_{kmn}/m;$$

$$\chi_k = -9(k+1)/((2k+1)(2k+3));$$

$$\Xi_k = \omega_k^2 + 2k^2(k+1) - 4k - 5k(k-1)W;$$

$$W = Q^2/(4\pi); \quad \omega_k^2 = k(k-1)(k+2-W);$$

$$\lambda_{mln}^{(\pm)} = (\gamma_{mln} \pm \omega_m \omega_l \eta_{mln})/(\omega_n^2 - (\omega_m \pm \omega_l)^2);$$

$$\alpha_{mln} = -C_{m0l0}^{n0} C_{m(-1)l1}^{n0} \sqrt{m(m+1)l(l+1)};$$

$$\gamma_{mln} = K_{mln}[\omega_m^2(n-m+1) + 2n(l(l+1)-1) + (l(m+1) - m(2m-2n+7) + 3)nW/2] + \alpha_{mln}[\omega_m^2/m + nW/2];$$

$$\eta_{mln} = K_{mln}(n/2 - m + 1) + \alpha_{mln}(1 + n/(2l))/m;$$

C_{m0l0}^{n0} and $C_{m,-1,l,1}^{n0}$ are the Clebsch–Gordan coefficients [13].

Acknowledgments. This study was supported by Presidential Grant No. 00-15-9925.

REFERENCES

1. J. A. Tsamopoulos and R. A. Brown, J. Fluid Mech. **127**, 519 (1983).
2. J. A. Tsamopoulos and R. A. Brown, J. Fluid Mech. **147**, 373 (1984).
3. N. A. Pelekasis, J. A. Tsamopoulos, and G. D. Manolis, Phys. Fluids A **2**, 1328 (1990).
4. T. G. Wang, A. V. Anilkumar, and C. P. Lee, J. Fluid Mech. **308**, 1 (1996).
5. Z. Feng, J. Fluid Mech. **333**, 1 (1997).
6. D. F. Belonozhko and A. I. Grigor'ev, Zh. Tekh. Fiz. **70** (8), 45 (2000) [Tech. Phys. **45**, 1001 (2000)].
7. S. O. Shiryaeva, Zh. Tekh. Fiz. **71** (2), 27 (2001) [Tech. Phys. **46**, 158 (2001)].
8. S. O. Shiryaeva, Izv. Akad. Nauk, Mekh. Zhidk. Gaza, No. 3, 173 (2001).
9. S. O. Shiryaeva, Zh. Tekh. Fiz. **72** (4), 15 (2002) [Tech. Phys. **47**, 389 (2002)].
10. S. O. Shiryaeva, D. F. Belonozhko, and A. I. Grigor'ev, Pis'ma Zh. Tekh. Fiz. **28** (22), 45 (2002) [Tech. Phys. Lett. **28**, 945 (2002)].
11. O. M. Phillips, J. Fluid Mech. **106**, 215 (1981).
12. A. I. Grigor'ev and S. O. Shiryaeva, Phys. Scr. **54**, 660 (1996).
13. D. A. Varshalovich, A. N. Moskalev, and V. K. Khersonskii, *Quantum Theory of Angular Momentum* (Nauka, Leningrad, 1975; World Scientific, Singapore, 1988).

Translated by P. Pozdeev

Technical Physics Letters, Vol. 29, No. 5, 2003, pp. 392–394. Translated from Pis'ma v Zhurnal Tekhnicheskoĭ Fiziki, Vol. 29, No. 9, 2003, pp. 83–88.

The Effect of Ultrasonic Treatment on the Generation Characteristics of a Si–SiO_2 Interface

P. B. Parchinskii*, S. I. Vlasov, L. G. Ligaĭ, and O. Yu. Shchukina

National University of Uzbekistan, Tashkent, Uzbekistan

** e-mail: pavelphys@mail.ru*

Received January 8, 2003

Abstract—We have studied the effect of ultrasonic treatment on the generation characteristics of a silicon–silicon dioxide (Si–SiO_2) interface obtained by thermal oxidation of the surface of silicon. The ultrasonic treatment leads to a decrease in the surface generation rate and an increase in the generation lifetime of minority charge carriers. These effects are related to a transformation of the defect structure of a transition layer at the Si–SiO_2 interface and in the adjacent region of silicon. *© 2003 MAIK "Nauka/Interperiodica".*

Now it is commonly accepted that ultrasound significantly influences the defect structure and electrical properties of semiconductors and related structures [1–4]. The effects produced by this factor are most clearly manifested in the regions of semiconductor structures featuring internal stresses [3, 4]. The presence of stress fields is a factor favoring the process of formation, rearrangement, and recombination of structural defects under the action of ultrasound. In this context, it is of interest to study the effect of an ultrasonic treatment on the properties of a Si–SiO_2 interface, which is characterized by the presence of a strongly stressed transition layer [5].

We have studied the effect of ultrasonic treatment on the generation characteristics of a Si–SiO_2 interface obtained by thermal oxidation of the surface of a ⟨100⟩ oriented *n*-type silicon single crystal with a resistivity of 0.3 Ω cm. The oxidation process was conducted in dry oxygen at 1000°C. The generation characteristics of the Si–SiO_2 interface were studied by the method of isothermal relaxation of capacitance, which provides data on the surface generation rate S_g and the generation lifetime τ_g in the region of silicon adjacent to the interface [6, 7].

The measurements were performed on test structures of the metal–insulator–semiconductor (MIS) type prepared by the vacuum deposition of aluminum onto SiO_2 layer. The structures were treated by ultrasound for 45 min at a frequency of 2.5 MHz and a power density of 0.5 W/cm^2. The process of relaxation of a nonequilibrium capacitance in thus treated MIS structures was studied using a 150 MHz probing signal. The measurements were performed at a temperature of 0°C in the dark. The nonequilibrium depleted state was created by switching the applied voltage from –16 to –20 V, which converted the sample from the state of inversion to that of a stronger inversion. This regime of measurements was selected because it allowed us to ignore the contribution due to the recharge of surface states in the course of relaxation of the nonequilibrium capacitance of the MIS structure, thus increasing the accuracy of measurements and making the data interpretation less ambiguous [8].

Figure 1 shows typical relaxation curves observed for one of the MIS structures studied before and after the ultrasonic treatment. As can be seen, the treatment increases the time of relaxation of the nonequilibrium capacitance of the MIS structure, which is indicative of a decrease in the rate of the minority carrier generation.

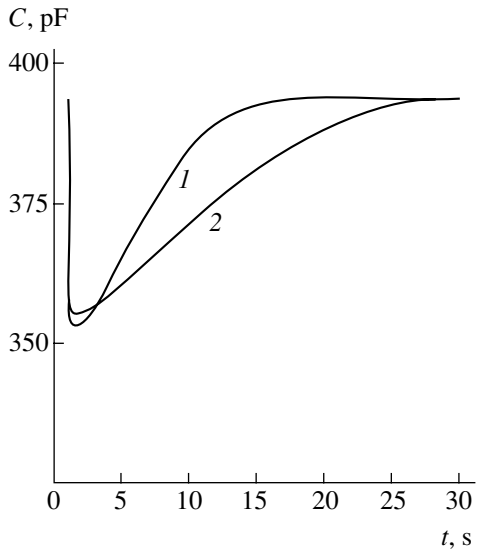

Fig. 1. Relaxation of the nonequilibrium capacitance of the MIS structures (*1*) before and (*2*) after ultrasonic treatment.

1063-7850/03/2905-0392$24.00 © 2003 MAIK "Nauka/Interperiodica"

The results of processing of the curves in Fig. 1 in terms of [6, 7] showed that the decrease in the relaxation rate is related both to a decrease in the surface generation rate S_g and to an increase in the minority carrier generation lifetime τ_g. It should be noted that the MIS structures studied before the ultrasonic treatment exhibited a considerable scatter in the S_g values (from 2.5 to 14.2 cm/s), while the scatter in τ_g did not exceed 20% relative to the mean value $\tau_g = 0.96 \times 10^{-6}$ s. However, the effect of decrease in S_g was observed in all samples, irrespective of the initial values of S_g and τ_g. The ultrasonic treatment not only decreased the surface generation rate S_g but reduced the scatter of these values (S_g = 0.5–2.5 cm/s). The values of τ_g in the region of silicon adjacent to the interface also change upon the ultrasonic treatment, but to a much lower extent: the average value upon the treatment was $\tau_g = 1.6 \times 10^{-6}$ s and the scatter of τ_g values did not exceed 15%.

According to [5, 9] the value of S_g is related to the density of the surface generation centers (surface states). However, the results of our investigation of the capacitance–voltage (C–V) characteristics showed that the ultrasonic treatment does not lead to any significant changes in shape of the C–V curves of the MIS structures (Fig. 2), which is evidence of the absence of changes in the density of surface states (N_{ss}). Moreover, it was established that the difference in the N_{ss} values of the samples before the ultrasonic treatment does not exceed 20% (despite a considerable scatter of the S_g values). We have observed no correlation between the density of surface states and the surface generation rate.

A considerable scatter in the S_g values of the samples with close N_{ss} for the MIS structures prepared in the same technological cycles was also reported previously [10, 11]. It was suggested [12, 13] that this behavior is explained by the fact that S_g depends not only on the density of surface states but on the presence of a local spatial inhomogeneity in the surface charge distribution at the Si–SiO_2 interface and the related fluctuations of the surface potential. In this context, a decrease in S_g upon the ultrasonic treatment can be explained by that this treatment leads to a transformation of the defect structure in the stressed layer at the interface toward leveling of the local inhomogeneities in the surface charge distribution. This results in elimination of the surface generation channels related to the surface potential fluctuations. This explanation is confirmed by the fact that the ultrasonic treatment decreases both S_g and the scatter of these vales. On the other hand, the ultrasound-induced transformation of the defect structure virtually does not change the total number of defects in the transition layer and, hence, does not influence the N_{ss} value.

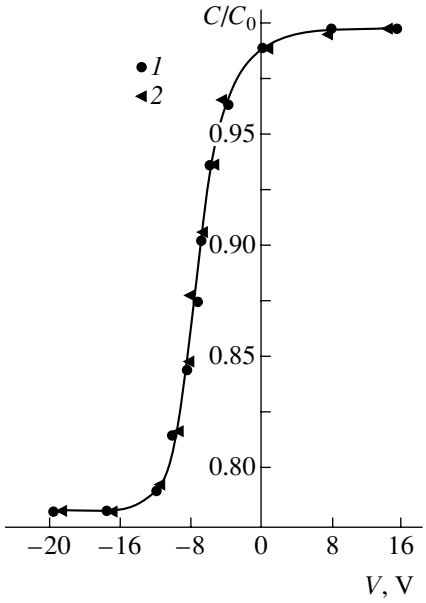

Fig. 2. High-frequency capacitance–voltage characteristics (normalized to the insulator capacitance C_0 = 524 pF) of the MIS structures (*1*) before and (*2*) after ultrasonic treatment.

An increase in the relaxation time τ_g as a result of the ultrasonic treatment of the MIS structures indicates that the region of silicon adjacent to the interface is also subject to a certain transformation of the defect structure, which is accompanied by a decrease in the number of generation centers. However, the ultrasound-induced changes in the generation characteristics are much less pronounced in this region, which can be explained by the absence of a field of internal mechanical stresses facilitating rearrangement of the defect centers.

Thus, the results of our investigations showed that the ultrasonic treatment leads to changes in the generation characteristics of a Si–SiO_2 interface formed upon thermal oxidation of the surface of silicon. These changes are related to the ultrasound-induced transformation of the defect structure at the interface and in the adjacent region of silicon. The presence of internal mechanical stresses is a factor facilitating the transformation of the defect structure. For this reason, the ultrasonic treatment more significantly influences the generation characteristics at the Si– SiO_2 interface than in the bulk of silicon.

REFERENCES

1. P. I. Baranskiĭ, A. E. Belyaev, S. M. Koshirenko, *et al.*, Fiz. Tverd. Tela (Leningrad) **32**, 2159 (1990) [Sov. Phys. Solid State **32**, 1257 (1990)].

2. B. N. Zaveryukhin, V. D. Krevchik, R. A. Muminov, *et al.*, Fiz. Tekh. Poluprovodn. (Leningrad) **20**, 525 (1986) [Sov. Phys. Semicond. **20**, 330 (1986)].

3. E. Yu. Braĭlovskiĭ, A. P. Zdebskiĭ, V. L. Korchnaya, *et al.*, Pis'ma Zh. Tekh. Fiz. **13**, 1310 (1987) [Sov. Tech. Phys. Lett. **13**, 547 (1987)].
4. I. V. Ostrovskiĭ, L. P. Stoblenko, and A. B. Nadtochiĭ, Fiz. Tekh. Poluprovodn. (St. Petersburg) **34**, 257 (2000) [Semiconductors **34**, 251 (2000)].
5. V. S. Pershenkov, V. D. Popov, and V. D. Shal'nov, *Surface Radiation Effects in Integrated Circuits* (Énergoizdat, Moscow, 1988).
6. M. Zerbst, Z. Angew. Phys. **22**, 3039 (1966).
7. J. S. Kang and D. K. Schroder, Phys. Status Solidi A **89** (13), 13 (1985).
8. L. S. Berman and A. A. Lebedev, *Capacitance Spectroscopy of Deep Centers in Semiconductors* (Nauka, Leningrad, 1981).
9. V. G. Litovchenko and A. P. Gorban', *The Principles of Physics of Metal–Dielectric–Semiconductor Microelectronic Systems* (Naukova Dumka, Kiev, 1978).
10. P. K. Schroder and J. Culdberg, Solid-State Electron. **14**, 1285 (1971).
11. P. B. Parchinskiĭ and S. I. Vlasov, Mikroélektronika **30**, 466 (2001).
12. E. I. Gol'dman, Fiz. Tekh. Poluprovodn. (St. Petersburg) **27**, 269 (1993) [Semiconductors **27**, 150 (1993)].
13. E. I. Gol'dman and A. G. Zhdan, Fiz. Tekh. Poluprovodn. (St. Petersburg) **29**, 428 (1995) [Semiconductors **29**, 219 (1995)].

Translated by P. Pozdeev

Technical Physics Letters, Vol. 29, No. 5, 2003, pp. 395–397. Translated from Pis'ma v Zhurnal Tekhnicheskoĭ Fiziki, Vol. 29, No. 9, 2003, pp. 89–94.

Soft X-ray Emission from the Plasma of a Conductor Exploding in a Strong Longitudinal Magnetic Field

Yu. É. Adamian and G. A. Shneerson

St. Petersburg State Technical University, St. Petersburg, Russia

e-mail: integr@delfa.net

Received December 29, 2002

Abstract—Previous experiments with the electric explosion of conductors in a strong (50 T) longitudinal magnetic field showed the formation of a relatively low-density plasma around the central part of the explosion channel, which exhibited expansion at a velocity on the order of 10–20 km/s [1, 2]. Expansion of the plasma was accompanied by displacement of the magnetic field from the explosion channel, which was manifested by a diamagnetic signal. An analysis of the plasma energy balance is hindered by the lack of reliable data about radiative energy losses. Here, we report the first experimental results on the radiation pulse kinetics and the first estimates of the radiation energy. © *2003 MAIK "Nauka/Interperiodica".*

Experimental setup. The experimental setup comprises a massive one-turn solenoid generating a longitudinal magnetic field, powered from a pulsed current generator with a maximum power of 800 kW, an electric explosion unit, and a vacuum chamber placed into a working cavity of the solenoid. The period of the external field variation is 32 μs [1, 2]. The explosion of a conductor takes place at a time in the vicinity of the first maximum of the longitudinal field strength. The electric explosion unit parameters are as follows: capacitance, 4 μF; inductance, 240 nH; charging voltage, 10 kV. Figure 1 shows a schematic diagram of the experimental setup. The radiation is extracted along the axis of the exploded conductor, via special windows in the current feedthrough system. The radiation detectors, representing vacuum diodes with aluminum cathodes, are arranged at the end of an evacuated channel, at a distance of about 0.6 m from the exploding conductor. This distance excludes the action of plasma particles upon the radiation detectors in the course of explosion.

The radiation detectors were calibrated by means of a vacuum electric explosion of a conductor in a capillary. This method of calibration is based on the proximity of the radiative properties of a capillary discharge in the UV and far UV regions to the blackbody characteristics. Since these properties are determined only by the plasma temperature, the main problem in this method is related to determining the plasma temperature in the capillary.

In our experiments, the detectors were calibrated using the radiation generated during electric explosion of a 80-μm-thick copper conductor in a Teflon capillary with an internal diameter of 2 mm. The radiation spectrum exhibits a characteristic maximum at a wavelength of about 1000 Å, which falls within the sensitivity range of the aluminum photocathode. A particular radiation spectrum can be determined from the known plasma temperature. This temperature can be calculated using the experimentally measured conductivity of the channel and well-known relations (Bakulin–Luchinskii conductivity model [3]). The distributions of particle density and conductivity in the capillary cross section are assumed to be homogeneous.

The maximum value of the plasma temperature in a capillary discharge was 4.2 eV. Once the energy distribution of the radiation intensity r_λ is known (Planck formula), the transmission coefficient of the measuring tract can be calculated as

$$K = \frac{2\pi R^2 U}{S\int_0^\infty r_\lambda(\chi_\lambda/\chi_{\max})d\lambda},$$

where U is the voltage at the oscillograph input, S is the radiator area, R is the radiator–photodetector distance, r_λ is the energy distribution of the blackbody radiation intensity, χ_λ is the spectral sensitivity of the photocath-

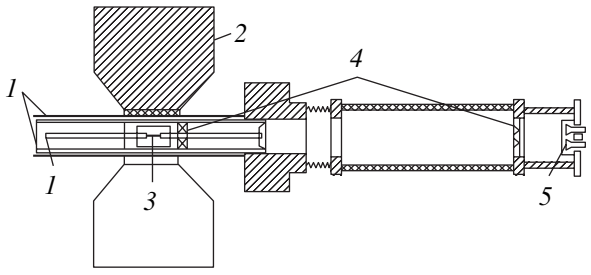

Fig. 1. A schematic diagram of the experimental setup: (*1*) current leads; (*2*) one-turn solenoid; (*3*) conductor; (*4*) diaphragms; (*5*) vacuum diodes (detectors).

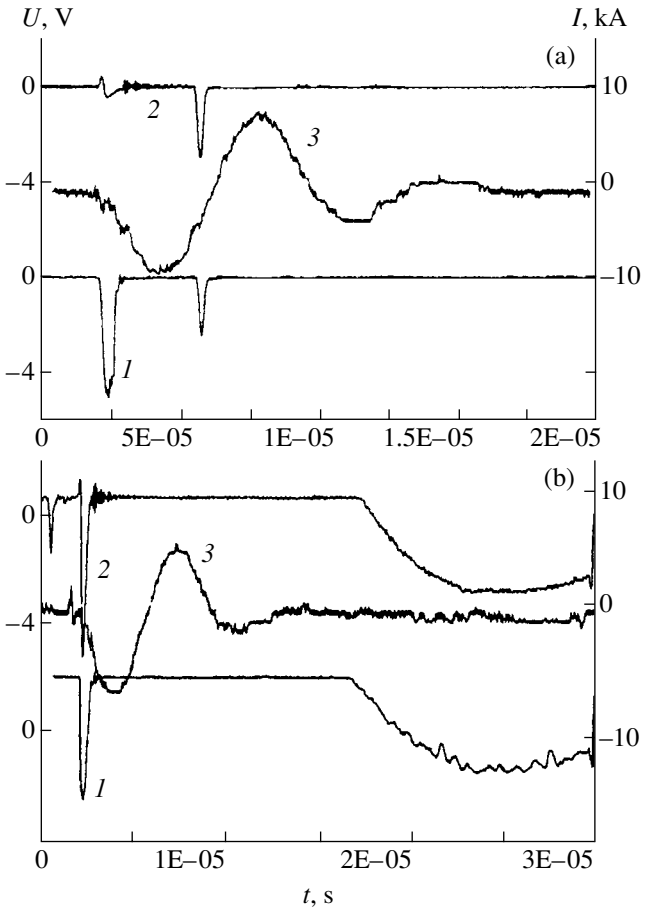

Fig. 2. Typical oscillograms of the current and the signals of radiation detectors during the explosion of an 0.2 mm copper conductor (a) without an applied field and (b) in a longitudinal field of 50 T: (*1*) signal from the detector without filter; (*2*) signal from the detector with a 10-μm-thick Dacron filter; (*3*) current through exploding conductor.

ode at a given wavelength λ, and χ_{max} is the maximum spectral sensitivity [4].

In the stage of calibration, the sensitivity of radiation detectors was adapted to the characteristics of the measuring tract. This was done using slit diaphragms (in experiments with the conductor explosion, the radiation was shielded using additional diaphragms). Thus, using data on the plasma temperature, system geometry, and spectral characteristics of the aluminum cathode, we determined the energy sensitivity of the radiation detection tract, which amounted to 50 and 25 μV m^2/W for channels 1 and 2, respectively.

After calibration, we performed a series of experiments with the conductors exploded with and without applied longitudinal magnetic field. For roughly estimating the total energy emitted during the electric explosion of a conductor with allowance for the spectral distribution, the radiation detector in channel 1 was blocked by a filter with a transmission boundary at 1 keV.

Taking into account that the intensity of radiation from the electric explosion of a conductor is significantly higher than that from the calibration source, the radiation from the exploding conductor was attenuated by a factor of 100 using additional diaphragms placed in the immediate vicinity of the exploding conductor. The radiation from the central region of the exploding conductor was not measured, since the detectors collected radiation only from the spatial region with radius exceeding 4 mm. The sensitivity of the measuring tract in our experiments amounted on the average to 0.5 and 0.25 μV m^2/W for the channels with and without the filter, respectively.

Experimental results. Comparative experiments were performed in the two following regimes.

(A) The electric explosion of a copper conductor without application of external longitudinal magnetic field. Typical oscillograms of the current and the signals from radiation detectors measured in this case are presented in Fig. 2a. As can be seen, the initial stage of explosion is accompanied by longwave emission, while a signal from the detector behind the filter is virtually absent. When the current passes through zero, a shortwave radiation pulse is detected (attenuation in a Dacron filter is insignificant).

(B) The electric explosion of a copper conductor (0.2 mm thick) in a longitudinal magnetic field of 50 T (with a period of 32 μs). The explosion takes place in the vicinity of the maximum field strength. Typical oscillograms of the current and the signals from radiation detectors measured in this case are presented in Fig. 2b. In this case, the initial stage of explosion is accompanied by a shortwave emission from peripheral plasma and, in contrast to regime A, by the absence of any signal from radiation detectors at the moment of the current passage through zero. The appearance of emission in later stages of the process can be related to repeated initiation of the azimuthal discharge upon changing polarity of the external field.

Discussion. During the explosion of a copper conductor with a diameter of 0.2 mm in a longitudinal magnetic field, the radiation detectors showed an intense peak of emission in the shortwave region and a longer stage of emission beginning when the external magnetic field passed through zero. As can be seen from the oscillograms of the radiation detector signals (with allowance for the almost twofold difference in sensitivity between the two channels), the attenuation of radiation by the Dacron filter for the first peak in the initial stage of explosion amounts to 1.5. This corresponds to an average quantum energy of 1.7 keV (or to an average wavelength of 7 Å).

The radiation power incident onto a detector is estimated using the values of sensitivities determined for a capillary discharge, with a correction for a decrease in the sensitivity in the region of quantum energies about 1.7 keV and for the attenuation in slit diaphragms. As a result, the amplitude of the specific power density is

estimated at 6×10^7 W/m^2. For a solid angle of 4π and a radius of 0.6 m (the distance from plasma to detector), the total power radiated from the plasma is $P \sim (2–3) \times 10^8$ W. On the other hand, the maximum power deposited in the conductor, as determined by the current oscillograms and the active voltage component [2], amounts to 5×10^7 W. This large discrepancy between deposited and radiated power values is outside the experimental error limits and may be indicative of a strong spatial anisotropy of the radiation.

Another interesting feature is the appearance of the second, much longer radiation pulse with an effective energy of 1.5 keV, which appears when the external field induction passes through zero. This effect is probably analogous to the theta-pinch, whereby the plasma in the conductor explosion channel is heated as a result of compression in increasing longitudinal magnetic field. The corresponding radiation energy is on the order of 1 keV.

Acknowledgments. This study was supported by the Russian Foundation for Basic Research (project no. 02-02-16157a).

REFERENCES

1. Yu. É. Adamian, S. I. Krivosheev, V. M. Vasilevskiĭ, *et al.*, Pis'ma Zh. Tekh. Fiz. **21** (23), 43 (1995) [Tech. Phys. Lett. **21**, 968 (1995)].
2. Yu. É. Adamian, V. M. Vasilevskiĭ, S. N. Kolgatin, and G. A. Shneerson, Zh. Tekh. Fiz. **69** (5), 121 (1999) [Tech. Phys. **44**, 588 (1999)].
3. Yu. D. Bakulin, V. F. Kuropatenko, and A. V. Luchinskiĭ, Zh. Tekh. Fiz. **46**, 1963 (1976) [Sov. Phys. Tech. Phys. **21**, 1144 (1976)].
4. V. A. Veretennikov, Candidate's Dissertation (Moscow, 1988).

Translated by P. Pozdeev

Technical Physics Letters, Vol. 29, No. 5, 2003, pp. 398–399. Translated from Pis'ma v Zhurnal Tekhnicheskoĭ Fiziki, Vol. 29, No. 10, 2003, pp. 1–5.

The Role of a Vortex Structure in the Mechanism Maintaining Thermal Autooscillations

V. P. Samsonov

Surgut State University, Surgut, Russia

e-mail: svp@iff.surgu.ru

Received December 16, 2002

Abstract—Vortex gas motion accompanying the excitation of thermal autooscillations in a "singing" flame or in a Rijke tube has been studied. A method for measuring the vortex gas flow energy distribution along the resonator tube is proposed. It is established that the vortex motion takes place in the region of a heat source, the size of which does not exceed 3–4 tube diameters. An increase in the resonator tube length increases the relative fraction of the energy of rotational motion in the total mechanical energy of the gas column performing acoustic oscillations. © *2003 MAIK "Nauka/Interperiodica".*

As is known [1], thermal autooscillations of a gas column in a resonant tube, excited due to heat evolution in a so-called "singing" flame or some other thermal source, possess certain general characteristic features. In particular, the amount of thermal power required for the excitation of acoustic oscillations decreases (under otherwise equal conditions) with increasing length of the resonator. Physical models intended to explain this phenomenon are rather contradictory. The mechanisms of feedback between the pressure oscillations and the rate of heat evolution still remain unclear. In the cases of a singing flame and the Rijke tube, these mechanisms are different in view of the unlike dependence of the combustion rate on both pressure and the temperature. The rate of heat evolution from a chemically neutral source, such as an electric spiral, depends only on the rate of convective heat transfer.

Afanas'ev *et al.* [2–4] showed that the excitation of acoustic oscillations is accompanied by the formation of vortex structures near the flame. The knowledge of the distribution of the energy of a gas vortex motion along the resonator tube is necessary for better understanding of the role of the vortex structure in the heat exchange between thermal source and the gas performing acoustic oscillations.

The energy of the gas vortex motion within a limited region of a tube was measured with the aid of a cylindrical sleeve as described previously [5]. The length of the mobile cylindrical sleeve was taken equal to the inner tube diameter (0.085 m), since the results reported in [2–4] indicate that the inner diameter of the tube determines the maximum size of the vortex cell. The sleeve, weighing 24.5 g, was suspended inside the tube on a spring with the coefficient of stiffness $k \leq 0.14$ N/m. The sleeve could move along the entire tube, from bottom to top end. The vertical displacement of the sleeve for each initial position relative to the tube ends was measured twice, at the instant of exciting oscillations (h_1) and at the maximum amplitude of oscillations (h_2). The energy of the rotational motion was determined using the relation $W = k(h_1 - h_2)^2$.

The resonator tube consisted of two parts. The immobile 1.5-m-long part was fixed on a stand. The second, 1-m-long mobile part was put onto the upper half of the first part. The internal diameter of the mobile part exceeded the outer diameter of the immobile part by 2×10^{-3} m. The gap was filled with glycerol in order to prevent the leak of combustion products to the ambient medium and avoid uncontrolled pressure drop inside the tube. By moving the upper end of the mobile part, it was possible to change the total length of the resonator tube and, hence, the period of oscillations in the course of one experiment. The interval of variation of the resonator length was 1.5–2.3 m.

Figure 1 shows the results of measurements of the energy of the rotational motion of a gas in the tube as a function of the current coordinate l of the lower edge of the mobile sleeve (measured from the bottom end of the resonator tube). The measurements were performed for various total lengths of the resonator tube. The heat source was represented by a singing flame. As can be seen from curves *1–3*, the man energy $W(l)$ of the vortex motion is concentrated in the region of the singing flame (heat source). With increasing the distance from the flame, the flow character transforms from vortex to potential under the action of viscous friction forces. A shift of the $W(l)$ maximum is related to the fact that the flame was moved so as to occur in the lower quarter of the resonator tube. Curve *4* shows a change in the kinetic energy $U(l)$ of the translational motion, which exhibits a jumplike increase in the region of the flame and then remains on a certain constant level. The change in $U(l)$ is explained by thermal expansion of the

1063-7850/03/2905-0398$24.00 © 2003 MAIK "Nauka/Interperiodica"

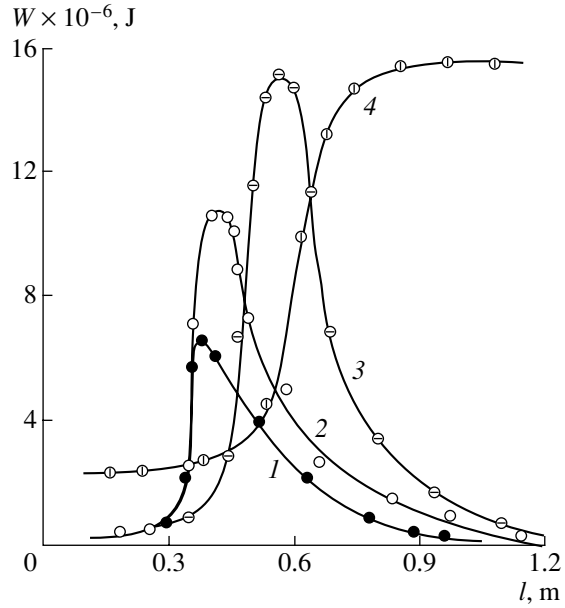

Fig. 1. Kinetic energy distributions for the (*1–3*) rotational and (*4*) translational gas motion in a singing flame along the resonator tubes of various lengths L = 1.5 (*1*), 1.8 (*2*), and 2.3 m (*3*, *4*).

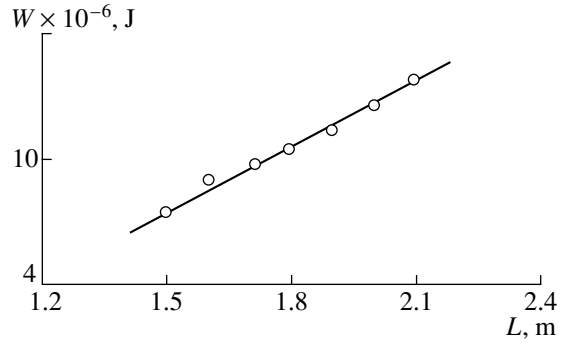

Fig. 2. A plot of variation of the energy W of rotational motion of the gas in a resonator tube with slowly varying length L.

gas and by its acceleration under the action of buoyancy force equilibrated by the viscous friction forces.

By changing position of the mobile part of the resonator tube during the experiment, it is possible to obtain additional information about the ratio of energies of the translational and rotational motions of gas in the tube. As demonstrated in [6], the product of the total mechanical energy E by the oscillation period T in some open mechanical oscillatory systems is an adiabatic invariant, ET = const, with respect to slow variation of the system parameters. On increasing the length of the resonator tube containing an oscillating gas column, we may expect the existence of such adiabatic invariants for the singing flame as well. According to [7], the energy of acoustic oscillations of the gas column in the tube is related to the average velocity of translational motion $\bar{v}_0$ at the tube end by the formula $I = c\rho \int \bar{v}_0^2 \, dS$. Here, I is the sound intensity (equal to the average energy of gas oscillations in the tube per unit time), ρ is the gas density, S is the tube cross section, and c is the sound velocity in the combustion products.

The relative variation of the sound intensity in a tube of slowly increasing length (in the frame related to the tube) can be expressed as $\Delta I/I = -4u/\bar{v}_0$, where u is the rate of tube elongation. If the u value is small compared to $\bar{v}_0$, a relative change in the period of oscillations can be written as $\Delta T/T = 4Tu/v_0$. Comparing these expressions, we obtain IT = const. This relation implies that the intensity of acoustic oscillations decreases with increasing length of the tube, since the oscillation period grows. The discrepancy with the well-known fact that the acoustic oscillations are more readily excited with increasing amplitude in a longer tube (at the same thermal power) can be explained by the increasing fraction of the energy of rotational motion in the total mechanical energy of the gas.

In order to verify the latter assumption, we have experimentally measured the energy of rotational motion in the course of outward motion of the mobile part of the resonator tube at a velocity of ≈0.01 m/s. The velocity of translational motion of the combustion products was ≈0.2 m/s, and the period of oscillations changed from 4×10^{-3} to 6.8×10^{-3} s. The position of the mobile sleeve relative to the flame remained unchanged. Figure 2 shows the $W(L)$ curve measured under these conditions, where L is the current length of the resonator tube. As can be seen from this plot, the energy of the rotational motion linearly increases with L in the whole interval of resonator lengths studied. The results presented in Figs. 1 and 2 are qualitatively consistent with the data obtained for the Rijke tube. This coincidence indicates that the feedback mechanisms accounting for realization of the Rayleigh principle for the excitation of thermal autooscillations are related to the vortex structure formation in a gas flow.

REFERENCES

1. *Nonsteady Flame Propagation*, Ed. by J. G. Markstein *et al.* (Pergamon, Oxford, 1964; Mir, Moscow, 1968).
2. V. V. Afanas'ev, S. A. Abrukov, N. I. Kidin, *et al.*, Fiz. Goreniya Vzryva **31** (4), 34 (1995).
3. V. V. Afanas'ev, Fiz. Goreniya Vzryva **35** (4), 43 (1999).
4. S. V. Ilyin, D. C. Alexandrov, and V. V. Afanasyev, *CD-ROM Proc. of VSJ-SPIE98 Intern. Conf. on Optical Technologies and Image Processing in Fluid, Thermal and Combustion Flow, Jokohama, Japan, 1998*, AB074.
5. V. P. Samsonov, Pis'ma Zh. Tekh. Fiz. **29** (2), 1 (2003) [Tech. Phys. Lett. **29**, 41 (2003)].
6. L. D. Landau and E. M. Lifshitz, *Mechanics* (Nauka, Moscow, 2001; Pergamon Press, Oxford, 1976).
7. L. D. Landau and E. M. Lifshitz, *Fluid Mechanics* (Nauka, Moscow, 1986; Pergamon Press, Oxford, 1987).

Translated by P. Pozdeev

Technical Physics Letters, Vol. 29, No. 5, 2003, pp. 400–403. Translated from Pis'ma v Zhurnal Tekhnicheskoĭ Fiziki, Vol. 29, No. 10, 2003, pp. 6–14.

Bulk Large-Area GaN Layers

Yu. V. Zhilyaev, A. V. Nasonov, S. D. Raevskiĭ, S. N. Rodin, M. P. Shcheglov, Sh. A. Yusupova, and V. Yu. Davydov

Ioffe Physicotechnical Institute, Russian Academy of Sciences, St. Petersburg, 194021 Russia

e-mail: Zhilyaev@jyuv.ioffe.rssi.ru

Received January 21, 2003

Abstract—Mirror-smooth, transparent bulk GaN layers with an area of 2×3 cm^2 and a thickness of up to 1 mm were grown by hydrochloride vapor-phase epitaxy. Cracking of the material was eliminated by using a two-stage growth process; separation from a substrate was provided by a low-temperature buffer layer of preset thickness. For the best samples, FWHM of the X-ray rocking curve was $\omega_\theta = 3.5'$ and the dislocation density amounted to 10^7–10^8 cm^{-2}. © *2003 MAIK "Nauka/Interperiodica".*

Introduction. Recent years were marked by considerable achievements in the design and production of nitride based devices, including ultrabright blue and green LEDs [1], violet lasers based on InGaN/GaN/AlGaN heterostructures [2], and a number of devices characterized by stable operation at elevated temperatures [3]. The main problem hindering the further development of GaN based devices is the lack of proper substrates. The use of sapphire (Al_2O_3), characterized by a considerable mismatch relative to GaN (both in the crystal lattice parameters and in thermal expansion coefficients), leads to a high dislocation density in device structures and their rapid degradation.

The best solution would be provided by using intrinsic GaN substrates. A certain success in the synthesis of bulk GaN crystals at high pressures and temperatures has been achieved [4], but the high cost and small dimensions of these crystals hinder their use as substrates for electronic devices. At present, it is a common practice to grow thick epitaxial GaN layers using lateral growth technology [5, 6]. Bulk GaN layers are then obtained by various methods, including removal of the sapphire substrate by grinding [7] or ion etching of SiC substrates [8]. According to a softer technology, separation of a thick epitaxial GaN layer grown by hydrochloride vapor-phase epitaxy (HVPE) is provided by a laser beam scanning over the rear surface of a sapphire substrate and decomposing the GaN layer adjacent to the substrate [9].

Previously [10], we reported on the development of an HVPE technology, which allowed bulk GaN layers to be obtained without any special separation procedure. According to this technology, epitaxial GaN plates are readily separated due to preliminary deposition of a low-temperature buffer layer of preset thickness. However, the bulk GaN layers grown at ~910°C as described in [10, 11] were nontransparent, and the samples did not possess the desired smooth surface morphology.

Below, we report on the improvement of the growth technology, which ensures the obtaining of transparent, mirror-smooth bulk GaN layers of a large area and high quality (Fig. 1).

Experimental. The heteroepitaxial GaN layers were grown on (0001) sapphire substrates by HVPE in a horizontal quartz reactor with an internal diameter of 40 mm. The process was conducted in a flow of Ar. The source of Ga was GaCl synthesized immediately in the reactor by passing gaseous HCl over a boat with melted Ga, while the source of nitrogen was gaseous ammonia delivered immediately to the growth zone.

Bulk GaN layers were grown according to a standard technology involving preliminary deposition of a low-temperature buffer layer (T_1 = 500–530°C). However, the thickness of this layer was selected so as to ensure separation of the as-grown main layer in the

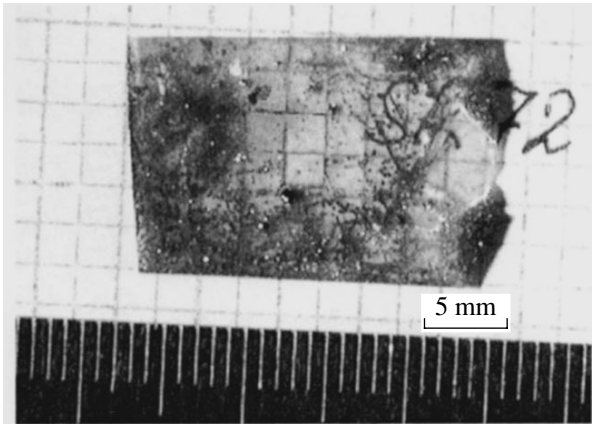

Fig. 1. Bulk GaN plate grown by a two-stage process (variant 1).

1063-7850/03/2905-0400$24.00 © 2003 MAIK "Nauka/Interperiodica"

course of cooling. The main GaN layer was grown at T_2 = 1030–1075°C. The bulk layers obtained by this method appeared as mirror-smooth plates, but the samples exhibited cracking into pieces with maximum dimensions of about 7 × 7 mm (Fig. 2).

In order to avoid cracking, the main layer was grown using a two-stage process implemented in two variants. According to the first variant, deposition of the buffer layer was followed by growing the first main GaN layer in that part of the growth zone which was characterized by a relatively small growth rate but ensured the obtaining of bulk GaN layers of the best quality. Then the growth was suspended and the samples were transferred to the zone characterized by a higher deposition rate, where the process was continued until completion of the second layer. Simultaneously, the samples were rotated through 180° in the horizontal plane in order to obtain layers of homogeneous thickness. Using this variant, we succeeded in obtaining bulk GaN plates with dimensions up to 2 × 3 cm (Fig. 1) with a quality comparable with that of the layers grown in a single-stage process. Separate black points observed on the photograph are caused by polycrystalline GaN particles falling onto the sample surface from some reactor parts during the substrate transfer.

The two-stage growth according to the second variant was conducted as follows. Deposition of the buffer layer was followed by growing the first main GaN layer under the optimum conditions ensuring the growth of bulk GaN layers of the best quality. When the first layer became sufficiently thick, the HCl flow rate was increased without interrupting the growth process. The increase in the HCl flow rate in the second stage led to the corresponding increase in the GaN deposition rate. Upon accomplishing the growth stage, the plates were cooled and separated from substrates without cracking, reaching up to 2 × 2 cm in size, while Al_2O_3 substrates exhibited cracking. In this case, no GaN particles (appearing black points on the photographs) are found on the sample surface. The quality of bulk GaN layers grown in this way exhibited no evidence of deterioration, which suggests that the growth mechanism and the perfect structure established in the first stage are inherited by epitaxial layers grown in the second stage. The growth in the second stage proceeds under conditions different from optimum, but on a GaN (rather than sapphire) surface. Figure 3b shows the cross-section of a sample grown by this variant. As can be seen, there is no distinct boundary separating layers grown in different stages.

Results and discussion. The structural perfection of GaN samples was evaluated by measuring the full width at half maximum (FWHM) of the X-ray rocking curves. For the best deposits, this parameter was ω_θ = 3.5′. The Hall measurements showed a charge carrier density of $n = 10^{18}$–10^{20} cm^{-3} and the carrier mobility reaching up to μ = 100 cm^2/(V s).

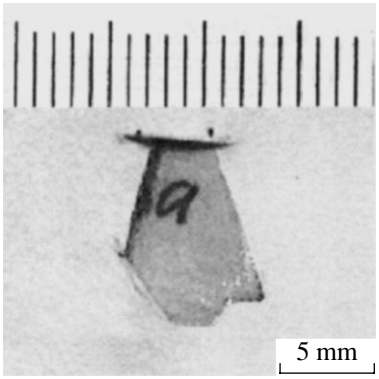

Fig. 2. Bulk GaN fragment obtained by a conventional method.

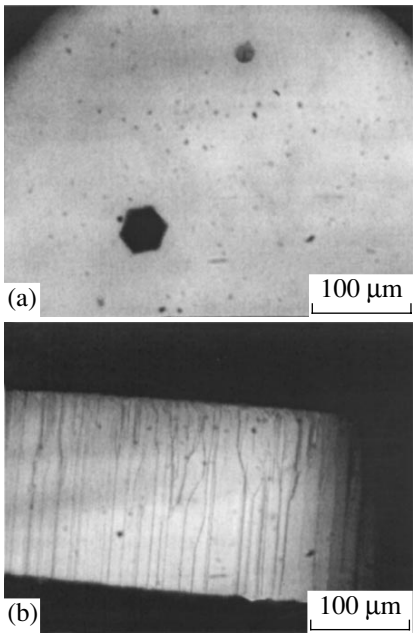

Fig. 3. Micrographs of the (a) surface and (b) cross-section of a bulk GaN plate grown by a two-stage process (variant 2).

Additional characterization of the structural perfection was provided by Raman scattering. The Raman spectra were measured at room temperature in the backscattering geometry (with the *z* axis parallel to the optical axis of GaN crystals). The spectra were excited by an Ar^+ laser operating at a wavelength of λ = 488 nm. The scattered light was analyzed by a double grating monochromator with a spectral slit width of 1 cm^{-1}. Figure 4 presents typical Raman spectra of GaN layers grown on Al_2O_3 substrates. The spectra of most samples display peaks corresponding to phonons of the E_2 (high) and A_1 (LO) symmetry and to a low-frequency phonon–plasmon mode (PPM). The presence of a spectral line corresponding to an unscreened phonon of the A_1 (LO) symmetry shows evidence of the presence

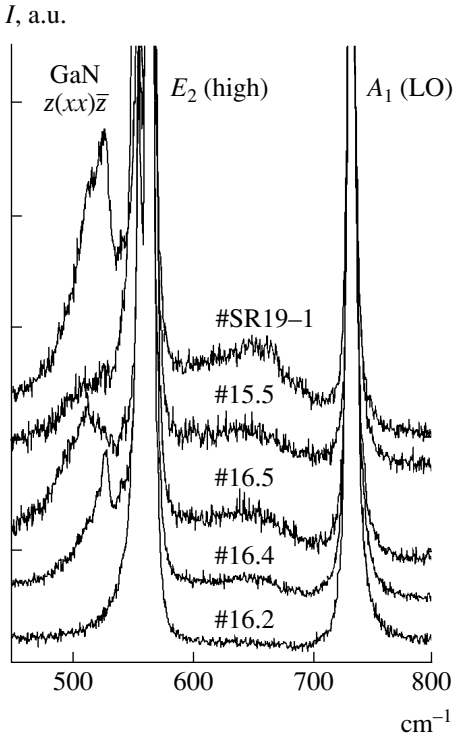

Fig. 4. Room temperature Raman spectra of GaN layers measured in the $z(xx)\bar{z}$ backscattering geometry (normalized to the E_2 (high) phonon line intensity).

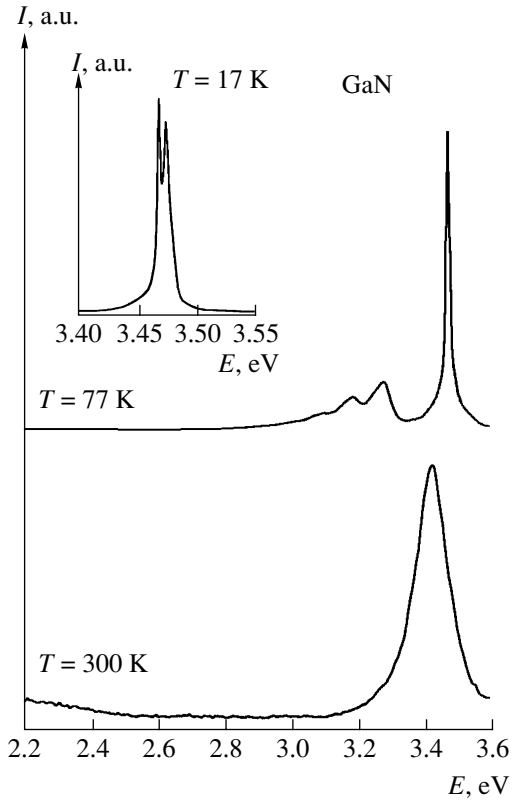

Fig. 5. Photoluminescence spectra of GaN layers measured at various temperatures.

of regions with a small density of free charge carriers ($n \sim 5 \times 10^{16}$ cm^{-3}), while a decrease in the lower PPM frequency reflects the presence of regions with a high charge carrier density ($n > 10^{19}$ cm^{-3}). One possible reason for the inhomogeneous distribution of charge carriers in the samples studied is the presence of regions with a highly density of defects, which is manifested by a broad spectral band with a maximum at ~650 cm^{-1} (Fig. 4).

Note that the Raman spectrum of sample 16.2 contains only two spectral lines corresponding to phonons of the E_2 (high) and A_1 (LO) symmetry allowed by the selection rules for GaN samples with homogeneous charge carrier distribution. The absence of a band at 650 cm^{-1} is indicative of a higher structural perfection of this sample. A small halfwidth (FWHM ~ 3 cm^{-1}) of the line due to a nonpolar phonon with the E_2 (high) symmetry is additional evidence of the perfect structure.

Deformation of the epitaxial GaN layers leads to a shift of the phonon lines relative to their positions in the spectrum of an unstrained bulk GaN sample. An analysis of the Raman spectra showed that all GaN layers grown on Al_2O_3 substrates possess residual deformation. The amount of compressive stresses in the plane of a GaN layer grown on Al_2O_3, as estimated from the shift of the E_2 (high) mode, reaches 0.1–0.2 GPa (sample 15) [12]. However, such stresses are virtually absent in the samples of GaN separated from substrates. A comparative analysis of the Raman spectra measured on both the free GaN surface and on the surface contacting with the substrate confirmed that the obtained epitaxial GaN layers are structurally homogeneous across their thickness.

A study of the surface morphology of the GaN plates showed that the front face of samples represents a smooth and sufficiently homogeneous surface with separate defects in the form of hexagonal pits (Figs. 3a, 3b).

The samples were also characterized by photoluminescence (PL) spectra measured in the reflection mode at various temperatures (300, 77, and 17 K). The PL response was intense and homogeneously distributed over the sample surface. The main room temperature PL from GaN/Al_2O_3 samples is observed at 3.43 eV (Fig. 5). A 40-meV shift relative to the normal position (3.39 eV) is indicative of a stressed state of the GaN layer. The main PL peak of GaN separated from the sapphire substrate corresponds to 3.40–3.41 eV, which is evidence of a significant reduction in the level of stresses. The PL spectra measured at liquid nitrogen temperature (77 K) revealed splitting of the main peak (band–band transitions) into components corresponding to bound and free excitons, which confirmed the high quality of the samples. This PL spectrum also exhibits a band due to the donor–acceptor recombination, which shows evidence of a small amount of foreign impurities at a high quality (significantly narrower main peak) of the base material (Fig. 5). The low-tem-

perature PL spectrum measured at 17 K displayed clearly resolved components of the edge emission peak (Fig. 5), related to the free and bound excitons.

Conclusion. The proposed two-stage HVPE growth procedure allows high-quality bulk GaN layers to be obtained with dimensions of up to 2×3 cm and prevents cracking of the plates. The plates of GaN are transparent, exhibit mirror-smooth surface morphology, and possess the following characteristics: X-ray rocking curve width (FWHM), $\omega_\theta = 3.5'$; dislocation density, 10^7–10^8 cm^{-2}; charge carrier density, $n = 10^{18}$–10^{20} cm^{-3}; carrier mobility, $\mu = 100$ cm^2/(V s).

Acknowledgments. This study was supported by the Russian Foundation for Basic Research, project nos. 00-02-16989 and 99-02-18318.

REFERENCES

1. S. Nakamura, M. Senoh, N. Iwasa, *et al.*, Jpn. J. Appl. Phys. **34**, L1332 (1995).
2. S. Nakamura, M. Senoh, N. Iwasa, *et al.*, Jpn. J. Appl. Phys. **35**, L74 (1996).
3. S. Yoshida and J. Suzuki, Jpn. J. Appl. Phys. **37**, L482 (1998).
4. I. Grzegory, M. Bockowski, B. Lucznik, *et al.*, MRS Internet J. Nitride Semicond. Res. **1**, 20 (1996).
5. A. Usui, H. Sunakawa, A. Sakai, and A. Yamaguchi, Jpn. J. Appl. Phys. **36**, L899 (1997).
6. H. Sone, S. Nambu, Y. Kawaguchi, *et al.*, Jpn. J. Appl. Phys. **38**, L356 (1999).
7. S. Nakamura, M. Senoh, S. Nagahama, *et al.*, Appl. Phys. Lett. **72**, L2014 (1998).
8. Yu. V. Melnik, K. V. Vassilevski, I. P. Nikitina, *et al.*, MRS Internet J. Nitride Semicond. Res. **2**, 39 (1997).
9. M. K. Kelly, R. P. Vaudo, V. M. Phanse, *et al.*, Jpn. J. Appl. Phys. **38**, L217 (1999).
10. V. V. Bel'kov, V. M. Botnaryuk, L. M. Fedorov, *et al.*, MRS Symp. Proc. III–V Nitrides. **449**, L343 (1997).
11. V. V. Bel'kov, V. M. Botnaryuk, L. M. Fedorov, *et al.*, J. Cryst. Growth **187**, 29 (1998).
12. V. Yu. Davydov, N. S. Averkiev, I. N. Goncharuk, *et al.*, J. Appl. Phys. **82**, 5097 (1997).

Translated by P. Pozdeev

Technical Physics Letters, Vol. 29, No. 5, 2003, pp. 404–407. Translated from Pis'ma v Zhurnal Tekhnicheskoĭ Fiziki, Vol. 29, No. 10, 2003, pp. 15–22.

The Effect of Compensation Currents of the Open Discharge

A. R. Sorokin

Institute of Semiconductor Physics, Siberian Division, Russian Academy of Sciences, 630090 Novosibirsk, Russia

e-mail: IFP@isp.nsc.ru

Received December 6, 2002

Abstract—Previous conclusions concerning a general mechanism of electron beam formation in glow discharges of various types, including the open discharge, are confirmed. The discharge behavior is determined by ionization processes and by the bombardment of cathode with fast heavy particles, in agreement with well-established notions about the glow discharge. Neither compensation currents nor the electron beam current can account for the photoelectron mechanism of the open discharge, despite still existing opposite assumptions. © *2003 MAIK "Nauka/Interperiodica".*

1. Recently, Kolbychev [1] revised the mechanism of photoemission from the cathode in an open discharge. Pointing out the short duration of the stage of pulsed electron beam formation, deterioration of the geometry of cathode illumination with increasing applied voltage, and reduction in the energy deposition contribution due to the UV radiation (whereby electrons of the beam less effectively interact with the gas), he concluded [1] that the UV radiation accounting for the photoelectron character of the open discharge is emitted from atoms excited by the current j_g to the anode grid, compensating for the charge carried away by the electron beam to the drift space, rather than by the electron beam as such. While the first part of this statement fully agrees with the concept repeatedly formulated in my previous papers [2, 3], it is by no means possible to accept the conclusion as well. Indeed, questions naturally arise as to why the open discharge current remains unchanged when the drift length changes, for example, by an order of magnitude and how we can interpret a quasistationary or continuous open discharge when $j_g = 0$. Although these discrepancies were recently emphasized again [4], Kolbychev [5] repeated the conclusion formulated in [1]. Finally, it should be noted that the open discharge was specially developed for the excitation of lasers; however, according to [1], compensation currents of the usual discharge type excite atoms even better than do electron beams. Then, it would be natural to reject electron beams and excite lasers by means of the usual discharge.

Despite these obvious inconsistencies, let us consider the compensation currents in more detail. The experiments described below will reveal the influence of electron beams on the open discharge, which is generally important for finally elucidating the open discharge mechanism.

2. The role of the compensation current j_g in the anode grid can be clearly and simple elucidated by comparing the behavior of the total open-discharge current in the cases when the collector is connected to the anode (j_c) and when it is disconnected (j_{dc}); in the latter case, the collector is under a free potential, whereby the total electron beam current becomes the compensation current ($j_g = j_{dc}$) and the j_g value increases by orders of magnitude.

The open discharge was initiated between a duralumin cathode and molybdenum anode (representing a grid of 1 mm mesh, with a geometric transparency of $\mu = 0.85$) separated by a gap of width $d = 0.65$ mm. The collector was arranged at a distance of $L = 19.5$ mm from the grid. In the disconnected collector mode, the collector potential U_p relative to anode was measured via a high-ohmic resistance R.

In all experiments, disconnecting the collector (whereby j_g and its contribution to the photoeffect were at maximum) led to an increase in the delay t_d of the electric breakdown of the gap d, up to tens of nanoseconds or above, until the breakdown ceased. The effect of processes in the drift space upon the open discharge is readily traced with increasing the voltage U applied to the gap d at low pressures p.

At small applied voltages, neither the discharge current nor the potential U_p (for $R = 50$ kΩ) can be detected by the measuring system. As the applied voltage U is increased, the pre-breakdown beam current delivers (with disconnected collector) a significant negative potential to the collector, initially with a delay of ~10 μs and then with a smaller delay. Under these conditions, j_{dc} is not detected, but j_c is measured as soon as the collector is connected (Fig. 1a). The absence of j_{dc} is related to the partial compensation of the field, sag-

1063-7850/03/2905-0404$24.00 © 2003 MAIK "Nauka/Interperiodica"

ging from the gap d beyond the grid, by the field of a negative charge accumulated on the collector. This decreases ionization in the holes of the anode grid, reduces the ion flux from the holes to cathode, and hinders the initiation of discharge. As the applied voltage increases further, the first electric breakdown of the gap L between collector and anode takes place on the trailing front of the potential U_p (initially with the delay of a few microseconds and then with a smaller delay). As a result, an electron beam is formed (opposite to the main beam) that produces ionization of the gas in the anode grid holes, thus leading to an increase in the ion flux to the cathode. The moment of breakdown in the gap L is clearly correlated with the appearance of j_{dc}, which is delayed relative to j_c and rapidly grows (to exceed j_c) with increasing U (Fig. 1b).

At still higher applied voltages, the current j_{dc} and, hence, the electron beam current increase so rapidly after the first breakdown of the gap L that the potential U_p starts increasing again to induce a second (heavy-current) breakdown of the gap L (Fig. 1c). Although the current amplitude $j_{dc} = 3.2$ A/cm^2 is eight times the j_c value ($K = j_{dc}/j_c = 8$), the onset of j_{dc} is delayed by $t_d >$ 100 ns relative to j_c. If the growth of U is continued, the coefficient K passes through a maximum and starts to decrease tending to unity.

It is important to note that, at not very high U (whereby $K < 1$), disconnecting the collector leads to a manifold growth in the intensity of emission from gas in the drift space. This is accompanied by a drop in the discharge current, thus evidencing the insignificant role of the photoemission from cathode related both to the compensation currents and the electron beam (the opposite electron beam produces additional excitation of atoms).

The results of experiments showed that the discharge is significantly influenced by the magnitude of the high-ohmic divider arm R. At low pressures, disconnection of R completely hindered the possibility of measuring j_{dc} because of large fluctuations in the delay time t_d. The fluctuations of t_d significantly decreased even for $R = 530$ kΩ. This result suggests that the initial stage of discharge is significantly affected by processes in the drift space, controlling the ion flux to cathode.

With increasing pressure, the currents j_{dc} and j_c exhibit leveling ($K \longrightarrow 1$), while the delay vanishes ($t_d \longrightarrow 0$). Acceleration of the discharge development was accompanied by an increase in the level of parasitic signals induced in the measuring chains, which complicated the detection of small (albeit also increased) pre-breakdown currents and the measurement of potential U_p via large resistance ($R = 50$ kΩ). For these reasons, and because the moment of breakdown in the gap L shifted toward the front of the U pulse, it was difficult to judge from the oscillograms of j_{dc} and j_c which of the two currents appeared first. However, when the sink of electrons from the collector was increased by decreasing R, the delay t_d became clearly pronounced: $R =$ 2 kΩ, $K = 1.5$, $j_c = 9.5$ A/cm^2 (Fig. 1d). Upon disconnecting R, the ratio of currents becomes equal to $K = 2$; under these conditions, it was possible (as above) to obtain $K < 1$ by decreasing the applied voltage.

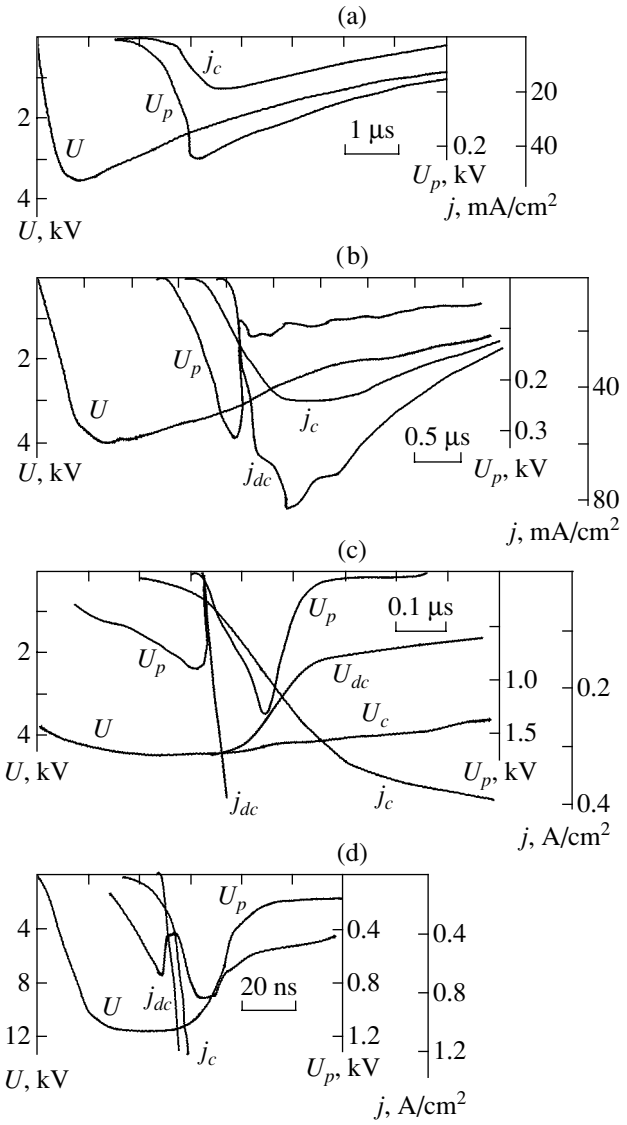

Fig. 1. Open discharge: the oscillograms of voltage U across the cathode–anode gap, collector potential U_p, and the currents and voltages j_{dc}, U_{dc} (with disconnected collector) and j_c, U_c (with the collector connected to anode) measured at a helium pressure of (a–c) 1.5 Torr and (d) 5.8 Torr.

At still higher pressures, the two breakdown pulses merged into one and, beginning with $p >$ 10 Torr, the currents became almost equal ($K = 1$, $t_d = 0$) even with disconnected R. For example, at $p = 13$ Torr and $U >$ 4 kV, the current j_{dc} exceeded j_c only by ≈1% (this difference can be considered as the upper limit of the photoemission contribution due to the compensation current). Under these conditions, rapidly formed and suffi-

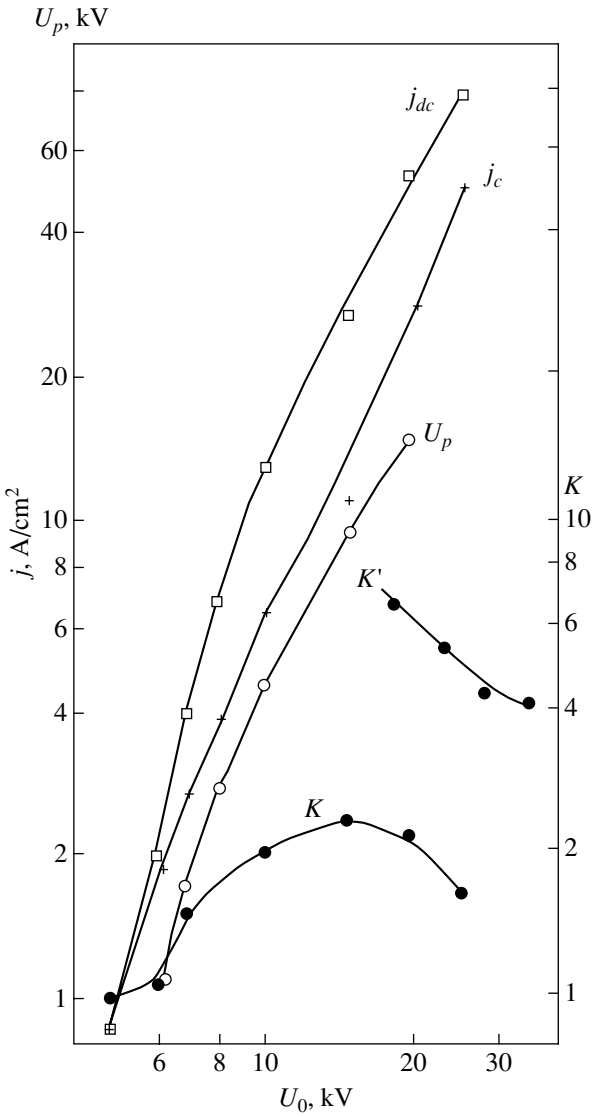

Fig. 2. Plots of the j_{dc} and j_c currents, collector potential U_0, and the coefficient $K = j_{dc}/j_c$ versus the amplitude of the cathode–anode voltage U_0 for the hollow-anode discharge in He + 1% O_2 mixture at a pressure of p = 3.4 Torr (K', at p = 0.4 Torr).

ciently dense anode plasma in the gap d is capable of controlling the discharge parameters, while reduced field strength in the plasma favors ionization [6]. For the same reason, the formation of a cathode potential fall and the appearance of anode plasma behind this region (beginning with sufficiently high voltage U) led to a decrease in the K value.

Thus, neither the compensation currents nor the electron beam currents can account for the photoelectron mechanism of the open discharge. All processes are determined by the ionization and the atom–atom electron emission from the cathode, as is commonly accepted for the glow discharge [6].

3. In order to emphasize the identical character of processes in the glow discharges of various types, the role of compensation currents was studied using a setup described in [7, Fig. 4]. This system comprises a 5-mm-thick ring anode with a 20-mm round hole, spaced by 5 mm from a duralumin cathode (cathode–anode distance, 40 mm). The hole could be covered with a grid, which transformed the discharge with hollow cathode to an open discharge with a large interelectrode gap (d = 10 mm). The discharge was initiated in helium (for increased stability, 1% O_2 could be added [6]).

In all cases, the pattern of variation of j_{dc}, j_c, and U_p was qualitatively the same as that presented above in Section 2. There were some distinctions (rather insignificant, being related primarily to a greater freedom in the development of ionization processes in the main discharge gap): (i) greater values of currents; (ii) one-pulse breakdown between grid and collector; (iii) pressure dependences of the parameters shifted toward lower pressures. Even for the normal glow discharge, the length of the cathode potential fall region (l_{cf} = $1.3p^{-1}$ cm) became smaller than d = 10 mm, beginning at $p > 1.3$ Torr. In the absence of the grid, the volume processes could develop even more freely. In both cases, neither open discharge nor a discharge with hollow cathode were realized: the gap featured usual anomalous discharge.

Figure 2 shows an example of the discharge with hollow cathode for p = 3.4 and 0.4 Torr (R = 50 kΩ). At higher pressures (see above) K approached unity beginning with $p \sim 10$ Torr. Note that, as was demonstrated in [7], electron beams were effectively generated under all studied conditions.

4. Finally, let us discuss one remark in [1], in which attention is given to the short duration of the effective stage of electron beam generation as compared to the total discharge duration. As stated in [1], this is related to the short duration of the UV illumination (restricted to the stage of charge neutralization by the compensation current in the drift space). However, this assumption is inconsistent with the fact of the existence of effective electron beams, for example, in a continuous open discharge.

In fact, the observed rapid drop in the efficiency η during termination of the discharge pulse is related to the process of charge transfer in the gap d. The efficiency of the electron beam formation in the open discharge is defined as the ratio of the collector current to the total discharge current: $\eta = j_e/j$. This characteristic depends in the coefficient γ of the electron emission from the cathode and on the fraction k of electrons generated in the volume of the discharge gap and reaching the collector: $\eta \approx \mu(\gamma + k)(\gamma + 1)^{-1}$ [8]. In the typical open discharge [5, 8], the electron runaway conditions are valid in the whole discharge gap. For this reason, $k \approx 1$, η is independent of γ, and $\eta \approx \mu$ (geometric transparency of the grid). The above formula for η is valid when the number of positive ions arrived at the cathode from the gap d, together with the positive charges appearing upon the removal of electrons via γ pro-

cesses, is equal to the total number of electrons striking the anode and collector. This regime is realized in a stationary or quasistationary discharge, at a time close to the maximum pulsed discharge current during the transition from accumulation to dissipation of the positive charge in the gap. In the latter stage, the ion flux (uncompensated by electrons) additionally contributes only to the anode current and, hence, $\eta < \mu$.

Thus, a decrease in η on the trailing edge of the open discharge current is related to the ion flux to cathode dominating over the electron flux to anode and collector.

Conclusions. (1) In all cases considered above, the experimental data confirm the conclusion [3, 7, 8] concerning a general mechanism of the electron beam formation in glow discharges of various types, including the open discharge. The discharge behavior is determined by ionization processes and by the bombardment of a cathode with fast heavy particles. Neither compensation currents nor the electron beam current can account for the photoelectron mechanism of the open discharge, in contrast to the assumptions made in [1, 9].

(2) At low pressures ($p < 10$ Torr), it is possible to control the discharge current within one order of magnitude at a fixed applied voltage U, by selecting a coupling resistance (R) between anode and collector. The opposite electron beam formed under these conditions produces additional excitation of the gas, which is important for discharge applications in lasers.

REFERENCES

1. G. V. Kolbychev, Izv. Vyssh. Ucheb. Zaved., Fiz., No. 11, 84 (1999).
2. A. R. Sorokin, Pis'ma Zh. Tekh. Fiz. **21** (20), 37 (1995) [Tech. Phys. Lett. **21**, 832 (1995)].
3. A. R. Sorokin, Pis'ma Zh. Tekh. Fiz. **28** (9), 14 (2002) [Tech. Phys. Lett. **28**, 361 (2002)].
4. A. R. Sorokin, Pis'ma Zh. Tekh. Fiz. **26** (24), 89 (2000) [Tech. Phys. Lett. **26**, 1114 (2000)].
5. G. V. Kolbychev, Opt. Atmos. Okeana **14** (11), 1056 (2001).
6. M. A. Zav'yalov, Yu. E. Kreĭndel', *et al.*, *Plasma Processes in Technological Electron Guns* (Énergoatomizdat, Moscow, 1989).
7. A. R. Sorokin, Opt. Atmos. Okeana **14** (11), 1062 (2001).
8. A. R. Sorokin, Pis'ma Zh. Tekh. Fiz. **29** (4), 86 (2003) [Tech. Phys. Lett. **29**, 171 (2003)].
9. A. P. Bokhan and P. A. Bokhan, Opt. Atmos. Okeana **15** (3), 216 (2002).

Translated by P. Pozdeev

Technical Physics Letters, Vol. 29, No. 5, 2003, pp. 408–410. Translated from Pis'ma v Zhurnal Tekhnicheskoĭ Fiziki, Vol. 29, No. 10, 2003, pp. 23–28.

Study of the Dynamics of Optical Emission from the Plasma Formed during Laser Ablation of a Polycrystalline $CuInS_2$ Target

A. K. Shuaibov, M. P. Chuchman, and A. I. Dashchenko

Uzhgorod National University, Uzhgorod, Ukraine

Received November 22, 2002

Abstract—We have studied the temporal characteristics of emission from the plasma formed during laser ablation of a polycrystalline $CuInS_2$ target. The plasma was generated by a focused beam of a pulsed-periodic laser operating at a wavelength of $\lambda = 1.06$ μm and a power density of $W \le 5 \times 10^8$ W/cm^2. The oscillograms of emission from the products of $CuInS_2$ decomposition occurring at various distances from the target were measured, from which the recombination times of a multicomponent laser plasma were determined. The results can be used for optimization of the process of laser deposition of thin films for solar cell elements. © *2003 MAIK "Nauka/Interperiodica".*

A polycrystalline compound with the composition $CuInS_2$ is among the most promising materials for thin-film elements of solar cells manufactured using laser beam deposition technology [1, 2]. For the optimization of this process, it is important to know the mechanism of laser ablation of the target and the main parameters of the resulting multicomponent plasma. In addition to using mass spectrometry techniques for the laser plasma diagnostics [3], a promising approach is offered by methods of optical diagnostics at high temporal and spatial resolution [4]. The first quantitative data on the emission from laser plasmas of copper and indium, representing individual components of $CuInS_2$, were reported in [5, 6]. The conditions of laser ablation for the polycrystalline compound were close to those for the pure metal targets. This circumstance allows us to perform a comparative analysis of emission from the laser plasmas of metals and polycrystalline compounds of the type of $CuInS_2$ or $CuInSe_2$.

Here, we report the results of investigation of the temporal characteristics of emission from a multicomponent plasma formed during moderate-power laser ablation of a $CuInS_2$ target in vacuum.

The experiments were performed with a polycrystalline $CuInS_2$ target (with an impurity content not exceeding 10^{-5}) in the form of a disk placed into a metal vacuum chamber evacuated to a residual pressure of ≤7 Pa. The optical emission from the laser plasma was collected with the aid of a lens from two regions on the axis of a laser plasma torch, spaced by $d = 1$ and 7 mm from the target surface. The experimental setup and procedure were described in detail elsewhere [7, 8].

An analysis of the emission from the plasma formed during laser ablation of the polycrystalline $CuInS_2$ target (see table) showed that the spectrum is determined primarily by the emission from copper and indium atoms. At the same time, the emission spectrum of the multicomponent plasma contained no spectral lines of

Intensity distribution in the spectrum of emission from plasma at a laser-ablated polycrystalline $CuInS_2$ target

λ, nm (atom, ion)	Upper state	*J*, a.u.
550.7 SI	$8d^5D^0$	0.05
522.0 CuI	$4d^2D_{3/2}$	0.55
521.8 CuI	$4d^2D_{5/2}$	
515.3 CuI	$4d^2D_{3/2}$	0.30
510.6 CuI	$4p^2P^0_{3/2}$	0.25
461.2 InI	–	0.05
455.3 SII	$4p^{12}P^6_{3/2}$	0.05
451.1 InI	$6^2S_{3/2}$	1.00
441.1 SI	$6p^3P_{0,\,1,\,2}$	0.05
410.2 InI	$6^2S_{1/2}$	0.70
406.3 CuI	$5d^2D_{3/2,\,5/2}$	0.10
402.3 CuI	$5d^2D_{3/2}$	0.05
327.4 CuI	$4p^2P^0_{1/2}$	0.35
324.8 CuI	$4p^2P_{3/2}$	0.70
303.9 InI	$5d^2D_{3/2}$	0.65
293.2 InI	$7^2S_{1/2}$	0.20
283.7 InI	$5^4P_{5/2}$	0.10
275.3 InI	$7^2S_{1/2}$	0.10
271.0 InI	$6d^2D_{5/2,\,3/2}$	0.45
256.0 InI	$6^2P_{3/2}$	0.15
252.2 InI	$7d^2D_{5/2,\,3/2}$	0.05
227.8 InI	–	0.10

1063-7850/03/2905-0408$24.00

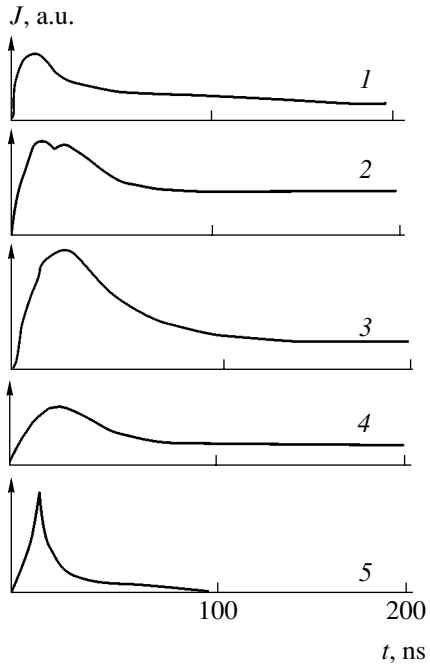

Fig. 1. Oscillograms showing the kinetics of line emission from the products of decomposition of a laser-ablated polycrystalline $CuInS_2$ target, measured at the center of the plasma torch (d = 1 mm): (*1*) 451.1 nm InI; (*2*) 410.2 nm InI; (*3*) 327.4 nm CuI; (*4*) 521.8 nm CuI; (*5*) 271.0 nm (InI).

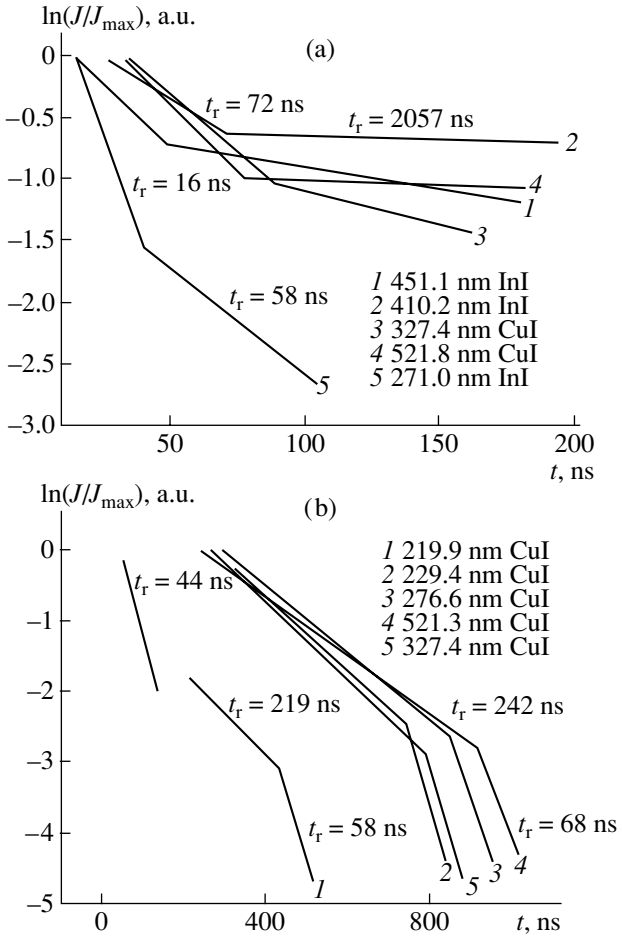

Fig. 2. Logarithmic diagrams for determining the recombination times t_r of ions at the center of the plasma torch of laser-ablated (a) polycrystalline $CuInS_2$ and (b) pure copper targets.

InII and no lines from the shifted levels of copper, which gave significant contributions to the line emission from indium and copper plasmas [5, 6]. A bottleneck in the recombination flux of the laser plasma of the polycrystalline target was the atomic level SI ($8d^5D^0_{0-4}$); E = 10.12 eV and the ion level SII ($4p^{12}P^6_{3/2}$); E = 17.81 eV.

Figure 1 shows oscillograms of the line emission from a multicomponent plasma, which mostly appear as a single pronounced maximum followed by an extended trailing front. The duration of emission of the spectral lines corresponding to the products of decomposition of the polycrystalline compound studied decreased with increasing energy of the upper occupied state. The spectral lines of emission from the lower energy states of indium exhibited an additional poorly resolved maximum, which, together with the presence of SI and SII lines, confirmed a dissociative mechanism of the formation of excited atoms in the laser plasma of the polycrystalline target.

In the case of laser plasmas of pure copper and indium, each oscillogram exhibited a pair of peaks. As the distance to the target surface increased, the two peaks either merged into one (for the spectral lines of the upper energy states of atoms) or separated into several peaks (for the spectral lines of lower levels). The nature of these peaks is determined by the laser-induced photoablation at the initial time and by the emission from subsequently heated and evaporated internal layers of the target [9]. Similar behavior of the emission intensity was observed for the spectral lines of metals and other products of the laser ablation of crystals [10, 11].

The kinetics of the laser plasma formation in the case of multicomponent targets is rather complicated. For this reason, we compared the recombination times determined for ions in the plasmas of $CuInS_2$ and pure copper (Fig. 2). The recombination times of singly charged ions in the plasma of $CuInS_2$ range from 16 to 2057 ns. This process involves fast and slow stages of the recombination of singly charged products of decomposition of the initial compound or $CuInS_2^+$ ions with electrons, which results in the formation of excited copper and indium atoms entering into the multicomponent laser plasma. Our study of the recombination times in the In and Cu laser plasmas at a distance of d = 1 mm from the target showed that $t_r(Cu^+)$ = 44–242 ns

and $t_r(In^+)$ = 14–442 ns. These laser plasmas were also characterized by two (slow and fast) stages of recombination of the corresponding singly charged ions, but the lengths of these stages were inversely proportional to those observed in the multicomponent laser plasma of a polycrystalline target.

The lower boundary of the recombination times indicates the true value, while the upper boundary provides information on the intensity of kinetic reactions in the plasma. This is related to the small rate of emission from atoms, the trailing edge of which was used to determine these times, especially at the onset of the intensity decay (where the inversion of level populations is clearly pronounced).

Thus, the results of our study of the dynamics of emission from the plasma formed during laser ablation of a polycrystalline $CuInS_2$ target showed that the spectral lines of copper and indium atoms are most suited for the spectroscopic diagnostics of this multicomponent plasma. The rate of recombination of the singly charged ions formed during the laser ablation of $CuInS_2$ is about ten times that of Cu^+ and In^+ ions in laser plasmas of corresponding pure metals. The results can be used for monitoring of the laser plasma parameters in the course of fabrication of the corresponding solar cell elements.

REFERENCES

1. R. Sheer, T. Walter, H. W. Schok, *et al.*, Appl. Phys. Lett. **63**, 3294 (1993).
2. V. A. Ivanov, I. A. Viktorov, and V. F. Gremenyuk, Zh. Tekh. Fiz. **72** (9), 134 (2002) [Tech. Phys. **47**, 1197 (2002)].
3. I. É. Kacher, I. I. Opachko, and M. Yu. Rigan, Ukr. Fiz. Zh. **34**, 1728 (1989).
4. A. K. Shuaibov, I. É. Kacher, and A. I. Dashchenko, Pis'ma Zh. Tekh. Fiz. **26** (23), 66 (2000) [Tech. Phys. Lett. **26**, 1058 (2000)].
5. A. K. Shuaibov, A. I. Dashchenko, and I. V. Shevera, Pis'ma Zh. Tekh. Fiz. **26** (18), 57 (2000) [Tech. Phys. Lett. **26**, 832 (2000)].
6. A. K. Shuaibov, L. L. Shimon, A. I. Dashchenko, and I. É. Kacher, Opt. Spektrosk. **90**, 560 (2001) [Opt. Spectrosc. **90**, 493 (2001)].
7. A. K. Shuaibov, L. L. Shimon, A. I. Dashchenko, *et al.*, Fiz. Plazmy **27**, 85 (2001) [Plasma Phys. Rep. **27**, 82 (2001)].
8. I. É. Kacher, A. K. Shuaibov, and A. I. Dashchenko, Prib. Tekh. Éksp. **44** (5), 152 (2001).
9. O. A. Novodvorskiĭ, E. O. Filipova, O. D. Khramova, *et al.*, Kvantovaya Élektron. (Moscow) **31**, 1159 (2001).
10. V. S. Burakov, N. A. Savostenko, and N. V. Tarasenko, Zh. Prikl. Spektrosk. **66**, 111 (1999).
11. T. J. Geier and W. Weimer, Appl. Spectrosc. **44**, 1659 (1990).

Translated by P. Pozdeev

Technical Physics Letters, Vol. 29, No. 5, 2003, pp. 411–413. Translated from Pis'ma v Zhurnal Tekhnicheskoĭ Fiziki, Vol. 29, No. 10, 2003, pp. 29–35.

Electron Beams Formed in a Diode Filled with Air or Nitrogen at Atmospheric Pressure

S. B. Alekseev, V. M. Orlovskiĭ, and V. F. Tarasenko*

Institute of High-Current Electronics, Siberian Division, Russian Academy of Sciences, Tomsk, Russia

** e-mail: VFT@loi.hcei.tsc.ru*

Received December 9, 2002

Abstract—We have studied the electron beam formation in a diode filled with a molecular gas at atmospheric pressure. A beam current amplitude of up to ~20 A at an electron energy of ~70 keV was obtained in an air-filled diode. It is suggested that the main fraction of runaway electrons at low initial values of the parameter E/p (~0.1 kV/(cm Torr)) is formed in the space between cathode plasma and anode. As the plasma spreads from cathode to anode, the electric field strength between the plasma front and anode increases and the E/p value reaches a critical level. *© 2003 MAIK "Nauka/Interperiodica".*

Introduction. The problems of electron beam formation in gas-filled diodes have been given much attention (see, e.g., [1–9] and references therein). Of special interest are the results of experiments [2–4], where electron or X-ray radiation beams were generated at a molecular gas pressure in a diode on the order of 1 atm. However, the number of accelerated electrons in a beam formed at atmospheric pressure was relatively small: ~10^9 [2–4], which (for a pulse duration of 1 ns) corresponded to a beam current amplitude of ~ 0.2 A behind the foil. Recently, Kolyada [5] obtained a beam current of about 1 kA at a pulse duration of ~1 μs. However, this result was obtained in a diode with the anode–cathode gap filled with a plasma characterized by low density during the voltage application at a deposited energy of ~20 kJ. Under the experimental conditions studied in [6–8], electron beams were formed at high E/p values (>1 kV/(cm atm)).

The aim of our experiments was to obtain an electron beam in a diode filled with air or nitrogen at atmospheric pressure and to analyze conditions of the electron beam formation at high gas pressures in the diode and small E/p values.

Experimental. The experiments were performed in systems employing two nanosecond pulse generators [10, 11] and four cathodes. Generator 1 possessed a wave impedance of 30 Ω and produced in a matched load a voltage pulse of ~200 kV amplitude, a full width at half maximum (FWHM) of ~3 ns, and a front width of ~1 ns [10]. Cathode 1 comprised a set of three coaxial cylinders (12, 22, and 30 mm in diameter) made of a 50-μm-thick titanium foil, embedded into one another and fastened on a duralumin substrate (36 mm in a diameter) so that the cylinder ring height decreased by 2 mm on the passage from smaller to greater ring. Cathode 2 represented a graphite disk with a diameter of 29 mm and rounded edges. The disk surface facing the foil was convex with a curvature radius of 10 cm. The cathode–anode spacing in this system was varied within 10–28 mm.

Generator 2 possessed a wave impedance of 20 Ω and produced in the discharge gap a voltage pulse with an amplitude of up to ~220 kV, a FWHM of ~2 ns, and a front width of ~0.3 ns [11]. Cathode 3 was a tube with a diameter of 6 mm, made of the same 50-μm-thick titanium foil. Cathode 4 was a graphite disk with a diameter of 6 mm and rounded edges. The cathode–anode spacing in this diode system was 16 mm.

The electron beam was extracted from the diode via a 45-μm-thick AlBe foil. The beam current was measured with a graphite electrode placed (in air or in vacuum) at a distance of 10 mm from the foil and connected with a low-ohmic shunt to an amplifier. The electron energy distribution was determined by the foil technique. The electron beam energy was measured with an IMO-2N calorimeter. In addition, we photographed the electron-beam induced luminescence of a phosphor target. The signals from the probing shunts were registered using a TDS-332 oscillograph.

Results. The values of the current amplitude measured behind the foil are presented in the table. In the first system, we obtained electron beams at atmospheric pressure (1 atm) in air, nitrogen, helium, and a CO_2–N_2–He mixture both in a single-pulse mode and at a repetition frequency of up to 5 Hz. Using the second system filled with air, we obtained a maximum electron beam current of 20 A, which is more than ten times the current values reported so far [2–4]. The maximum in the electron energy distribution for the beam obtained with generator 1 and cathode 1 at an air pressure of 1 atm corresponded to ~95 keV, while the same with generator 2 and cathode 4 was at ~70 keV (Fig. 1).

Figure 2 shows plots of the beam current behind the foil versus the interelectrode distance at a gas pressure

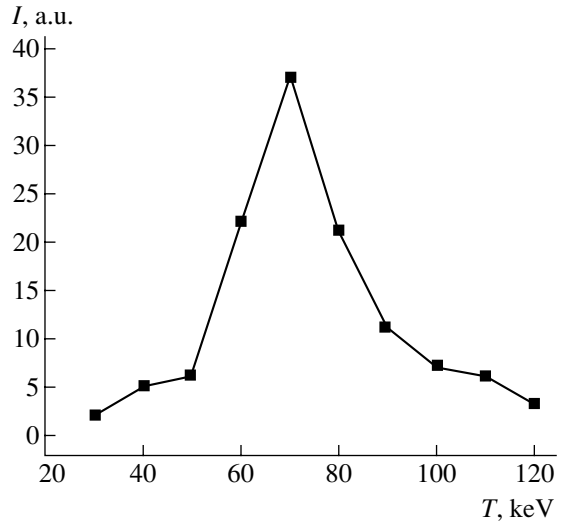

Fig. 1. Electron energy distribution in the beam measured behind the foil in a diode filled with air at 1 atm (generator 2/cathode 4).

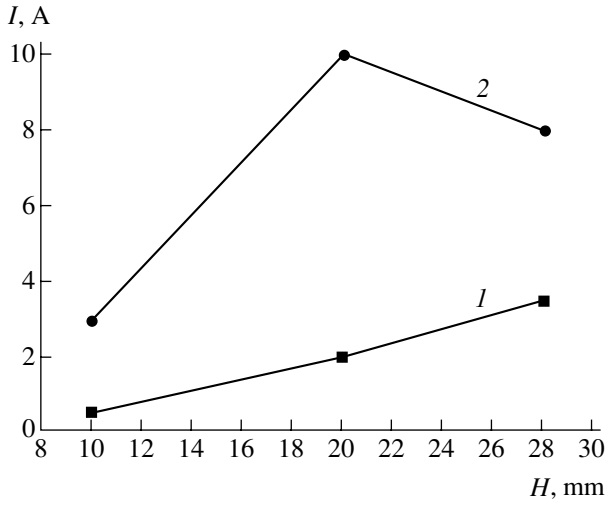

Fig. 2. Experimental plots of the beam current amplitude behind the foil versus gap width in a diode filled with (*1*) N_2 and (*2*) air at a pressure of 1 atm.

of 1 atm in the diode with generator 1. As can be seen, an increase in the cathode–foil spacing to 28 mm led to a monotonic growth in the beam current in nitrogen, while the beam current in air exhibited a maximum at 20 mm. It should be noted that the discharge shape in the diode and the beam current amplitude were strongly influenced by the cathode design. Various forms of discharge in systems with various cathodes and different interelectrode distances were also observed in [1, 2, 4].

Similarly to what was reported in [2, 4], we have observed electrons with energies exceeding that corresponding to the voltage applied to the diode, but the density of such particles was significantly lower as compared to that at the maximum of the electron energy distribution in the beam. The beam current pulse duration was shorter than that of the voltage pulse and amounted to ~1 ns (FWHM) for both generators (Fig. 3). The time resolution of our beam registration system was also about 1 ns. The electron beam energy measured with an IMO-2N calorimeter for the air-filled diode was 1.2 mJ with generator 1 and 1.6 mJ with generator 2. The effective current pulse duration calculated using the beam energy, average electron energy, and current amplitude was 1–1.5 ns.

Discussion. The value of E/p under the experimental conditions studied was small and corresponded to the right-hand branch of the Paschen curve. According to [9], the electron runaway criterion is $E_c/p = 3.88 \times 10^3 Z/I$, where E_c/p [V/(cm Torr)] is the critical field strength divided by pressure, Z is the atomic number, and I [eV] is the mean energy of inelastic losses. For air with I = 15–80 eV, this relation yields E_c/p = 0.8–3.5 kV/(cm Torr). In the diode with a 20–28 mm gap width and an initial applied voltage of ~200 kV, this parameter is $E/p \sim 0.09$–0.13 kV/(cm Torr). Therefore, the voltage used in our experiments was insufficient to produce runaway electrons.

The above results can be explained as follows. Upon breakdown of the gas-filled diode gap, a plasma generated in the form of channels or a cloud shunts the gap within a time period on the order of a few nanoseconds or even a fraction of a nanosecond. The motion of the

Electron beam currents measured behind the foil in a diode filled with various gases at atmospheric pressure

Diode system (generator/cathode)	Cathode–anode gap width, mm	Beam current *I*, A			
		N_2	Air	He	CO_2–N_2–He (1 : 1 : 3)
1/1	20	2	10	25	n/m
1/1	28	3.5	8	60	12
1/2	28	–	–	200	n/m
2/3	16	n/m	13.8	n/m	n/m
2/4	16	n/m	20	n/m	n/m

Note: n/m—not measured.

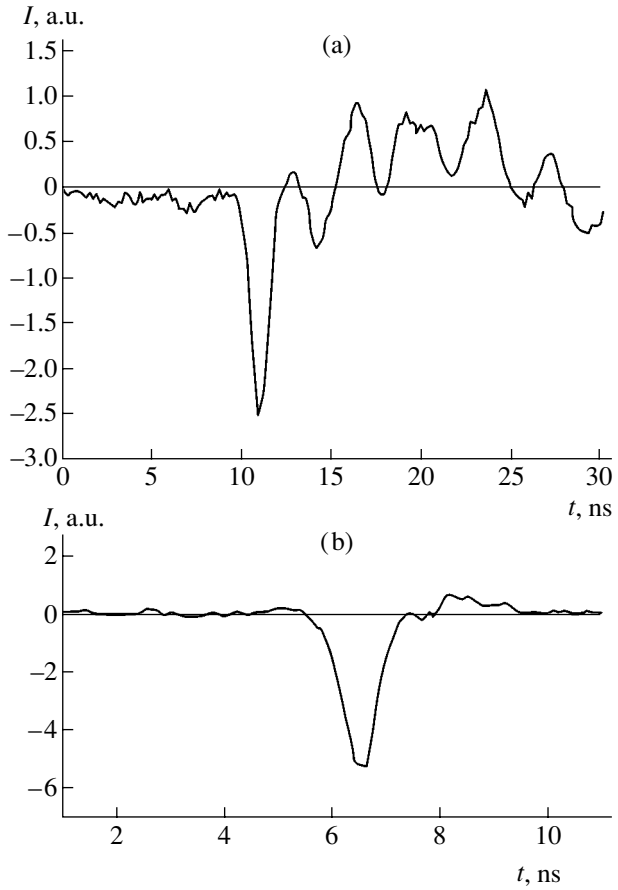

Fig. 3. Oscillograms of the electron beam current behind the foil, measured (a) in air (generator 1/cathode 1) and (b) in vacuum (generator 2/cathode 4) for a diode filled with air at a pressure of 1 atm.

plasma cloud or channels (appearing at the cathode and possessing greater conductivity as compared to the other part of the gap) leads to redistribution of the electric field in the gap, whereby a critical field strength is developed in the region between plasma and foil. This mechanism explains the production of runaway electrons and X-ray emission at low fields and high pressures. The electric field strength at the cathode and in the gap can be additionally increased due to the geometric factor.

Realization of the proposed mechanism requires that a voltage buildup rate in the gap would be sufficiently high, since the plasma shortens the gap upon breakdown in the pulse front. This mechanism can also be operative during pulse discharges of other types, for example, in long tubes [12] and in the case of a surface discharge [13]. Note that runaway electrons of sufficiently high energy appearing at the cathode (e.g., due to the field enhancement at sharp microscopic points) can travel over rather long distances without significant energy losses at relatively small values of the parameter E/p [14].

Conclusion. We obtained an electron beam at a relatively low value of the parameter E/p in a diode filled with molecular and atomic gases at atmospheric pressure. Gas-filled diodes operating at a pressure of 1 atm and above can be used to obtain electron beams of short duration (fractions of a nanosecond). In order to provide conditions for the formation of a beam of runaway electrons at increasing gas pressure in the diode, it is necessary to reduce the width of the voltage pulse front.

Acknowledgments. The authors are grateful to LLNL (contract No. B506095) and Dr. V. Hasson for their support of this study and to S.D. Korovin and V.G. Shpak for kindly providing nanosecond pulse generators.

REFERENCES

1. L. V. Tarasova and L. N. Khudyakova, Zh. Tekh. Fiz. **39**, 1530 (1969) [Sov. Phys. Tech. Phys. **14**, 1148 (1969)].
2. L. V. Tarasova, L. N. Khudyakova, T. V. Loĭko, and V. A. Tsukerman, Zh. Tekh. Fiz. **44**, 564 (1974) [Sov. Phys. Tech. Phys. **19**, 351 (1974)].
3. L. P. Babich and T. V. Loĭko, Prib. Tekh. Éksp. **32** (2), 188 (1989).
4. L. P. Babich, T. V. Loĭko, and V. A. Tsukerman, Usp. Fiz. Nauk **160** (7), 49 (1990) [Sov. Phys. Usp. **33**, 521 (1990)].
5. Yu. E. Kolyada, Pis'ma Zh. Tekh. Fiz. **26** (16), 52 (2000) [Tech. Phys. Lett. **26**, 721 (2000)].
6. G. V. Kolbychev, P. D. Kolbycheva, and I. V. Ptashnik, Zh. Tekh. Fiz. **66** (2), 59 (1996) [Tech. Phys. **41**, 144 (1996)].
7. A. R. Sorokin, Pis'ma Zh. Tekh. Fiz. **28** (9), 14 (2002) [Tech. Phys. Lett. **28**, 361 (2002)].
8. A. P. Bokhan and D. E. Zakrevsky, Pis'ma Zh. Tekh. Fiz. **28** (11), 21 (2002) [Tech. Phys. Lett. **28**, 454 (2002)].
9. Yu. D. Korolev and G. A. Mesyats, *The Physics of Pulsed Breakdown in Gases* (Nauka, Moscow, 1991).
10. V. P. Gubanov, S. D. Korovin, I. V. Pegel', *et al.*, Izv. Vyssh. Ucheb. Zaved., Fiz., No. 12, 110 (1996).
11. F. Ya. Zagulov, A. S. Kotov, V. G. Shpak, *et al.*, Prib. Tekh. Éksp. **32** (2), 146 (1989).
12. É. I. Asinovskiĭ, V. V. Markovets, D. N. Polyakov, *et al.*, Teplofiz. Vys. Temp. **23**, 606 (1985).
13. P. N. Dashuk and S. L. Kulakov, Pis'ma Zh. Tekh. Fiz. **5** (2), 69 (1979) [Sov. Tech. Phys. Lett. **5**, 26 (1979)].
14. L. P. Babich, E. N. Donskoy, R. L. Il'kaev, *et al.*, Dokl. Akad. Nauk **382**, 31 (2002) [Dokl. Phys. **46** (8), 536 (2002)].

Translated by P. Pozdeev

Technical Physics Letters, Vol. 29, No. 5, 2003, pp. 414–417. Translated from Pis'ma v Zhurnal Tekhnicheskoĭ Fiziki, Vol. 29, No. 10, 2003, pp. 36–44.

Peculiarities of the Resistive Transition in Fractal Superconducting Structures

Yu. I. Kuzmin

Ioffe Physicotechnical Institute, Russian Academy of Sciences, St. Petersburg, 194021 Russia
e-mail: yurk@mail.ioffe.ru; iourk@yandex.ru

Received December 24, 2002

Abstract—The influence of fractal clusters of a normal phase on the current–voltage characteristics of a percolation superconductor in the region of a resistive transition has been studied. The clusters appear as aggregates of columnar defects, the presence of which leads to a correlated microscopic disorder in the system. Dependences of the static and dynamic resistance on the transport current are determined for an arbitrary fractal dimension of the cluster boundaries. In the case under consideration, the superconducting system features a mixed state of the vortex glass type. © *2003 MAIK "Nauka/Interperiodica".*

Fractal superconducting structures possess a number of unusual magnetic and transport properties [1–3]. Of much interest is the possibility to enhance pinning by trapping the magnetic flux in the normal phase clusters with fractal boundaries [4–6]. The study of peculiarities of the current–voltage characteristics of these structures in the region of a resistive transition can provide new information about the nature of the vortex state in such systems.

Formulation of the problem was described in detail previously [1, 2]. We will consider a superconductor containing columnar fragments of a normal phase representing either inclusions of different chemical composition or regions with reduced superconducting order parameter. Such columnar defects can be formed during the film growth or induced by heavy ion bombardment [7, 8]. The columnar defects can produce a much more intensive pinning than that caused by, for example, point defects, because their topology is closer to a vortex structure [9, 10]. The presence of columnar defects in a superconductor enhances irreversible magnetization, on the one hand, and suppresses the magnetic flux creep, on the other hand, which allows the critical current to be increased up to a level of depairing current [11, 12].

When a sample is cooled in a magnetic field below the critical temperature, the magnetic flux is trapped in isolated clusters of the normal phase. Then a transport current is passed through the sample in the direction perpendicular to the magnetic field. The transport current adds to persistent superconducting currents circulating around the normal phase clusters and maintaining unchanged distribution of the trapped magnetic flux. By a cluster we mean a set of columnar defects united by a common trapped flux and surrounded by the superconducting phase. Since the distribution of the trapped magnetic flux is two-dimensional, we will consider the transverse cross section of the clusters, representing extended objects, by a plane carrying the transport current.

As established for the first time in [1], normal phase clusters can possess fractal boundaries. This property significantly influences the dynamics of a trapped magnetic flux [2, 4, 6]. Below we will consider a special case when the characteristic dimensions of the normal phase clusters significantly exceed both the coherence length and the penetration depth. This assumption agrees well with the data about the cluster structure of YBCO based high-T_c superconductor films [1, 2] and is most consistent with the important role of cluster boundaries in the magnetic flux trapping.

It is assumed that a superconducting percolation cluster is formed in the plane where the electric current flows. Such a structure provides for an effective pinning, since the magnetic field is trapped in finite clusters of the normal phase. As the transport current increases, a moment comes when vortices begin to break away from the clusters in which the pinning force is smaller than the Lorentz force created by the current. With gradually increasing transport current, the vortices will break away first from the clusters of a smaller pinning force and, accordingly, of a lower critical current. The vortices will travel through the superconducting space via weak links connecting the clusters of the normal phase and playing the role of channels for the magnetic flux transport. These weak links are formed especially readily at various structural defects in high-T_c superconductors possessing small correlation lengths. Thus, weak links in high-T_c superconductors are created by the defects which could otherwise (at a greater coherence length) only account for an additional scattering.

The motion of vortices broken away from pinning centers results into a voltage drop across the sample and

1063-7850/03/2905-0414$24.00 © 2003 MAIK "Nauka/Interperiodica"

causes transition to the resistive state. Each cluster possesses an individual configuration of weak links and gives its own contribution to the total static distribution of critical currents. The critical current of a cluster is proportional to the pinning force and is equal to the current at which the magnetic flux can no longer be held inside the normal phase cluster. Various types of the critical current distribution for the clusters with fractal boundaries (the most general case being a distribution of the gamma-function type) were recently considered in [3, 4, 6, 13].

Below, the consideration is restricted to the practically most important case of an exponential-hyperbolic distribution of critical current,

$$f(i) = \frac{2C}{D} i^{-\frac{2}{D}-1} \exp\left(-Ci^{-\frac{2}{D}}\right), \quad (1)$$

which is realized in YBCO based film structures with exponential distribution of the cluster areas [1, 2]. In expression (1), $i \equiv I/I_c$ is the dimensionless current normalized to the critical current of the transition to the resistive state, $I_c \equiv \alpha(C\bar{A})^{-D/2}$, I is the transport current, D is the fractal dimension of the cluster boundary, $C \equiv ((2 + D)/2)^{2/D+1}$ is the constant depending on the fractal dimension, $\bar{A}$ is the average cluster area, and α is the cluster form factor.

The fractal dimension D determines a scaling relationship between the perimeter P and area A of the normal phase cluster: $P^{1/D} \propto A^{1/2}$. This relation is consistent with the generalized Euclidean theorem, according to which the ratios of corresponding geometric measures are equal when reduced to the same dimension [14]. For the Euclidean clusters, the fractal dimension coincides with the topological dimension of line ($D = 1$), while the dimension of fractal clusters always exceeds the topological value ($D > 1$) to reach maximum ($D = 2$) for the clusters of maximum fractality. A fractal object possesses fractional dimension. In the case under consideration, this reflects the highly indented shape of the cluster boundary [14]. Note that the probability density for the exponential-hyperbolic distribution (1) is exactly zero at $i = 0$, which implies the absence of any contribution from negative and zero currents. This will allow us to avoid an artificial assumption about the existence of a "vortex liquid" featuring free vortices and possessing a finite resistance in the absence of transport currents: $r(i \longrightarrow 0) \neq 0$. This assumption is made, for example, in the case of a normal distribution of critical currents [15].

The voltage drop across a superconductor in the resistive state represents an integral response of all clusters to the action of transport current:

$$u = r_f \int_0^i (i - i') f(i') di', \quad (2)$$

where u is the dimensionless voltage and r_f is the dimensionless resistance of the flux flow. Using the convolution integral of type (2), it is possible to determine the current–voltage characteristics of fractal superconducting structures of an arbitrary fractal dimension and to study the dependence of resistance on the transport current. The resistive characteristics provide important information about the nature of the vortex state in a given superconducting system. The standard parameters are the dc (static) resistance, $r \equiv u/i$, and the differential (dynamic) resistance $r_d \equiv du/di$. The corresponding dimensional quantities R and R_d can be calculated using the formulas $R = rR_f/r_f$ and $R_d = r_d R_f/r_f$, where R_f is the dimensional flux flow resistance.

For an exponential-hyperbolic distribution of critical currents described by formula (1), expressions for the resistances of a superconductor with fractal clusters of the normal phase are as follows:

$$r = r_f \left[\exp\left(-Ci^{-\frac{2}{D}}\right) - \frac{C^{\frac{D}{2}}}{i} \Gamma\left(1 - \frac{D}{2}, Ci^{-\frac{2}{D}}\right) \right], \quad (3)$$

$$r_d = r_f \exp\left(-Ci^{-\frac{2}{D}}\right), \quad (4)$$

where $\Gamma(\nu, z)$ is the complementary incomplete gamma-function. In the limiting cases of the Euclidean clusters ($D = 1$) and the clusters with most fractal boundaries ($D = 2$), the above formulas simplify to yield

$$D = 1:$$

$$r = r_f \left[\exp\left(-\frac{3.375}{i^2}\right) - \frac{\sqrt{3.375\pi}}{i} \mathrm{erfc}\left(\frac{\sqrt{3.375}}{i}\right) \right],$$

$$r_d = r_f \exp\left(-\frac{3.375}{i^2}\right),$$

where $\mathrm{erfc}(z)$ is the complementary error function, and

$$D = 2:$$

$$r = r_f \left[\exp\left(-\frac{4}{i}\right) + \frac{4}{i} Ei\left(-\frac{4}{i}\right) \right],$$

$$r_d = r_f \exp\left(-\frac{4}{i}\right),$$

where $Ei(z)$ is the exponential integral function.

Figure 1 shows plots of the dc resistance versus transport current for a superconductor with fractal clusters of the normal phase. The curves constructed for the Euclidean clusters ($D = 1$) and the clusters with most fractal boundaries ($D = 2$) bound a region containing the resistive characteristics for arbitrary fractal dimensions. For example, the dashed curve presents a curve

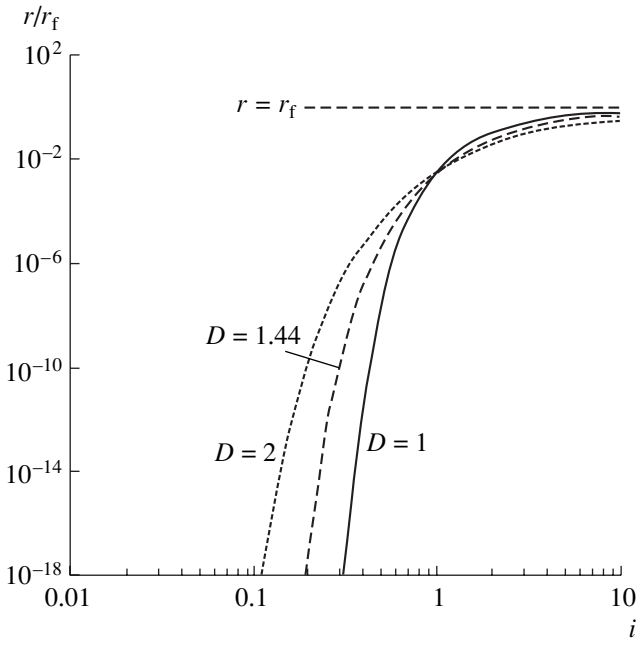

Fig. 1. Plots of the dc resistance versus transport current for a superconductor with fractal normal phase clusters (D is the fractal dimension). The dashed straight line $r = r_f$ in the topright part corresponds to a viscous flow of the magnetic flux.

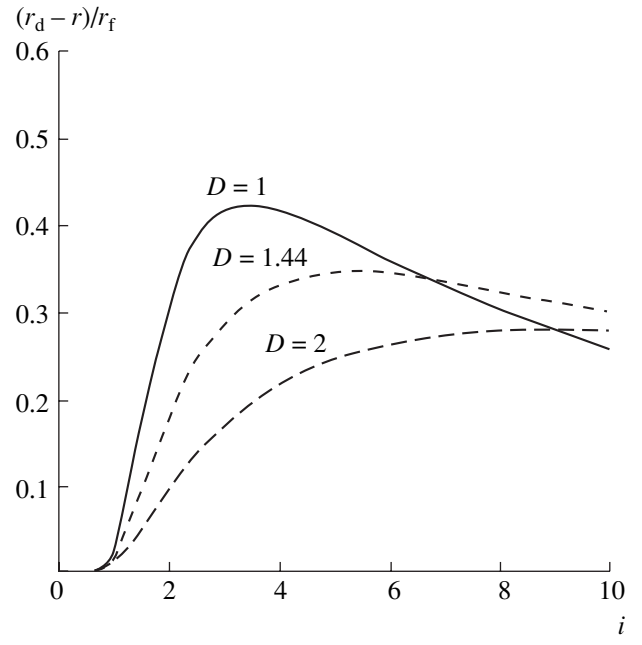

Fig. 2. A comparison of the dc resistance and the differential resistance for a superconductor with the normal phase clusters of various dimensions D.

for the fractal dimension $D = 1.44$ constructed by data of the geometric-probabilistic analysis of the electron micrographs of YBCO based superconducting film structures [1]. The dependences of resistance on the current in Fig. 1 are typical of the vortex glass, whereby the curves plotted in a double logarithmic scale are convex and the resistance tends to zero as the transport current decreases, $r(i \longrightarrow 0) \longrightarrow 0$ which is related to suppression of the magnetic field creep [15, 16]. A vortex glass represents an ordered system of vortices which has no long-range order. At the same time, the vortex configuration is stable in time and can be characterized by the order parameter of the glassy state [17, 18]. In the H–T phase diagram, a mixed state of the vortex glass type exist in the region below the irreversibility line. The dashed straight line in the topright part of Fig. 1 corresponds to a viscous flux flow regime ($r = r_f = \text{const}$), which can be achieved only asymptotically.

Since the current–voltage characteristic (2) of a fractal superconducting structure is nonlinear, the dc resistance (3) is not constant and depends on the transport current. In this situation, important information is provided by the differential resistance, a small-signal parameter determined by the slope of the current–voltage characteristic. The plots of the differential resistance versus transport current are qualitatively analogous to the resistance curves presented in Fig. 1. The difference between these characteristics can be seen in Fig. 2. As the fractal dimension grows, the two parameters behave more like each other, the difference being manifested in a wider range of transport currents in the latter case. This is related to the fact that, as the fractal dimension increases, the exponential-hyperbolic distribution of critical currents (1) broadens, moving toward greater i values [2, 13].

The differential resistance is determined by the density of vortices broken away from pinning centers by the transport current i,

$$n = \frac{B}{\Phi_0}\int_0^i f(i')di' = \frac{B}{\Phi_0}\exp\left(-Ci^{-\frac{2}{D}}\right), \qquad (5)$$

where B is the magnetic field, $\Phi_0 \equiv hc/(2e)$ is the magnetic flux quantum, h is the Planck constant, c is the speed of light, and e is the electron charge. A comparison of expressions (4) and (5) shows that the differential resistance is proportional to the density of free vortices: $r_d = (r_f\Phi_0/B)n$. The resistance of a superconductor in the resistive state is determined by the motion of these very vortices, because it leads to the appearance of voltage across the sample.

The vortices are broken away from pinning centers mostly when $i > 1$, that is, above the resistive transition. A practically important property of the fractal superconducting structures consists in the fact that the fractal character of cluster boundaries enhances pinning [5] and, hence, decreases the electric field induced in the superconductor by the magnetic flux motion [4]. This is manifested both in Fig. 1, where the resistance decreases with increasing fractal dimension above the resistive transition, and in Fig. 2, where an increase in the fractal dimension of cluster boundaries leads to a

decrease in the relative difference between the differential resistance and the dc resistance.

In the range of transport currents below the resistive transition ($i < 1$), the situation changes to the opposite: the resistance increases for clusters of greater fractal dimension (Fig. 1). This behavior is related to the fact that, as the fractal dimension increases, the exponential-hyperbolic distribution of critical currents (1) broadens, covering both greater and smaller currents. For this reason, the separation of vortices under the action of transport current begins earlier for the clusters of greater fractal dimension. The range of currents under consideration is characterized by a small number of free vortices (which is much smaller than that above the resistive transition) and, accordingly, by a low resistance (Fig. 1). This interval corresponds to the so-called initial fractal dissipation region, which was observed in BPSCCO samples with silver inclusions, as well as in polycrystalline YBCO and GdBCO samples [19].

Thus, the fractal properties of clusters of the normal phase significantly influence the resistive transition. This phenomenon is related to the properties of the fractal distribution of critical currents. The relations established between the resistance and the transport current correspond to a mixed state of the vortex glass type. An important finding of this study is that the fractal character of the normal phase clusters enhances pinning, thus decreasing the resistance of a superconductor upon transition to the resistive state.

Acknowledgments. This study was supported by the Russian Foundation for Basic Research, project no. 02-02-17667.

REFERENCES

1. Yu. I. Kuzmin, Phys. Lett. A **267**, 66 (2000).
2. Yu. I. Kuzmin, Phys. Rev. B **64**, 094519 (2001).
3. Yu. I. Kuzmin, Phys. Lett. A **300**, 510 (2002).
4. Yu. I. Kuzmin, Phys. Lett. A **281**, 39 (2001).
5. Yu. I. Kuzmin, Pis'ma Zh. Tekh. Fiz. **26** (17), 81 (2000) [Tech. Phys. Lett. **26**, 791 (2000)].
6. Yu. I. Kuzmin, Fiz. Tverd. Tela (St. Petersburg) **43**, 1157 (2001) [Phys. Solid State **43**, 1199 (2001)].
7. E. Mezzetti, R. Gerbaldo, G. Ghigo, *et al.*, Phys. Rev. B **60**, 7623 (1999).
8. A. W. Smith, H. M. Jaeger, T. F. Rosenbaum, *et al.*, Phys. Rev. B **59**, R11665 (1999).
9. F. C. Klaassen, G. Doornbos, J. M. Huijbregtse, *et al.*, Phys. Rev. B **64**, 184523 (2001).
10. A. Tonomura, H. Kasai, O. Kamimura, *et al.*, Nature **412** (6847), 620 (2001).
11. Y. Yeshurun, A. P. Malozemoff, and A. Shaulov, Rev. Mod. Phys. **68**, 911 (1996).
12. M. Konczykowski, N. Chikumoto, V. M. Vinokur, and M. V. Feigelman, Phys. Rev. B **51**, 3957 (1995).
13. Yu. I. Kuzmin, Pis'ma Zh. Tekh. Fiz. **28** (13), 74 (2002) [Tech. Phys. Lett. **28**, 568 (2002)].
14. B. B. Mandelbrot, *The Fractal Geometry of Nature* (Freeman, San Francisco, 1982).
15. B. Brown, Phys. Rev. B **61**, 3267 (2000).
16. G. Blatter, M. V. Feigel'man, V. B. Geshkenbein, *et al.*, Rev. Mod. Phys. **66**, 1125 (1994).
17. M. P. A. Fisher, Phys. Rev. Lett. **62**, 1415 (1989).
18. D. S. Fisher, M. P. A. Fisher, and D. A. Huse, Phys. Rev. B **43**, 130 (1991).
19. M. Prester, Phys. Rev. B **60**, 3100 (1999).

Translated by P. Pozdeev

Technical Physics Letters, Vol. 29, No. 5, 2003, pp. 418–419. Translated from Pis'ma v Zhurnal Tekhnicheskoĭ Fiziki, Vol. 29, No. 10, 2003, pp. 45–48.

Microhardness of Gallium Crystals Grown in a Centrifuge

V. N. Gurin*, L. I. Derkachenko, S. P. Nikanorov, M. M. Korsukova, and I. N. Zimkin

Ioffe Physicotechnical Institute, Russian Academy of Sciences, St. Petersburg, 194021 Russia

** e-mail: vladimir.gurin@mail.ioffe.ru*

Received December 29, 2002

Abstract—Gallium single crystals with identified faces grown from melt under usual conditions are compared for the first time to those obtained under conditions of centrifugation at 15000*g*. The crystals grown in a centrifuge exhibit a change in the lattice parameters and possess a significantly higher microhardness. Crystals of both types are characterized by a strong polar anisotropy. *© 2003 MAIK "Nauka/Interperiodica".*

Previously [1], we established that the lattice parameters of gallium single crystals grown from melt in a centrifuge slightly vary depending on the acceleration [(1.3, 6.2, or 11.8) $\times 10^3 g$]. The value of a decreased, while the values of b and c increased with the centrifuge speed, so that the crystal lattice of gallium exhibited a certain distortion as compared to that in the samples grown under normal gravity conditions. It was suggested that such crystal distortions must lead to a significant change (increase) in microhardness of the material. However, it was difficult to correctly estimate the change in microhardness, because all measurements were performed on cleavages which could not be assigned to definite crystal faces or crystallographic directions (the as-grown samples did not represent single crystals).

In this study, we have succeeded in obtaining gallium crystals with clearly pronounced faces grown from the intrinsic melt both under normal gravity conditions and in a centrifuge. As can be seen from Fig. 1a, this sample grown under normal conditions comprises several gallium single crystals grown together in the form of triplets. The crystal layers grow perpendicularly to the third crystallographic axis (i.e., normally to the plane of the figure). The faceting of these crystals exhibits edges representing vertical faces of pinacoids and prisms growing along the z axis and intersecting one or both horizontal axes (x and y). A centrifuged sample shown in Fig. 1b exhibits faces of a truncated rhombic bipyramid.

The experiments were performed in a centrifuge of the K24D type with an arm length of 70 mm. The samples were grown from ultrahigh-purity metallic gallium (99.99997% Ga). The temperature inside the centrifuge was maintained at –10°C. Gallium melt was heated to 90°C, poured into polyethylene tubes, and centrifuged for 30 min at 15000*g*. The crystal lattice parameters of gallium crystals were determined by X-ray diffraction measurements in a DRON-2 diffractometer using FeK_α radiation (λ = 1.93597 Å). The microhardness measurements were performed at T = 20°C in a PMT-3 device with a Knoop pyramid indenter loaded at P = 98.1 mN (the experimental error was 7%).

After centrifugation, it was found that gallium in one tube (of the two balanced in the rotor) was completely crystallized, while it remained liquid in the other tube (except for a thin layer contacting with the tube surface). This difference can be related to the order of filling tubes in the course of balancing: because of cooling, the temperature of the melt filling the second tube is significantly (by approximately 10–15°C) lower than that in the first tube. For this reason, the melt in the second tube can more readily crystallize, while that in the first tube can remain liquid in a strongly supercooled state.

The X-ray diffraction measurements showed that the crystal lattice parameters of the centrifuged sample changed as compared to those of the reference (normal) samples (indicated in parentheses): a = 0.4491 (0.4535) nm; b = 0.4517 (0.4516 nm; c = 0.7689 (0.7645) nm (the experimental uncertainty is ±0.0003 nm). Note that the centrifugation "distorts" the crystal structure of gallium, so that the a value decreases, while the b and c values increase as compared to the analogous parameters of the reference crystal. As was pointed out in [1], this distortion probably makes the crystal structure strained, which must significantly increase the microhardness.

In this study, we have succeeded for the first time in establishing and measuring the polar anisotropy of microhardness for the rhombic bipyramid faces (111) in gallium single crystals. It was found that this anisotropy can reach a very high level. Indeed, the reference (noncentrifuged) gallium crystals showed H_K = 98 MPa at an azimuthal angle of 0°, 189 MPa at 45°, and 254 MPa at 90°. The corresponding values for the crystals grown in the centrifuge were significantly higher, reaching 172, 256, and 326 MPa, respectively (measurements at 90° in another part of this crystal gave

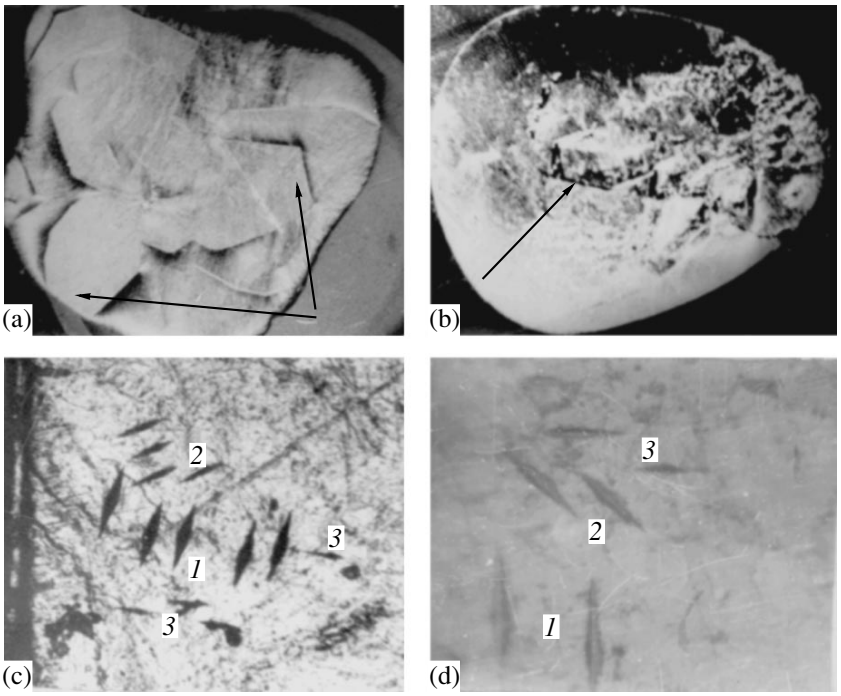

Fig. 1. Photographs showing (a, b) the crystallographic planes and (c, d) the marks of Knoop pyramid indenter on gallium crystals grown under (a, c) normal gravity conditions and (b, d) in a centrifuge. The arrows indicate (a) rhombic bipyramids (real scale) and (b) faces of truncated bipyramid at the center of the ingot (magnification, ×1.5). The Knoop indentation marks on the faces of rhombic bipyramids (c, ×80; d, ×230) correspond to three values of the azimuthal angle: (*1*) 0°, (*2*) 45°, and (*3*) 90°.

H_K = 577 MPa). Figures 1c and 1d show the photographs of both reference and centrifuged samples with indentation marks of the Knoop pyramid. On the reference sample (Fig. 1c), zero azimuth in the indentations was measured relative to the [100] edge of bipyramid. In the centrifuged sample (Fig. 1d), the marks were made on a bipyramid face growing in the direction [111] of the crystallographic axis and bounded by (001) pinacoid at the vertex; here, the direction of the common edge between the pinacoid and bipyramid determined zero azimuth in the indentations.

According to our experimental data, both reference and centrifuged gallium crystals are characterized by very high polar anisotropy of the microhardness. At the same time, we have unambiguously established that both solidified ingots and crystallized samples grown in a centrifuge (in particular, those obtained in the last experiment at 15000*g*) possess a significantly higher microhardness than the analogous non-centrifuged samples. This phenomenon is probably explained by straining of the crystal structure of gallium solidified in the centrifuge, as evidenced by essential (albeit small) changes in the crystal lattice parameters. The changes are apparently sufficient to account for a large increase in the microhardness. This, in turn, can be due to mechanical stresses developed in the sample as a result of the crystal lattice distortion. We are planning investigations aimed at determining the dislocation density and the stressed state of gallium crystals, which will probably elucidate the factors that account for the observed increase in the microhardness of gallium crystallized under the action of elevated gravity.

Thus, we have established that the samples of metallic gallium grown under normal gravity conditions and in a centrifuge possess a high polar anisotropy of the microhardness. The microhardness of centrifuged gallium is significantly higher as compared to that of the samples obtained under normal conditions. The difference is probably explained by a small distortion of the crystal lattice of gallium caused by centrifugation.

Acknowledgments. This study was supported by the Russian Foundation for Basic Research, project no. 01-03-32822.

REFERENCES

1. V. N. Gurin, L. I. Derkachenko, I. N. Zimkin, *et al.*, Pis'ma Zh. Tekh. Fiz. **28** (4), 78 (2002) [Tech. Phys. Lett. **28**, 162 (2002)].

Translated by P. Pozdeev

Technical Physics Letters, Vol. 29, No. 5, 2003, pp. 420–421. Translated from Pis'ma v Zhurnal Tekhnicheskoĭ Fiziki, Vol. 29, No. 10, 2003, pp. 49–53.

The Effect of Illumination on the Current–Voltage Characteristics and Conductivity of $MnGaInS_4$ Single Crystals

N. N. Niftiev and O. B. Tagiev

Azerbaijan State Pedagogical University, Baku, Azerbaijan

Received November 25, 2002

Abstract—We have studied the effect of illumination on the current–voltage characteristics and the temperature dependence of conductivity of $MnGaInS_4$ single crystals. Under illumination, the current in a sample was 10^4–10^5 times the dark value. It is established that the light-induced current buildup is due to the carrier release from the traps filled under illumination. The energy positions of levels are determined. © *2003 MAIK "Nauka/Interperiodica".*

In recent years, semimagnetic semiconductors of the $A^{II}B_2^{III}X_4^{VI}$ type containing elements with incompletely filled *d* shells (A = Mn, Fe, Co, Ni; B = Ga, In; X = S, Se, Te) have received much attention [1–6]. These compounds offer a promising base for the creation of lasers, light modulators, photodetectors, and some other devices controlled by magnetic field. Previously [5, 6], we obtained layered semimagnetic semiconductor single crystals with a composition of $MnGaInS_4$, representing 1 : 1 mixtures of spinel $MnIn_2S_4$ (space group $Fd3m$) and tetragonal $MnGa_2S_4$ (space group 14) structures, and studied their electrical and optical properties.

This Letter presents the results of our investigation of the effect of illumination on the current–voltage characteristics and the temperature dependence of conductivity of $MnGaInS_4$ single crystals.

The samples of $MnGaInS_4$ single crystals were grown from melt by the Bridgman method. X-ray diffraction measurements showed that the singe crystal structure belongs to a single-pack $ZnIn_2S_4$ polytype [7] with the unit cell parameters a = 8.31 Å, c = 12.17 Å, Z = 1 (space group, $P3ml$). The electrical measurements were performed on sandwich structures with fused indium contacts.

Figure 1 shows typical current–voltage (*I–U*) characteristics of an In–$MnGaInS_4$–In structure measured in the dark (curve *1*) and under illumination with a white light (curve *2*) at 294 K. As can be seen, the *I–U* characteristic measured in the dark (curve *1*) can be divided into the following regions: linear increase ($I \sim U$), quadratic growth ($I \sim U^2$), and sharp buildup ($I \sim U^n$, $n > 2$). We have established that the current generation in the nonlinear region is due to a unipolar carrier injection and the field effect [5]. Under illumination, the whole *I–V* curve is linear; the values of J_2 (light current) are 10^4–10^5 times the values of J_1 (dark current) observed at the same voltage. This indicates that $MnGaInS_4$ is an extremely photosensitive material.

In addition, Fig. 1 presents a family of the *I–U* curves of the same In–$MnGaInS_4$–In structure illuminated at a wavelength of 710 nm and measured at various temperatures (curves *3–11*). As can be seen, the measurements at low temperatures (80–153 K) reveal ohmic behavior at small applied voltages, replaced by the quadratic dependence at higher voltages (curves *3* and *4*). Previously [8], we established that the photoconductivity spectrum of $MnGaInS_4$ single crystals measured at 175 K and above contains a region (640–720 nm) related to the impurity photoconductivity. Therefore, the quadratic behavior observed in the *I–U* curves measured at low temperatures is not caused by the illumination. Here, the mechanism of carrier transfer is related to the unipolar injection observed previously in the dark *I–U* curves of $MnGaInS_4$ [5]. As the sample temperature increases to 212 K and above, the quadratic region disappears and the *I–U* curves become almost linear. The current buildup with the temperature is due to the carrier release from the traps filled under illumination.

Figure 2 shows the temperature dependences of the electric conductivity of $MnGaInS_4$ single crystals measured in the dark (curve *1*) and under IR illumination at λ = 710 nm (curve *2*). As can be seen, the conductivity in a low-temperature region is significantly higher under illumination than in the dark. The temperature dependence of $\log\sigma$ for the illuminated single crystal reveals three regions with different activation energies E = 0.07, 0.20, and 0.46 eV, while the curve measured in the dark shows two such regions with E = 0.46 and 0.67 eV. It should be noted that the levels with E = 0.46 eV were also revealed by data on the temperature dependence of trapping factor $\theta(T)$ [5]. This fact indi-

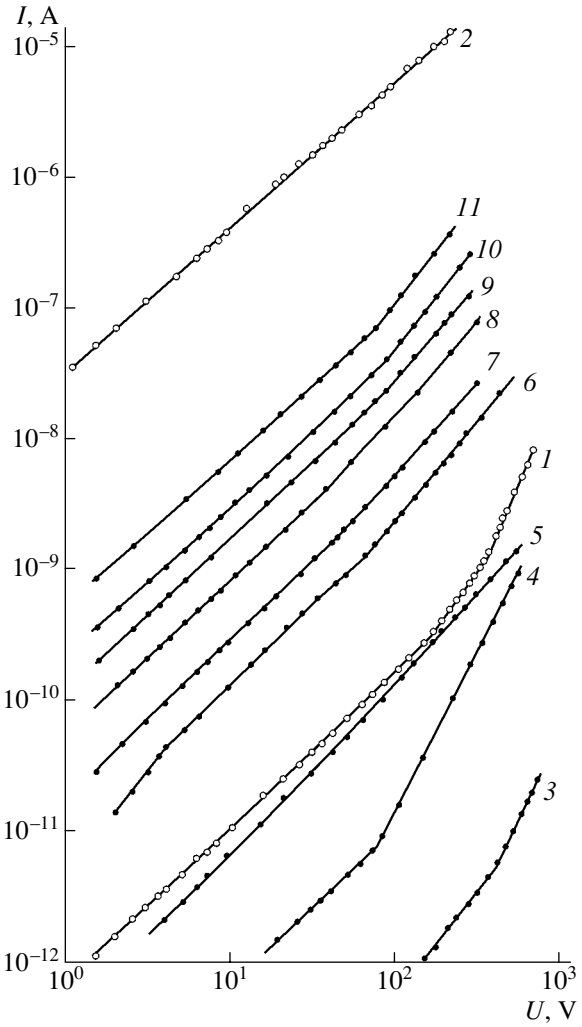

Fig. 1. Typical current–voltage characteristics of an In–$MnGaInS_4$–In sandwich structure measured (curve *1*) at 294 K in the dark, (curve *2*) at 294 K under illumination with a white light at 200 lx, and (curves *3–11*) under IR illumination (λ = 710 nm) at various temperatures T = 80 (*3*), 153 (*4*), 212 (*5*), 291 (*6*), 311 (*7*), 341 (*8*), 359 (*9*), 372 (*10*), and 394 K (*11*).

cates that both the light-induced carrier injection and the high-temperature conductivity behavior in illuminated $MnGaInS_4$ single crystals are related to the same levels.

Thus, the results of our experimental investigation of the effect of illumination on the current–voltage characteristics and the temperature dependence of conductivity of $MnGaInS_4$ single crystals show that the current in a sample under illumination is 10^4–10^5 times the dark value. The light-induced current buildup is due to the carrier release from the traps filled under illumination. The energy positions of levels are determined.

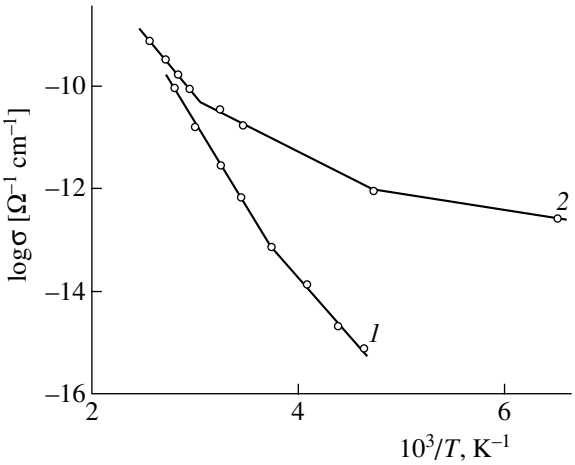

Fig. 2. Temperature dependences of the electric conductivity of a $MnGaInS_4$ single crystal measured (curve *1*) in the dark and (curve *2*) under IR illumination at λ = 710 nm.

REFERENCES

1. T. Kanomata, H. Ido, and T. Kaneko, Jpn. J. Phys. **34**, 554 (1973).
2. R. N. Bekimbetov, Yu. V. Rud', and M. A. Tairov, Fiz. Tverd. Tela (Leningrad) **21**, 1051 (1987) [Sov. Phys. Solid State **21**, 642 (1987)].
3. R. N. Bekimbetov, G. A. Medvedkin, V. D. Prochukhan, *et al.*, Pis'ma Zh. Tekh. Fiz. **13**, 1040 (1987) [Sov. Tech. Phys. Lett. **13**, 434 (1987)].
4. G. K. Averkieva, R. N. Bekimbetov, N. N. Konstantinova, *et al.*, Izv. Akad. Nauk SSSR, Neorg. Mater. **24**, 591 (1988).
5. N. N. Niftiev, A. G. Rustamov, and O. B. Tagiev, Fiz. Tekh. Poluprovodn. (St. Petersburg) **27**, 386 (1993) [Semiconductors **27**, 215 (1993)].
6. N. N. Niftiev, A. G. Rustamov, O. B. Tagiev, *et al.*, Opt. Spektrosk. **75**, 351 (1993) [Opt. Spectrosc. **75**, 206 (1993)].
7. C. Battistoni, L. Gastaldi, S. Mattagno, *et al.*, Solid State Commun. **61**, 43 (1987).
8. N. N. Niftiev, O. B. Tagiev, and G. M. Niftiev, Izv. Ross. Akad. Nauk, Neorg. Mater. **32**, 291 (1996).

Translated by P. Pozdeev

Technical Physics Letters, Vol. 29, No. 5, 2003, pp. 422–425. Translated from Pis'ma v Zhurnal Tekhnicheskoĭ Fiziki, Vol. 29, No. 10, 2003, pp. 54–61.

Diffusion with the Formation and Decay of Immobile Complexes in Solids

R. Sh. Malkovich

Ioffe Physicotechnical Institute, Russian Academy of Sciences, St. Petersburg, 194021 Russia

Received December 23, 2002

Abstract—The concentration profiles of an impurity diffusing in a solid with the formation and decay of immobile complexes are determined. Formulas describing the impurity distribution are obtained by transformation of a solution of the problem of free impurity diffusion under the same initial and boundary conditions. © *2003 MAIK "Nauka/Interperiodica".*

The process of diffusion in solids is frequently accompanied by the formation of complexes between the diffusant (impurity) and various traps (other impurities, defects, etc.) [1]. These traps can be either mobile or immobile.

Kucher [2] studied the linear problem, whereby an impurity and complexes simultaneously diffuse in an unbounded or semibounded medium as described by the system of equations

$$\frac{\partial c_1}{\partial t} = D_1\frac{\partial^2 c_1}{\partial x^2} - k_1c_1 + k_2c_2, \quad (1a)$$

$$\frac{\partial c_2}{\partial t} = D_2\frac{\partial^2 c_2}{\partial x^2} + k_1c_1 - k_2c_2. \quad (1b)$$

Here, c_1 is the free impurity (diffusant) concentration; c_2 is the bound impurity (complex) concentration; D_1 is the diffusion coefficient for the impurity; D_2 is the diffusion coefficient for the complexes; k_1 and k_2 are the probabilities of complex formation and decay per unit time, respectively; x is the coordinate; and t is the time.

The problem of diffusion in a nonlinear region is described by the system of equations

$$\frac{\partial c_1}{\partial t} = D_1\frac{\partial^2 c_1}{\partial x^2} - k_1qc_1 + k_2c_2,$$

$$\frac{\partial c_2}{\partial t} = D_2\frac{\partial^2 c_2}{\partial x^2} + k_1qc_1 - k_2c_2, \quad (2)$$

$$\frac{\partial q}{\partial t} = D_q\frac{\partial^2 q}{\partial x^2} - k_1qc_1 + k_2c_2,$$

where q and D_q are the concentration and the diffusion coefficient of traps, respectively. For immobile complexes ($D_2 = 0$), this problem was solved by the method of sequential intervals [3]. An analytical solution can be obtained in the particular case of immobile traps ($D_q = 0$) using the local equilibrium approximation ($k_1qc_1 = k_2c_2$) [3, 4] or the total binding approximation. In the case of mobile traps, analytical solutions were obtained in the local equilibrium approximation (for weak or strong binding) [5–7]. The process of diffusion with the formation and decay of immobile complexes was studied by Fistul and Sinder [8–10]. Analytical solutions were obtained in some limiting cases (strong and weak binding, close diffusion coefficients, etc.). The analytical description is also possible when the impurity is immobile in the free state ($D_1 = 0$) and is transferred only via diffusion of complexes [11, 12].

This Letter reports on an explicit analytical solution of the linear problem of diffusion in a solid with the formation and decay of immobile complexes. The solution is obtained by transformation of a solution of the problem of free impurity diffusion under the same initial and boundary conditions.

Consider a solution of the system of equations (1) in the case of immobile complexes ($D_2 = 0$), assuming that no complexes were present at the initial time: $c_2(x, 0) = 0$.

The diffusion problem will be solved by method of Laplace transform. Let us determine the concentration profile $c_1(x, t)$ of the free impurity (diffusant), since the distribution of complexes $c_2(x, t)$ can then be found from Eq. (1b). Indeed, for $D_2 = 0$ this equation yields

$$c_2(x, t) = k_1\exp(-k_2t)\int_0^t c_1(x, \tau)\exp(k_2\tau)d\tau. \quad (3)$$

Equation (1a) transformed via

$$v(x) = \int_0^\infty \exp(-pt)c_1(x, t)dt \quad (4)$$

acquires the form

$$\frac{d^2v}{dx^2} - \frac{1}{D}sv + \frac{c_1(x,0)}{D} = 0, \quad (5)$$

where $c_1(x, 0)$ is the initial concentration distribution of the free impurity, $D = D_1$, and

$$s = p + k_1 - \frac{k_1k_2}{p + k_2}. \quad (6)$$

It can be readily shown that the solution of Eq. (5) for a finite body ($0 \le x \le l$) with absorbing [$c_1(0, t) = c_1(l, t) = 0$, $t > 0$] or impermeable [$\frac{\partial c_1}{\partial x}(0, t) = \frac{\partial c_1}{\partial x}(l, t) = 0$, $t > 0$] boundaries is as follows:

$$v(x) = \frac{1}{2\sqrt{sD}\sinh\left(\sqrt{\frac{s}{D}}l\right)} \times \left\{\int_0^x c_1(\xi, 0)\cosh\left[\sqrt{\frac{s}{D}}(l - x + \xi)\right]d\xi + \int_x^l c_1(\xi, 0)\cosh\left[\sqrt{\frac{s}{D}}(l + x - \xi)\right]d\xi \mp \int_0^l c_1(\xi, 0)\cosh\left[\sqrt{\frac{s}{D}}(l - x - \xi)\right]d\xi\right\}. \quad (7)$$

Here, the upper and lower signs correspond to the cases of absorbing and impermeable boundaries, respectively.

Expression (7) shows that the transform $v(x)$ is a function of the quantity s given by formula (6). As can be readily verified, this statement is also valid for a semibounded medium ($0 \le x \le \infty$) with either absorbing [$c_1(0, t) = 0$, $t > 0$] or impermeable [$\frac{\partial c_1}{\partial x}(0, t) = 0$, $t > 0$] boundaries, as well as for the unbounded medium ($-\infty \le x \le \infty$). This circumstance allows us to obtain a solution for the problem of diffusion with the formation and decay of complexes, using a solution of the problem of free impurity diffusion under the same initial and boundary conditions.

Let us determine the impurity concentration $c_1(x, t)$ using the transform $v(s, x)$: $v(s, x) = v(x)$ defined by Eq. (4). Taking the Laplace transform

$$v(p, x) = \int_0^\infty \exp(-p\tau)c(x, \tau)dt, \quad (8)$$

replacing p by s, and substituting expression (6), we obtain

$$v(s, x) = \int_0^\infty \exp[-(p + k_1)\tau]\exp\left(\frac{k_1k_2\tau}{p + k_2}\right)c(x, \tau)d\tau. \quad (9)$$

Using the relation [13]

$$\int_0^\infty \exp[-(p + a)\eta]I_1\left(2\sqrt{\frac{\eta}{b}}\right)\frac{d\eta}{\sqrt{a\eta}} = \exp\left(\frac{1}{b(p + a)}\right) - 1,$$

where I_1 is the modified Bessel function of the first kind [14], Eq. (9) can be rewritten as

$$v(s, x) = \int_0^\infty \exp[-(p + k_1)\tau]\left\{1 + \sqrt{k_1k_2}\int_0^\infty \exp[-(p + k_2)\tau] \times I_1 2\sqrt{k_1k_2\eta\tau}\sqrt{\frac{\tau}{\eta}}d\eta\right\}c(x, \tau)d\tau.$$

Putting $\eta = t - \tau$ in the inner integrand, we obtain

$$v(s, x) = \int_0^\infty \exp[-(p + k_1)\tau]c(x, \tau)d\tau + \sqrt{k_1k_2}\int_0^\infty \exp[-(p + k_1)\tau]\sqrt{\tau}\int_\tau^\infty \exp[-(p + k_2)(k - \tau)] \times I_1(2\sqrt{k_1k_2\tau(t - \tau)})\frac{dt}{\sqrt{t - \tau}}c(x, \tau)d\tau. \quad (10)$$

Changing the order of integration and replacing τ by t in the first integrand of Eq. (10), we obtain a transform of type (4) in which the original function $c_1(x, t)$ is given by the expression

$$c_1(x, t) = \exp(-k_1t)c(x, t) + \sqrt{k_1k_2}\exp(-k_2t) \times \int_0^t \exp[-(k_1 - k_2)\tau]I_1(2\sqrt{k_1k_2\tau(t - \tau)})\sqrt{\frac{\tau}{t - \tau}}c(x, \tau)d\tau. \quad (11)$$

Thus, the function $c(x, t)$ is an original for the transform $v(p, x)$ defined by Eq. (8), and the function $c_1(x, t)$ determined by Eq. (11) is an original for the transform $v(s, x) = v(x)$ given by Eq. (4). Therefore, once the concentration profile $c(x, t)$ for the free impurity diffusion is known, the distribution of the same impurity $c_1(x, t)$ for the diffusion with the formation and decay of immobile complexes under the same initial and boundary conditions can be determined using expression (11).

Consider an example of outdiffusion from a homogeneously doped semibounded medium with the initial condition $c_1(x, 0) = c(x, 0) = c_0$ and the absorbing

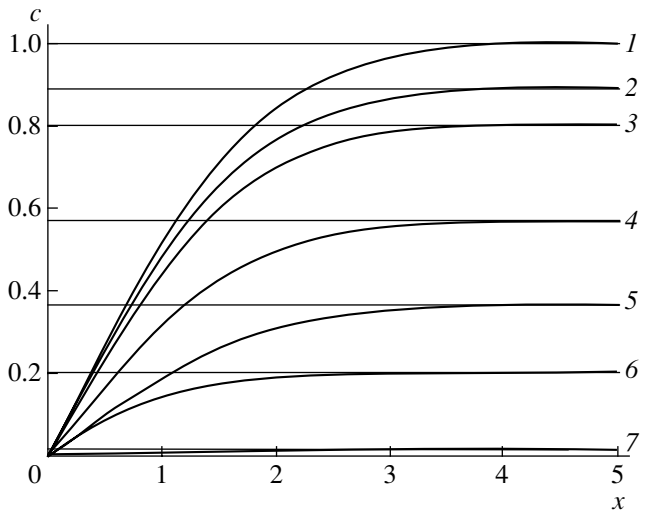

Fig. 1. Impurity depth–concentration profiles in the case of outdiffusion from an initially homogeneously doped medium [$c_1(x, 0) = 1$] with absorbing boundary, accompanied by the formation and decay of immobile complexes ($D = 1$, $t = 1$): (*1*) free diffusion ($k_1 = 0$); (*2*) $k_1 = 1$, $k_2 = 8$; (*3*) $k_1 = 1$, $k_2 = 4$; (*4*) $k_1 = 1$, $k_2 = 1$; (*5*) $k_1 = 1$, $k_2 = 0$; (*6*) $k_1 = 4$, $k_2 = 1$; (*7*) $k_1 = 4$, $k_2 = 0$.

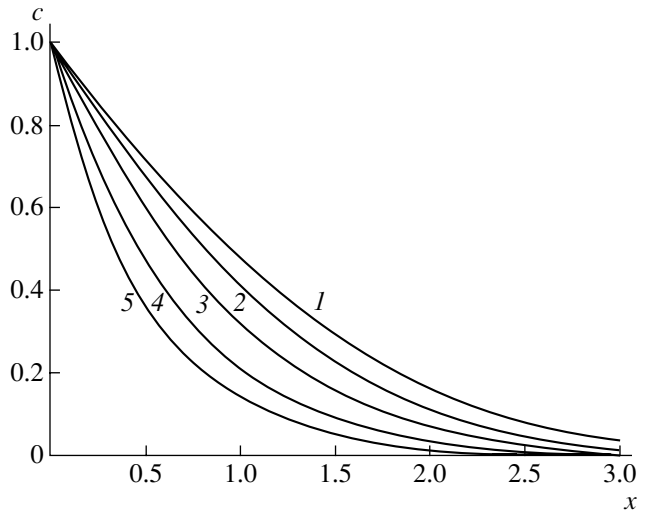

Fig. 2. Impurity depth–concentration profiles in the case of diffusion at a constant surface concentration [$c_1(0, t) = c_0 = 1$, $t > 0$] into an initially impurity-free medium [$c_1(x, 0) = 0$], accompanied by the formation and decay of immobile complexes ($D = 1$, $t = 1$): (*1*) free diffusion ($k_1 = 0$); (*2*) $k_1 = 1$, $k_2 = 12$; (*3*) $k_1 = 1$, $k_2 = 4$; (*4*) $k_1 = 1$, $k_2 = 1$; (*5*) $k_1 = 4$, $k_2 = 12$.

boundary. In the case of free diffusion, the impurity profile at an arbitrary time is described by the formula [15]

$$c(x, t) = c_0 \mathrm{erf}\frac{x}{2\sqrt{Dt}}.$$

Substituting this expression into formula (11), we obtain the required expression for the impurity profile $c_1(x, t)$ in the case of diffusion with the formation and decay of immobile complexes. The curves of $c_1(x, t)$ calculated for several sets of coefficients k_1 and k_2 are presented in Fig. 1.

Now let us consider the practically important case of diffusion into a semibounded medium initially free of the impurity, at a constant surface density of the diffusant: $c_1(0, t) = c_0 = \text{const}$, $t > 0$. In this case, a transform of the impurity profile for diffusion with the formation and decay of immobile complexes is as follows:

$$v(x) = \frac{c_0}{p}\exp\left(-\sqrt{\frac{s}{D}}x\right). \quad (12)$$

Note that this transform is a function of both s and p, rather than of s alone. As can be readily seen, the function $c_1(x, t)$ can be determined, according to the theorem about integration of the original, from the relation

$$c_1(x, t) = \int_0^t \tilde{c}_1(x, \tau)d\tau, \quad (13)$$

where $\tilde{c}_1(x, \tau)$ is an original function for the transform

$$v^*(s, x) = c_0\exp\left(-\sqrt{\frac{s}{D}}x\right).$$

In the case under consideration, an original function for the transform

$$v^*(p, x) = c_0\exp\left(-\sqrt{\frac{p}{D}}x\right)$$

can be expressed as [15]

$$\tilde{c}(x, t) = \frac{c_0 x}{2t\sqrt{\pi Dt}}\left(-\frac{x^2}{4Dt}\right).$$

Substituting this function $\tilde{c}(x, t)$ into formula (11), we determine $\tilde{c}_1(x, t)$. Then, upon calculating the integral in (13), we obtain the desired impurity concentration profile $c_1(x, t)$. Figure 2 shows the curves of $c_1(x, t)$ calculated for several sets of coefficients k_1 and k_2.

REFERENCES

1. *Atomic Diffusion in Semiconductors*, Ed. by D. Shaw (Plenum, London, 1973; Mir, Moscow, 1975).
2. T. I. Kucher, Fiz. Tverd. Tela (Leningrad) **6**, 801 (1964) [Sov. Phys. Solid State **6**, 623 (1964)].
3. R. Sh. Malkovich and V. A. Pokoeva, Phys. Status Solidi B **82**, 421 (1977).

4. H. Reiss, C. Fuller, and F. Morin, Bell Syst. Tech. J. **35**, 535 (1956).
5. V. V. Vas'kin and V. A. Uskov, Fiz. Tverd. Tela (Leningrad) **10**, 1239 (1968) [Sov. Phys. Solid State **10**, 985 (1968)].
6. V. V. Vas'kin and V. A. Uskov, Fiz. Tverd. Tela (Leningrad) **11**, 1763 (1969) [Sov. Phys. Solid State **11**, 1429 (1969)].
7. V. I. Fistul', M. I. Sinder, and D. M. Reĭn, Fiz. Tekh. Poluprovodn. (Leningrad) **15**, 1867 (1981) [Sov. Phys. Semicond. **15**, 1088 (1981)].
8. V. I. Fistul' and M. I. Sinder, Élektron. Tekh., Ser. Mater. **8** (157), 35 (1981).
9. V. I. Fistul' and M. I. Sinder, Fiz. Tekh. Poluprovodn. (Leningrad) **17**, 1995 (1983) [Sov. Phys. Semicond. **17**, 1273 (1983)].
10. V. I. Fistul' and M. I. Sinder, Fiz. Tekh. Poluprovodn. (Leningrad) **17**, 2003 (1983) [Sov. Phys. Semicond. **17**, 1278 (1983)].
11. A. Lidiard, in *Handbuch der Physik* (Springer-Verlag, Berlin, 1957), Vol. 20.
12. J. R. Andersen and J. F. Gibbons, Appl. Phys. Lett. **28**, 184 (1976).
13. V. A. Ditkin and A. P. Prudnikov, *A Handbook on Operational Calculus* (Vysshaya Shkola, Moscow, 1965).
14. *Handbook of Mathematical Functions*, Ed. by M. Abramowitz and I. Stegun (Nat. Bureau of Standards, 1964; Nauka, Moscow, 1979).
15. J. Grank, *The Mathematics of Diffusion* (Clarendon Press, Oxford, 1956).

Translated by P. Pozdeev

Technical Physics Letters, Vol. 29, No. 5, 2003, pp. 426–429. Translated from Pis'ma v Zhurnal Tekhnicheskoĭ Fiziki, Vol. 29, No. 10, 2003, pp. 62–69.

Extracting Surface Impedance Model Parameters of a High-Temperature Superconductor from Experimental Characteristics of a Microstrip Resonator

P. N. Yudin and I. B. Vendik

St. Petersburg State Electrotechnical University, St. Petersburg, Russia

e-mail: mwlab@eltech.ru

Received December 24, 2002

Abstract—We describe a method for extracting the model parameters of a high-temperature superconductor (HTSC) film from experimental resonance characteristics of a microstrip resonator. The method is based on a correct phenomenological model of the surface impedance of an HTSC film and the exact calculation of the microstrip resonator characteristics. The procedure of extracting the model parameters from experimental data is realized by using a genetic algorithm. Based on the models described, a special program implementing this mathematical algorithm was written, which allows the HTSC model parameters to be determined from experimental data. © *2003 MAIK "Nauka/Interperiodica".*

Introduction. High-temperature superconductor (HTSC) films possessing extremely low surface impedance are widely used in microwave devices, in particular, in ultra-narrowband filters. Designing such filters is based on an analysis of the corresponding planar microwave structures using correct models of planar HTSC transmission lines with allowance for the known characteristics of superconducting films. Use of a model implies knowledge of the model characteristics, which are considered as fitting parameters. These parameters have to be determined from experimental data, for example, on the resonance characteristics of planar resonators employing films of the same type as that to be used in a designed filter.

Below, we will consider the relation between the characteristics of HTSC microstrip resonators and the parameters of a phenomenological model of the surface impedance of an HTSC film. Based on this relation, a procedure has been developed for extracting the model parameters from experimental characteristics by means of a genetic algorithm.

The surface impedance of an HTSC film: a phenomenological model and its relation to the characteristics of a microstrip resonator. Recently [1–4], we developed a phenomenological model of the surface impedance of an HTSC film. According to this model, the surface impedance is described by the function

$$Z_{\text{sur}}^0 = \left(\frac{i\omega\mu_0}{\sigma_1 - i\sigma_2}\right)^{1/2}, \quad (1)$$

where

$$\sigma_1(t) = \sigma_n(1)\left\lfloor t^{\gamma-1} + \alpha(1-t^{\gamma})\right\rfloor, \quad (2)$$

$$\sigma_2 = \frac{1}{\omega\mu_0\lambda_L^2}, \quad (3)$$

$$[\lambda_L(0)/\lambda_L(t)]^2 = 1 - t^{\gamma}. \quad (4)$$

In Eqs. (1)–(4), $\omega = 2\pi f$, f is the frequency, μ_0 is the magnetic permeability of vacuum, $\sigma_n(1)$ is the conductivity of normal charge carriers at $T = T_c$; $t = T/T_c$, T is the current absolute temperature, λ_L is the London penetration depth, $\lambda_L(0) = 0.13 \times 10^{-6}\exp(1.27 - 0.5\gamma)$ [m], α is the parameter of residual resistance, and γ is an empirical parameter extracting the temperature dependence of the London penetration depth. The model employs four fitting parameters: T_c, $\sigma_n(1)$, α, and γ.

In the case of film structures, one has to take into account the reflection of electromagnetic waves from both boundaries of the film and calculate the surface impedance by the formula

$$Z_{\text{sur}} = R_{\text{sur}} + iX_{\text{sur}} = \frac{Z_{\text{sur}}^0}{\tanh(ikd)}, \quad (5)$$

$$k(t) = \sqrt{-i\omega\mu_0\sigma_1(t) - \frac{1}{\lambda_L^2(t)}}. \quad (6)$$

HTSC transmission lines are characterized by the characteristic impedance Z_0 and the propagation parameters, including the wavenumber β and the attenuation coefficient α_{at}. The propagation parameters

1063-7850/03/2905-0426$24.00 © 2003 MAIK "Nauka/Interperiodica"

strongly depend on the HTSC line characteristics. The wavenumber is calculated by the formula

$$\beta = \frac{\omega\sqrt{\varepsilon_{\text{eff}}}}{c}, \tag{7}$$

$$\varepsilon_{\text{eff}} = \varepsilon^0_{\text{eff}}(1 + L_k/L_1), \tag{8}$$

$$L_k = \frac{X_{\text{sur}}}{\omega\mu_0} = \mu_0\lambda_L^2/(dw_{\text{eff}}), \tag{9}$$

where ε_{eff} is the effective permittivity of the microstrip line, $\varepsilon^0_{\text{eff}}$ is the same without HTSC contribution, c is the light speed in vacuum, L_k is the kinetic inductance of HTSC, L_1 is the inductance per unit length of the transmission line, w_{eff} is the effective width of the transmission line with allowance for an inhomogeneous distribution of the surface current density across the conductor [4, 5]. The attenuation coefficient is determined by the expression

$$\alpha_{at} = \frac{R_{\text{sur}}}{2Z_0 w_{\text{eff}}}. \tag{10}$$

An HTSC line section used as a resonator is connected to external circuit via coupling elements. For calculating the characteristics of an HTSC resonator employing a planar line (microstrip or coplanar), we have developed a special program package ensuring computation of the scattering matrix S with allowance of the HTSC characteristics [6]. The program employs a quasistatic method for the analysis of microwave structures in a given range of frequencies. Using the program, the resonator characteristics S can be calculated in this frequency range as functions of the temperature and the model parameters in terms of Eqs. (1)–(10).

Extracting model parameters from experimental characteristics of an HTSC resonator. The model parameters are extracted using an optimization procedure employing a genetic algorithm developed by Goldberg [7] for description of the evolution of biological objects. This genetic algorithm allows the global minimum of a criterion function to be determined and is effective from the standpoint of required computational facilities.

In constructing a symbolic model of the genetic algorithm, the set of admissible solutions is represented by a finite population of solution. Each individual in a given population possesses a certain degree of adaptation with respect to the environment. The search for the optimum solution is represented by a model evolution process aimed at finding an individual (or a set of such individuals) characterized by maximum adaptation, that is, corresponding to the optimum requirements (parameters).

Each individual is represented by a combination of genes (bit sequences of a liven length) called chromosomes. The number of genes in a chromosome corresponds to the dimension of a given problem; each gene is used to code a small interval of values of a certain model parameter. This way of coding essentially corresponds to a subdivision of the space of parameters into hypercubes representing unique bit combinations in a chromosome (genotype).

In the problem of extracting the model HTSC parameters, each gene represents a binary code of one of the parameters (d, T_c, σ_N, α, γ, ε) to be extracted from experimental data, and a chromosome is a set of such genes. The maximum number of genes in a chromosome for the problem under consideration is six (which corresponds to the case of extraction of the maximum number of model parameters).

Each solution of the genetic algorithm has the following structure: (i) A point $\mathbf{X}$ in the space of parameters (phenotype): $\mathbf{X} = (d, T_c, \sigma_N, \alpha, \gamma, \varepsilon)$ belongs to $\mathbf{D}$ from $\mathbf{R}^N$.

(ii) A binary sequence $\mathbf{s}$ of a fixed length, uniquely extracting the hypercube of subdivision in the space of parameters (genotype): $\mathbf{s} = (b_1, b_2, \ldots, b_l)$ belongs to S, where S is the space of representations (binary sequences of length l).

(iii) A scalar quantity m, corresponding to the value of the criterion function at the point $\mathbf{X}$ (adaptation): $m = f(\mathbf{X})$.

In terms of the theory of genetic algorithms, this structure is called an individual. A set of individuals is referred to as a population.

In the theory of evolution, an important role belongs to the mechanism by which the characters of parent individuals are inherited by offspring. In genetic algorithms, this heredity is provided by a special *crossover* (or *crossing-over*) operator, which acts as follows: (i) selects two individuals (parents) from a population; (ii) selects (usually randomly) a step to crossover; and (iii) determines offspring as concatenants of parts of the first and second parents. Another genetic operator is intended to maintain the diversity of individuals in a population. This *mutation* operator produces inversion of every bit in a chromosome at a certain probability. The two genetic operators introduced above are, in principle, sufficient to provide for the functioning of a genetic algorithm. In practice, however, some additional operators and/or their modifications are employed as well.

A criterion function used to determine the model parameters has the following form:

$$Q = Q(\mathbf{X}) = \sum_{k=1}^{n}\left(\frac{(S11_{\text{exp}} - S11_{\text{cal}}(\mathbf{X}_k))^2}{S11^2_{\text{exp}}}\right) + \sum_{k=1}^{n}\left(\frac{(S12_{\text{exp}} - S12_{\text{cal}}(\mathbf{X}_k))^2}{S12^2_{\text{exp}}}\right), \tag{11}$$

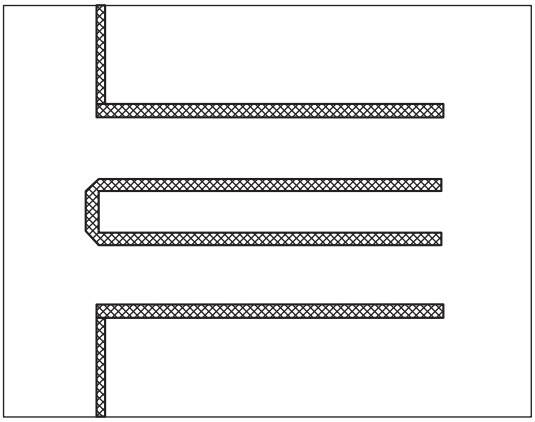

Fig. 1. Schematic diagram showing topology of the YBCO microstrip resonator.

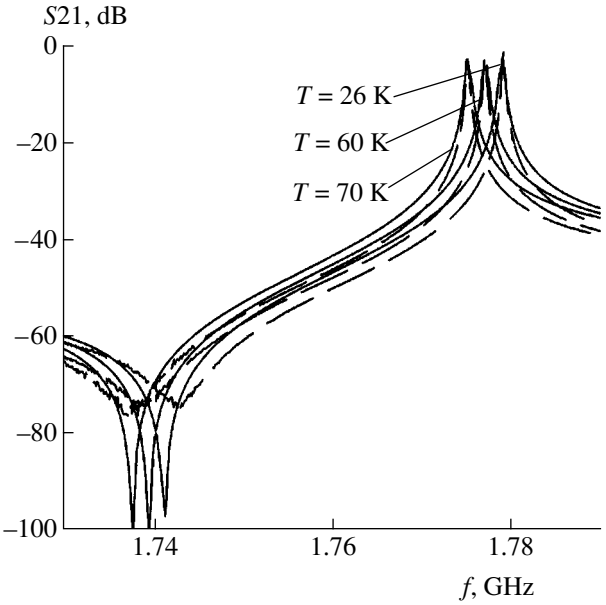

Fig. 2. A comparison of (solid curves) calculated and (dashed curves) measured frequency characteristics of a microstrip resonator.

where $S11_{exp}$, $S11_{cal}$, $S12_{exp}$, and $S12_{cal}$ are the experimental and calculated scattering parameters of a resonator ($S11$ being the reflection coefficient and $S12$, the transmission coefficient), n is the number of the experimental data, and $\mathbf{X} = (d, T_c, \sigma_N, \alpha, \gamma, \varepsilon)$ is the vector of optimization parameters. The set of fitting (optimization) parameters includes the film thickness d and the substrate permittivity (ε) because these values are usually unknown.

The process of optimization is aimed at finding a minimum of the criterion function,

$$\min_{x \in D} \; Q = Q(\mathbf{X}^*) = Q^*, \qquad (12)$$

under certain limiting conditions $x_j^- \le x_j \le x_j^+$ ($j = 1, 2, \ldots, N$). Here, $\mathbf{X}^* = (x_1^*, x_2^*, \ldots, x_N^*)$ is the vector of optimum parameters corresponding to a minimum of the criterion function $Q(\mathbf{X})$ and N is the number of optimization parameters.

The problem of finding the extremum of the criterion function $Q(\mathbf{X})$ is solved by the genetic algorithm using the following procedure:

1. Initialization of the starting population.

2. Calculation of the benefit function for individuals of the population.

3. Selection of individuals from the current population.

4. Application of the crossover and mutation operators for creating offspring.

5. Calculation of the benefit function for individuals of the offspring.

6. Selection of individuals for the new population.

7. Repetition of pp. 3–6 until extracting a minimum of the criterion function $Q(\mathbf{X})$ and the corresponding vector of parameters $\mathbf{X}$ at a preset accuracy.

Application of the method of extracting model parameters to an YBCO microstrip resonator. Consider a hairpin microstrip resonator representing an YBCO film on a $LaAlO_3$ substrate with a thickness of $d = 450$ nm (Fig. 1) [8, 9]. The resonator is a planar multistrip structure that can be modeled using the aforementioned program [6] taking into account coupling between all lines. The model parameters were determined using a set of experimental data obtained at various temperatures.

The problem was solved under the following limitations posed on the model parameters: $50\ \text{K} \le T_c \le 100\ \text{K}$; $2 \le \gamma \le 4$; $1 \times 10^6\ (\Omega\ \text{m})^{-1} \le \sigma_n(1) \le 3 \times 10^6\ (\Omega\ \text{m})^{-1}$; $5 \le \alpha \le 20$; the number of chromosomes in the population, 100. It was found that the global minimum of the criterion function (11) is provided by the following set of parameters: $T_c = 85$ K; $\gamma = 2.3$; $\sigma_n(1) = 2.5 \times 10^6\ (\Omega\ \text{m})^{-1}$, $\alpha = 13$; permittivity of the substrate, $\varepsilon = 23.63$. The computational time for Pentium IV (1.7 GHz; 256 MB RAM) was 30 s.

The values of parameters determined for the surface impedance model were used to calculate the resonance characteristics of HTSC resonators at various temperatures. Figure 2 presents the results of these calculations in comparison to the experimental characteristics. As can be seen, the proposed method ensures a good coincidence of the calculated and measured characteristics.

Conclusion. We proposed a method for extracting parameters of the HTSC surface impedance model from experimental characteristics of the HTSC microstrip resonators. The experimental characteristics coincide with those calculated using the model parameters extracted using a specially developed genetic algorithm. This is evidence of the correctness of the model and the applicability of the procedure used for extracting the model parameters.

REFERENCES

1. I. B. Vendik, Supercond. Sci. Technol. **13**, 974 (2000).
2. O. G. Vendik, I. B. Vendik, and D. I. Kaparkov, IEEE Trans. Microwave Theory Tech. **46**, 469 (1998).
3. I. B. Vendik, IEEE Trans. Appl. Supercond. **11**, 3545 (2001).
4. I. B. Vendik, O. G. Vendik, and D. I. Kaparkov, in *High-Temperature Superconducting Devices for Microwave Signal Processing. Part 2. Superconducting Microwave Circuits* (Skladen, St. Petersburg, 1997).
5. I. B. Vendik, M. N. Gubina, A. N. Deleniv, and D. V. Kholodnyak, Zh. Tekh. Fiz. **67** (2), 83 (1997) [Tech. Phys. **42**, 196 (1997)].
6. I. B. Vendik, O. G. Vendik, A. N. Deleniv, *et al.*, IEEE Trans. Microwave Theory Tech. **48**, 1247 (2000).
7. D. Goldberg, *Genetic Algorithms in Search Optimization and Machine Learning* (Addison-Wesley, New York, 1989).
8. H. T. Kim, B.-C. Min, Y. H. Choi, *et al.*, IEEE Trans. Appl. Supercond. **9**, 3909 (1999).
9. A. N. Deleniv, D. Kholodniak, A. Lapshin, *et al.*, Supercond. Sci. Technol. **13**, 1419 (2000).

Translated by P. Pozdeev

Technical Physics Letters, Vol. 29, No. 5, 2003, pp. 430–432. Translated from Pis'ma v Zhurnal Tekhnicheskoĭ Fiziki, Vol. 29, No. 10, 2003, pp. 70–76.

On the Possibility of Determining Internal Wave Characteristics from the Ray Arrival Time Distribution in an Underwater Sound Channel under Conditions of Ray Chaos

D. V. Makarov, M. Yu. Uleysky, and S. V. Prants*

Il'ichev Pacific Oceanological Institute, Far East Division, Russian Academy of Sciences, Vladivostok, Russia

** e-mail: prants@poi.dvo.ru*

Received December 25, 2002

Abstract—We describe the simplest mechanism of cluster structure formation in the timefront of an acoustic signal propagating in a submerged channel under ray chaos conditions. It is shown that this cluster structure is related to the phase space structure. This relation allows, in principle, the characteristics of an inhomogeneous medium to be determined from the timefront shape parameters. As an example, the period of inhomogeneity is calculated for a periodic perturbation in the sound velocity caused by an internal wave propagation. © *2003 MAIK "Nauka/Interperiodica".*

Methods of the acoustic tomography of the ocean are used for the remote sensing of dynamics and structure of water bodies, for determining their hydrodynamic characteristics, and for studying their spatiotemporal variations on a real time scale [1, 2]. When the acoustic waves propagate over long distances, an effective means of monitoring of the medium is provided by an analysis of the signal arrival times. However, extensive theoretical and numerical investigations in the past decade showed that longitudinal variations of the sound velocity, caused by the presence of internal waves or mesoscale structures, lead to chaotization of the signal arrival time pattern even for absolutely deterministic (in the simplest case, periodic) variations. In the approximation of geometric acoustics, this implies the establishment of ray chaos, whereby the ray trajectories are exponentially sensitive with respect to small perturbations in the initial conditions (ray source depth and emission angle). This behavior is typical in the case of nonlinear equations of motion in Hamilton's form.

Smearing of the timefront of an acoustic signal under the conditions of ray chaos is one of the main difficulties encountered in remote sensing of the ocean. However, it was established [3, 4] that rays exhibit grouping with respect to their arrival times, as manifested by the so-called cluster formation. Each cluster has a characteristic interval of arrival times, which corresponds to a certain interval of the ray action variable. This implies that clusterization takes place in the phase space of the system as well. Using the concept of cluster formation, it is possible to explain the stability of the initial part of a received signal. Discovered experimentally, this effect seems to be rather unexpected from the standpoint of the theory of dynamic chaos.

This paper considers two models of realistic sound velocity profiles and periodic perturbations. Using these examples, we will describe a mechanism of cluster formation based on the concept of phase space structurization under the action of a sound velocity perturbation. The existence of a relationship between the timefront structure and the phase space structure allows us, in the given particular case, to determine the perturbation period from a distribution of the ray arrival times.

Consider a two-dimensional model of deep ocean, comprising a characteristic sound velocity profile $c(z)$, which is assumed to be independent of the current longitudinal ray coordinate r, and a small additive $\delta c(z, r)$ (dependent on both ray coordinates). In the paraxial approximation (i.e., at small grazing angles), the propagation of acoustic rays is described by the Hamiltonian

$$H = \frac{1}{2}p^2 + \frac{\Delta c(z)}{c_0} + \frac{\delta c(z, r)}{c_0} - 1, \qquad (1)$$

where $p = dz/dr = \tan\phi$, z is the depth, ϕ is the ray grazing angle, c_0 is the sound velocity at a certain depth, and $\Delta c(z) = c(z) - c_0$. The trajectory of a ray in an underwater sound channel is determined by the Hamilton equations $dz/dr = \partial H/\partial p$, $dp/dr = -\partial H/\partial z$. As a result of refraction, the ray trajectory becomes periodic with a spatial cycle length of $D = 2\pi dI/dH$, where $I = \frac{1}{2\pi}\oint p\,dz$ is the action variable. The time of the ray arrival at a point

with the coordinate R in a homogeneous waveguide is calculated (for a sufficiently large pathlength, $R/D \gg 1$) using the formula

$$t = \frac{R}{c_0}\left[2\pi\frac{I(D)}{D} - H(D)\right]. \quad (2)$$

A point source can be represented (in the paraxial approximation) as

$$\rho(t, R) = F(t, R)\frac{dp_0(t)}{dt}. \quad (3)$$

Here, $F(t, R)$ is a function describing the effect of a spatial inhomogeneity of the sound velocity on the distribution of rays with respect to the arrival times. The shape of this function is determined by the structure of the phase space of a perturbed system. In the particular case of a periodic spatial inhomogeneity, the phase space contains zones of stability corresponding to so-called "islands." The presence of islands is related to a nonlinear resonance [5, 6] determined by the condition $lD_{\text{res}} = m\lambda$, where l and m are some integers. The rays belonging to an island are localized inside it, so that $\lim_{R\to\infty}\overline{D}(R) = D_{\text{res}}$, where the upper bar denotes averaging with respect to r. Accordingly, the arrival times of such rays obey the condition $\lim_{R\to\infty} t(R) = t_{\text{res}}$, where $t_{\text{res}} = t(D_{\text{res}})$ is determined by formula (2). If the size of an island is sufficiently large, the rays belonging to this island form a peak of the $F(t, R)$ function at $t = t_{\text{res}}$. There can be several such peaks, with the greater amplitudes corresponding to resonances with small m at $l = 1$. Thus, if the observed pattern exhibits at least two distinct peaks of the function $F(t, R)$ with close amplitudes, we can determine the period of inhomogeneity as $\lambda \simeq D_{\text{res}}(t_1) - D_{\text{res}}(t_2)$ by calculating D_{res} for each peak using relation (2) and taking into account the resonance condition.

Let us consider an unperturbed sound velocity profile with a periodic perturbation recently introduced in [6]:

$$c(z, r) = c_0\left[1 - \frac{\beta^2}{2}(1 - e^{-az})(e^{-az} - \gamma) + \mu\frac{z}{B}e^{-2z/B}\cos\frac{2\pi r}{\lambda}\right], \quad 0 \le z \le h, \quad (4)$$

where $\gamma = \exp(-ah)$, h is the lower boundary of an underwater sound channel, and λ is the period of inhomogeneity. Numerical calculations were performed for the following set of parameters: $c_0 = 1500$ m/s; $a = 1$ km^{-1}; $h = 2.5$ km; $\beta = 0.3$; $\lambda = 10$ km; $\mu = 0.0025$; and $B = 1$ km. In the absence of perturbations ($\mu = 0$), the ray cycle length (in kilometers) for the profile (4) is given by the formula

$$D(t) = \frac{2\pi}{a}\left(\beta\frac{1+\gamma}{2} - \sqrt{\frac{\beta^2}{4}(1-\gamma)^2 + 2 - \frac{2c_0 t}{R}}\right)^{-1}, \quad (5)$$

where a positive value of the root is employed.

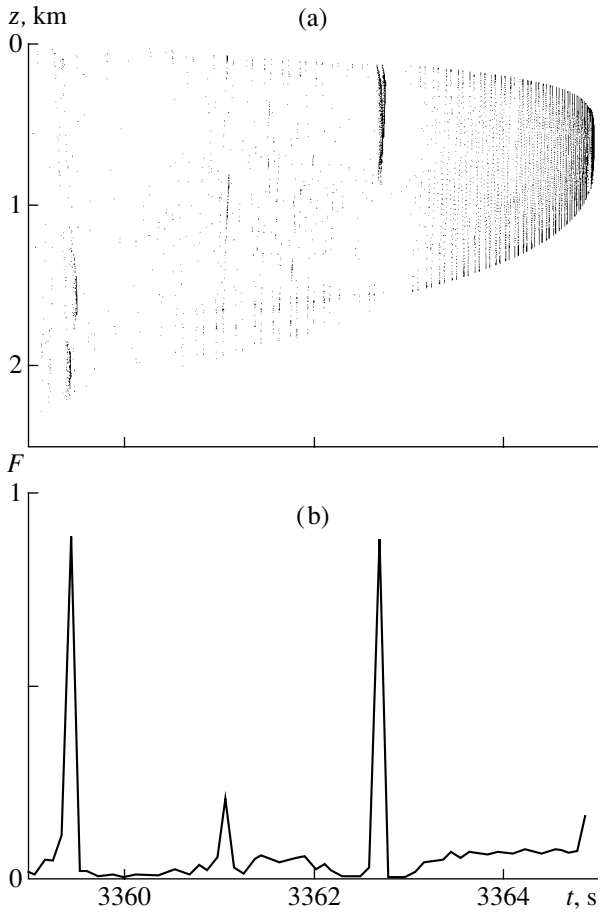

Fig. 1. A model of ray chaos with the sound velocity profile (4): (a) the timefront at a distance of $R = 5000$ km from the source; (b) the corresponding normalized function of the ray arrival times.

Figure 1 shows the timefront and the corresponding function $F(t, R)$ calculated for the model profile (4) with $R = 5000$ km. Local accumulation of the points, observed at $t_1 \simeq 3359.5$ s and $t_2 \simeq 3362.7$ s (Fig. 1a), corresponds to two peaks of the function $F(t, R)$ (Fig. 1b). Based on these data, we obtain for the period of inhomogeneity $\lambda \simeq 10.1$ km, so that the relative error is on the order of one percent. Note that Fig. 1b displays an additional smaller peak corresponding to $D_{\text{res}} \simeq 55$ km (a resonance with $l = 2$, $m = 11$).

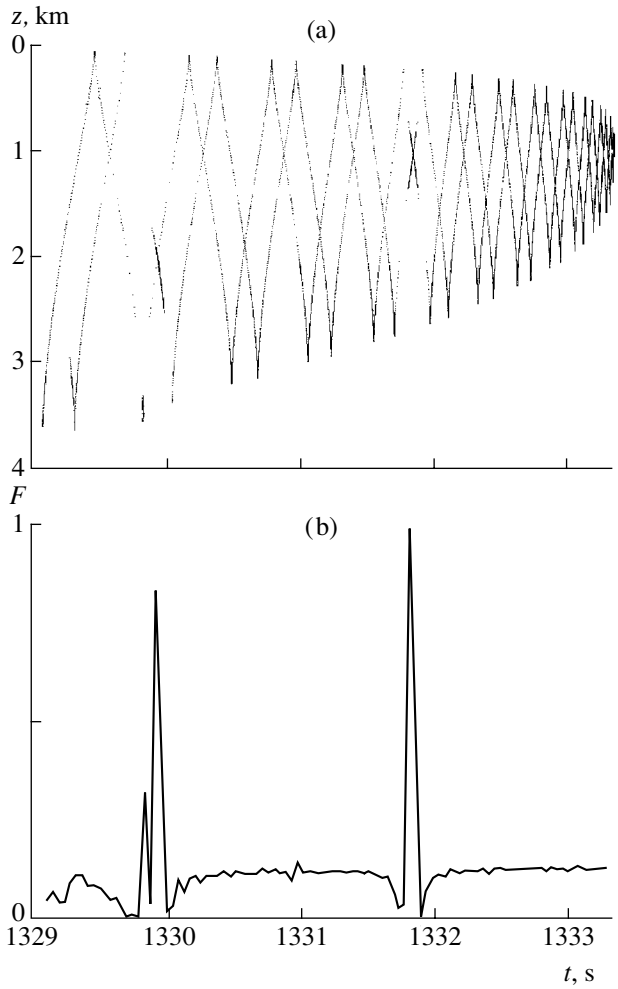

Fig. 2. A model of ray chaos with the Munk sound velocity profile: (a) the timefront at a distance of $R = 2000$ km from the source; (b) the corresponding normalized function of the ray arrival times.

Let us also consider a model of the canonical submerged Munk channel with a periodic perturbation:

$$c(z, r) = c_0\left[1 + \epsilon(\eta - 1 + e^{-\eta}) + \mu\frac{z}{B}e^{-2z/B}\cos\frac{2\pi r}{\lambda}\right], \quad (6)$$

where $\epsilon = 0.0057$ is a constant factor and η is a dimensionless depth defined as $\eta = 2(z - z_a)/B$, where $z_a = 1$ km. We have numerically calculated the timefront at a distance of $R = 2000$ km for $\lambda = 5$ km (all other parameters are the same as above). The results presented in Fig. 2 reveal two distinct peaks of the function $F(t, R)$. The left peak at $t_1 = 1329.9$ s corresponds to $D_{\text{res}}(t_1) \simeq 55$ km (the relation between D and t for the Munk profile was obtained in the numerical form using formula (2)), while the right peak at $t_2 = 1331.8$ s corresponds to $D_{\text{res}}(t_2) \simeq 50$ km. Thus, the difference between D_{res} for the Munk profile is also equal to the spatial period of inhomogeneity.

Thus, we have described the simplest mechanism of the formation of ray clusters related to the presence of localization zones in the phase space of the system under consideration. Since the phase space structure (in particular, the arrangement of localization zones) is directly determined by the properties of a perturbation, there appears a principal possibility to determine characteristics of the spatial variation of the sound velocity from an analysis of the cluster structure of the timefront of the acoustic signal. In the particular case of a periodic perturbation, the structure of the timefront provides determination of the period of variation of the sound velocity. In a more general context, the proposed mechanism is related to inhomogeneity of the phase space and admits generalization to a wider class of perturbations, including those caused by internal waves with a continuous spectrum. Since the timefronts and the arrival time distributions of rays are measurable characteristics of the acoustic field, the possibility of determining parameters of the sound velocity variation from the results of such measurements is of interest both for the acoustic tomography of the ocean with remote sensing and for the basic theory of wave propagation in inhomogeneous media.

Acknowledgments. This study was supported by the Federal Targeted Program "Investigation into the Nature of the World Ocean," by the Russian Foundation for Basic Research (project no. 03-02-06896), and by the Program "Mathematical Methods in Nonlinear Dynamics" of the Russian Academy of Sciences.

REFERENCES

1. W. H. Munk and C. Wunsch, Deep-Sea Res. A **26**, 123 (1979).
2. V. A. Akulichev, V. V. Bezotvetnykh, S. I. Kamenev, *et al.*, Dokl. Akad. Nauk **381**, 243 (2001).
3. F. D. Tappert and Xin Tang, J. Acoust. Soc. Am. **99**, 185 (1996).
4. A. L. Virovlyansky, nlin.CD/0012015 (2001).
5. S. S. Abdullaev and G. M. Zaslavskiĭ, Usp. Fiz. Nauk **161** (8), 1 (1991) [Sov. Phys. Usp. **34**, 645 (1991)].
6. D. V. Makarov, S. V. Prants, and M. Yu. Uleysky, Dokl. Akad. Nauk **382**, 394 (2002).

Translated by P. Pozdeev

Technical Physics Letters, Vol. 29, No. 5, 2003, pp. 433–434. Translated from Pis'ma v Zhurnal Tekhnicheskoĭ Fiziki, Vol. 29, No. 10, 2003, pp. 77–81.

Longwave Generation in Laser Structures Based on InGaAs(N) Quantum Wells on GaAs Substrates

V. A. Odnoblyudov*, A. Yu. Egorov, A. R. Kovsh, V. V. Mamutin, E. V. Nikitina, Yu. M. Shernyakov, M. V. Maksimov, and V. M. Ustinov

Ioffe Physicotechnical Institute, Russian Academy of Sciences, St. Petersburg, 194021 Russia

** e-mail: vovaod@pop.ioffe.rssi.ru*

Received December 25, 2002

Abstract—The MBE growth regime has been optimized for the obtaining of laser structures based on InGaAs(N)/GaAs quantum wells (QWs) with high indium content. Structures containing InGaAs and InGaAsN isolated QWs exhibit low-threshold longwave emission at room temperature. Lasers based on QWs of the $In_{0.35}GaAs$ and $In_{0.35}GaAsN_{0.023}$ types are characterized by the radiation wavelengths λ = 1.085 and 1.295 μm at a threshold current density of 60 and 350 A/cm^2, respectively. © *2003 MAIK "Nauka/Interperiodica".*

Introduction. The effort of many research groups is presently devoted to the development of GaAs lasers operating in the region of wavelengths about 1.3 μm, which offer an alternative to lasers based on materials of the InGaAsP/InP system. It is expected that new GaAs lasers will provide cheaper base elements for telecommunication systems, thus leading to wider use of fiber optic lines in local computer networks. An important advantage of GaAs based structures over the indium phosphide analogs is the possibility of obtaining epitaxial structures for vertical-cavity surface-emitting lasers in a single technological cycle.

The main candidate materials for use in the active region of longwave GaAs based lasers are heterostructures with InGaAsN/GaAs quantum wells (QWs) and InAs/InGaAs quantum dots. Injection lasers of both stripe [1–3] and vertical-cavity surface-emitting [4, 5] geometry emitting at a wavelength of 1.3 μm were successfully obtained using heterostructures of both types.

However, the progress in the technology of growing laser structures with InGaAsN quantum wells emitting at 1.3 μm is rather contradictory, as evidenced by the significant scatter in published data. We believe that this problem is related to the fact that the growth of such QWs takes place under unfavorable conditions, differing from those typically employed for the obtaining of high-quality optical devices. Because of the high indium content in the QWs, the growth temperature has to be reduced so as to exclude switching of the growth mechanism from two-dimensional (lateral) to island type. Moreover, the addition of nitrogen (2–2.5%) favors an increase in the tendency to phase separation, despite a decrease in the lattice mismatch between matrix and QW [6]. In order to prevent the phase separation and maintain the desired lateral growth mechanism, the growth of the active region of a laser emitting at 1.3 μm has to be performed at a temperature not exceeding 440°C (which is almost 100°C lower than the temperature used for growing "standard" laser structures with $In_{0.18}GaAs$ quantum wells operating at 980 nm). Growth at such a low temperature can lead to a sharp increase in the concentration of impurities incorporated into the epitaxial layer and in the density of defects formed in this layer, thus dramatically impairing the optical and electrical properties of laser structures.

We have thoroughly analyzed and optimized the growth regime and the conditions of pretreatment of the growth chamber, so as to ensure the obtaining of low-threshold GaAs laser structures with the active regions grown at low temperatures. This allowed us to obtain lasers exhibiting record characteristics: a laser structure with $In_{0.35}GaAs$ quantum wells (grown at 440°C) was characterized by a minimum threshold current density of 60 A/cm^2 at a wavelength of 1085 nm; for a laser structure with QWs of the $In_{0.35}GaAsN_{0.023}$ (grown at 425°C), the corresponding characteristics were 350 A/cm^2 and 1295 nm.

Experimental. The sample structures were grown in a molecular beam epitaxy (MBE) system of the EP-1203 type equipped with an RF plasma nitrogen source (Epi Unibulb) and a solid-state source of arsenic. The active regions of lasers with $In_{0.35}GaAs$ and $In_{0.35}GaAsN_{0.023}$ quantum wells were grown at 440 and 425°C, respectively. Laser structures of both types contained 1.5-μm-thick $Al_{0.35}GaAs$ emitters and 0.5-μm-thick GaAs waveguides. The growth process was monitored by means of reflection high-energy electron diffraction (RHEED). The threshold current density was measured on samples with four cleaved edges.

Results and discussion. The spectra of electroluminescence measured using InGaAs(N)-QW laser structures with four cleaved edges are presented in the fig-

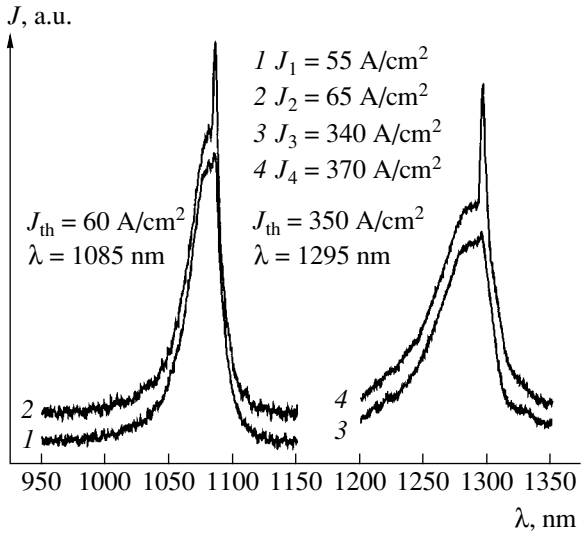

Electroluminescence spectra of GaAs based laser structures with (*1*, *2*) InGaAs and (*3*, *4*) InGaAsN quantum dots measured at current densities J below and above the lasing threshold J_{th}.

ure. The spectra were recorded at a current density below the threshold level (curves *1* and *3*) and after onset of the lasing regime (curves *2* and *4*). Curves *1* and *2* refer to a structure with $In_{0.35}GaAs$ quantum wells (laser No. 1), while curves *3* and *4* characterize a structure with $In_{0.35}GaAsN_{0.023}$ quantum wells (laser No. 2).

The threshold current density achieved with laser No. 1 (60 A/cm^2) is close to the best published results [7], which is evidence of almost absent nonradiative recombination in the laser structure studied. Thus, we have found growth regimes virtually eliminating the aforementioned negative effects during the low-temperature active region growth. In particular, a decrease in the undesired flux of arsenic during the QW growth probably reduced the number of point defects formed as a result of As incorporation into the interstitial sites. This effect plays a significant role during low-temperature growth (420–440°C), when the migration of Group III atoms over the surface of the growing film is suppressed.

Thus, laser No. 1 can serve as a base for growing nitrogen-containing laser structures. Adding 2.3% of nitrogen atoms into the active region ($In_{0.35}GaAs$) of laser No. 1 must shift the working wavelength from 1085 to 1300 nm. Previously [6], we demonstrated that the introduction of up to 2% of nitrogen atoms into the epitaxial layer at a certain plasma source operation regime does not significantly reduce the intensity of luminescence from the structures with QWs. We believe that the higher value of the threshold current density achieved in laser structures with InGaAsN quantum wells is due to a further decrease in the growth temperature and the possible presence of impurities in gaseous nitrogen. Laser No. 2 was grown under otherwise equal conditions with Laser No. 1, except for the temperature during the growth of $In_{0.35}GaAsN_{0.023}$ quantum wells being reduced to 425°C. This was necessary because adding nitrogen can stimulate the phase separation of indium-rich strained $In_{0.35}GaAs$ phase. Kageyama *et al.* [8] demonstrated that postgrowth annealing increases the optical characteristics of both InGaAs and compounds with low nitrogen content grown at low temperatures [8]. In our experiments, the active region was annealed during the growth of an upper emitter layer for 1.5 h at 700°C.

Thus, laser No. 2 reached a relatively low threshold current density of 350 A/cm^2. We believe that further progress in this direction can be achieved by more thoroughly purifying gaseous nitrogen from impurities (oxygen, carbon, water), by using other plasma source regimes during the growth, and by optimizing the active region composition with respect to In and N content in the quantum wells.

Conclusion. We have demonstrated low-threshold lasing in structures with InGaAs and InGaAsN quantum wells grown by low-temperature MBE. The complex approach to solving the problems encountered in the low-temperature growth (optimization of the growth conditions, use of ultrahigh purity materials, etc.) explains the achieved results and shows good prospects for further progress.

Acknowledgments. The work was supported by a grant from the Ministry of Science and Technology of the Russian Federation ("Physics of Solid State Structures" Program), by the Russian Foundation for Basic Research (project no. 02-02-17677), and by the NATO Science for Peace Program (Grant SfP 972484).

REFERENCES

1. V. M. Ustinov and A. E. Zhukov, Semicond. Sci. Technol. **15**, R41 (2000).
2. A. Yu. Egorov, B. Brenklau, B. Borchert, *et al.*, J. Cryst. Growth **227-228**, 545 (2001).
3. A. R. Kovsh *et al.*, Electron. Lett. **38**, 1104 (2002).
4. N. A. Maleev, A. Yu. Egorov, A. E. Zhukov, *et al.*, Fiz. Tekh. Poluprovodn. (St. Petersburg) **35**, 881 (2001) [Semiconductors **35**, 847 (2001)].
5. J. A. Lott, N. N. Ledentsov, V. M. Ustinov, *et al.*, Electron. Lett. **36**, 1384 (2000).
6. A. R. Kovsh *et al.*, J. Vac. Sci. Technol. B **20**, 1158 (2002).
7. N. Chand *et al.*, Appl. Phys. Lett. **58**, 1704 (1991).
8. T. Kageyama, T. Miyamoto, Sh. Makino, *et al.*, Jpn. J. Appl. Phys., Part 2 **38**, L298 (1999).

Translated by P. Pozdeev

Technical Physics Letters, Vol. 29, No. 5, 2003, pp. 435–437. Translated from Pis'ma v Zhurnal Tekhnicheskoĭ Fiziki, Vol. 29, No. 10, 2003, pp. 82–87.

Deterministic Noise in Vanadium Dioxide Based Structures

A. A. Velichko*, G. B. Stefanovich, A. L. Pergament, and P. P. Boriskov

Petrozavodsk State University, Petrozavodsk, Karelia, Russia

** e-mail: velichko@mainpgu.karelia.ru*

Received December 25, 2002

Abstract—We present experimental data on the low-frequency noise in vanadium dioxide based sandwich and planar structures possessing negative differential resistance. It is established that the noise spectrum obeys the $1/f^{\alpha}$ law and the values of coefficient α for the sandwich structure are experimentally determined for the first time. The regions of switching in the current–voltage characteristics of structures of both types exhibit a noise possessing the character of deterministic chaos. © *2003 MAIK "Nauka/Interperiodica".*

As is known [1], approaching the region of instability of a homogeneous state in a system featuring the metal–insulator phase transition may be accompanied by low-frequency fluctuations analogous to the turbulent flow oscillations in hydrodynamics, alternatively referred to as deterministic chaos. The extensive investigation of noise in the structures based on transition metal oxide films is explained both by the prospects of using the steep temperature dependence of the physical properties of these structures, as well as by the basic interest in the physics of such phase transitions.

A large proportion of investigations devoted to the metal–insulator phase transition in vanadium dioxide (VO_2) was concentrated on the switching effect, which provides information on the phenomenon of interest and determines the practical applications of this material [2]. Electric switching in VO_2, related to the metal–insulator phase transition, was observed in single crystal samples [3], planar thin-film structures [4], sandwich structures of the V–VO_2–metal type [5], and in various other systems containing VO_2 layers [6, 7].

In most studies of noise in VO_2 based structures, the main attention is given to determining the noise spectrum [4, 8]. At the same time, it would be of interest to analyze the noise in such systems by methods on nonlinear dynamics, in particular, to estimate the fractal dimension of the attractor of noise oscillations. This would indicate whether the noise is stochastic or deterministic and, in combination with the results of spectral analysis, elucidate the physical mechanism of this noise.

The method of manufacturing sandwich switches based on amorphous VO_2 was described previously [9]. The main switching channel is composed of vanadium dioxide possessing a crystalline structure. A typical current–voltage characteristic (*I–U* curve) of the switching sandwich structure is presented in Fig. 1a. A planar switch had the form of a polycrystalline VO_2 film deposited by reactive magnetron sputtering [10] onto a sapphire substrate and provided with aluminum contacts. The *I–V* curves of such samples (Fig. 1b) were measured using a conventional four-point-probe technique.

The phenomenon of switching in VO_2 based structures at room temperature is usually explained in terms

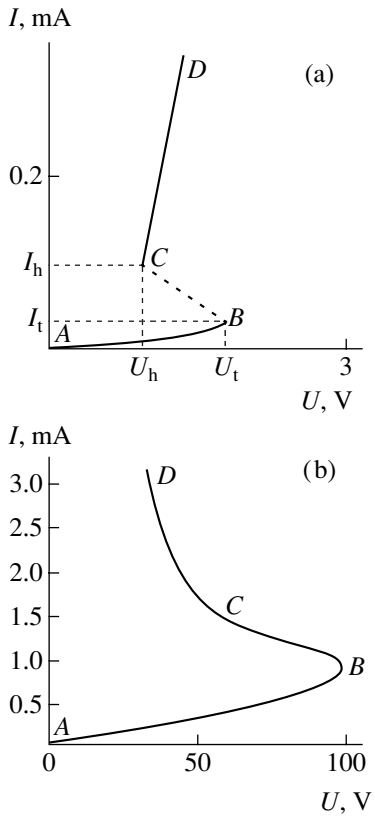

Fig. 1. The current–voltage characteristics of (a) sandwich and (b) planar VO_2 based switching structures: U_t, I_t are the threshold (switching) voltage and current; U_h, I_h are the holding voltage and current, respectively.

1063-7850/03/2905-0435$24.00 © 2003 MAIK "Nauka/Interperiodica"

The parameters of noise in VO_2 based switching structures

Sandwich switch					
Region	1	2	3	4	5
I, μA	10	30	–	100	200
α	1.3	1.2	–	0.2	1
D	∞	5	–	2.4	∞
Planar switch					
Region	1	2	3	4	5
I, mA	0.2	1	1.5	–	3
α	1.28	1.77	1.6	–	1.2
D	∞	2.3	2.2–2.8	–	∞

of the critical temperature model [2]. According to this, the Joule heating of the material by the current up to the metal–insulator transition temperature leads to a jump in the conductivity, which accounts for the appearance of a negative differential resistance (NDR) region in the current–voltage characteristic (S-shaped *I–U* curve). The *I–U* curve of a sandwich switch can be divided into five characteristic regions (Fig. 1a): (1) high-ohmic state (region *AB*); (2) high-ohmic subthreshold state in the vicinity of point *B*; (3) NDR region (*BC*); (4) low-ohmic subthreshold state upon switching (in the vicinity of point *C*); and (5) low-ohmic state upon switching (region *CD*). The same conditional subdivision of the *I–V* curve can be accepted for the *I–U* curve of a planar structure (see Fig. 1b).

We have measured (in the digital form) the noise in all regions of the *I–V* curves, except region 3 for the sandwich switch (which is characterized by unstable working point) and region 4 for the planar switch (which exhibits no distinct boundary between regions 3 and 5). The measurements were performed in a frequency range from 10 to 10^3 Hz.

The fractal dimensions of attractors for the observed noise oscillations were estimated upon calculating the correlation integral [11]

$$C(r) = \lim \frac{1}{N^2} \sum_{i=1}^{N} \sum_{j=1}^{N} H(r - |x_i - x_j|),$$
$$N \longrightarrow \infty \ (i \neq j),$$

where r is the cell size of the phase space subdivision, $N = 10000$ is the number of points in the initial time series, H is the Heaviside function [$H(s) = 1$ for $s > 0$ and $H(s) = 0$ for $s < 0$], $x_i = x(i\Delta t)$, and Δt is the discretization step. The fractal dimension D of the space of attractor embeddings was estimated from the slope of a linear portion of the plot of $\ln C(r)$ versus $\ln(r)$. Note that $N_0 \geq \text{int}|D| + 1$ determines the number of differential equations of the first order necessary for the physical description of behavior of the dynamic system under consideration. For a stochastic (nondeterministic) noise, the slope of $\ln C(r) = f[\ln(r)]$ does not reach saturation and the corresponding dimension is taken equal to infinity.

In all regions of the *I–U* curves, the spectrum of noise is described well by the $1/f^{\alpha}$ law. The results of determination of the α and D values in this relation for various currents I (corresponding to the five characteristic regions of the *I–V* curves) are presented in the table.

In region 1, the coefficients α for both sandwich and planar switches agree well with the analogous values measured for small currents in single crystals [4] and polycrystalline VO_2 films [8, 12]. The excess low-frequency noise in the this region has a stochastic character and is related to the structural defects [12].

The value of α in region 5 is lower than that in region 1, which is typical of noise observed in the presence of a phase with metallic conductivity [4]. This noise also shows no signs of deterministic chaotic behavior.

In the low-ohmic subthreshold region of the *I–U* curve (region 4), the fractal dimension of the attractor is finite. At all probability, a relatively small excess stochastic noise related to resistance of the low-ohmic channel part is supplemented by an additional noise from a source possessing a deterministic chaos nature. The physical mechanism of these oscillations can be related to the chaotic pulsation and random walk of current filaments formed in a subthreshold switching region. One possible source of the deterministic chaotic noise in this case is the generation–recombination effects in combination with transverse diffusion in S-shaped NDR regions [1]. We also believe that, in a sandwich switch, the current fluctuations are more likely related to an instability of the metal–insulator transition as such. This is evidenced by an anomalous value of $\alpha \approx 0.2$, which is consistent neither with the spectrum of noise caused by the generation–recombination effects [13] nor with recently reported determin-

istic character of chaotic oscillations in the resistance of VO_2 films within the hysteresis loop [14].

For the sandwich switch, the D and α values in region 2 are greater than the corresponding values in region 4, which is indicative of a greater contribution due to the stochastic noise component. For the planar switch, the noise in the region of pronounced NDR (regions 2 and 3) is deterministic with $D = 2.2–2.8$. Based on the data reported in [15], where the crystalline VO_2 films were found to possess a domain structure in the vicinity of the metal–insulator phase transition, we may suggest that the aforementioned noise possessing the character of deterministic chaos is due to these very domains moving between electrodes [4]. The domains can form as a result of the generation–recombination instability, which is confirmed by the value of $\alpha \approx 2$ [13].

Acknowledgments. This study was supported by the Ministry of Education of the Russian Federation (project no. PD02-1.2-183) and by the U.S. Civilian Research and Development Foundation for Independent States of the Former Soviet Union (CRDF Award No. PZ-013-02).

REFERENCES

1. E. Shöll, *Nonequilibrium Phase Transitions in Semiconductors: Self-Organization Induced by Generation and Recombination Processes* (Springer-Verlag, Heidelberg, 1987; Mir, Moscow, 1991).
2. A. A. Bugaev, B. P. Zakharchenya, and F. A. Chudnovskiĭ, *Metal–Semiconductor Phase Transition and Its Applications* (Nauka, Leningrad, 1979).
3. A. Mansingh and R. Singh, J. Phys. C **13**, 5725 (1980).
4. A. Alekseyunas, V. Bareĭkis, V. Bondarenko, and Yu. Liberis, Fiz. Tverd. Tela (Leningrad) **20**, 1980 (1978) [Sov. Phys. Solid State **20**, 1143 (1978)].
5. R. L. Remke, R. M. Walser, and R. W. Bene, Thin Solid Films **97**, 129 (1982).
6. G. P. Vasil'ev, I. A. Serbinov, and L. A. Ryabova, Pis'ma Zh. Tekh. Fiz. **3** (8), 342 (1977) [Sov. Tech. Phys. Lett. **3**, 179 (1977)].
7. J. K. Higgins, B. K. Temple, and J. E. Lewis, J. Non-Cryst. Solids **23**, 187 (1977).
8. V. N. Andreev, B. P. Zakharchenya, Yu. S. Kapshin, *et al.*, Zh. Éksp. Teor. Fiz. **79**, 1353 (1980) [Sov. Phys. JETP **52**, 684 (1980)].
9. F. A. Chudnovskii and G. B. Stefanovich, J. Solid State Chem. **98**, 137 (1992).
10. A. L. Pergament and G. B. Stefanovich, Thin Solid Films **322**, 33 (1998).
11. F. Mun, *Chaotic Vibrations. An Introduction for Applied Scientists and Engineers* (Wiley, New York, 1987; Mir, Moscow, 1990).
12. M. V. Baĭdakova, A. V. Bobyl', V. G. Malyarov, *et al.*, Pis'ma Zh. Tekh. Fiz. **23** (13), 58 (1997) [Tech. Phys. Lett. **23**, 520 (1997)].
13. B. I. Yakubovich, *Electric Fluctuations in Nonmetallic Materials* (Énergoatomizdat, St. Petersburg, 1999).
14. L. A. L. De Almedia, G. S. Deep, A. M. N. Lima, and H. Nef, Appl. Phys. Lett. **77**, 4365 (2000).
15. B. Fisher, J. Phys. C **9**, 1201 (1976).

Translated by P. Pozdeev

Technical Physics Letters, Vol. 29, No. 5, 2003, pp. 438–440. Translated from Pis'ma v Zhurnal Tekhnicheskoĭ Fiziki, Vol. 29, No. 10, 2003, pp. 88–94.

String Wave Spraying of Liquid

V. A. Aleksandrov

Institute of Applied Mechanics, Ural Division, Russian Academy of Sciences, Izhevsk, Udmurtia, Russia
e-mail: ipm@ipm.uni.udm.ru

Received December 16, 2002

Abstract—It is established that an impact-excited string partly immersed into a liquid at an angle to its surface produces wave transport and spraying of the liquid. The liquid is sprayed from some regions on the string excited at definite frequencies. A law governing the conditions of liquid spraying is found and explained in terms of the phase difference between transverse and longitudinal waves in various regions of the oscillating string. *© 2003 MAIK "Nauka/Interperiodica".*

The spraying of liquids by means of acoustic oscillations in the audio and ultrasonic frequency ranges [1] is usually performed with devices comprising a piezoceramic actuator and a spraying unit, the latter typically representing a plate, membrane, or flange [2]. Such a design hinders using these devices for the spraying of liquids capable of producing physical or chemical action upon the piezoelectric transducer.

This paper reports on the results of investigation of the interaction of a metal string with water. The string, partly immersed into the liquid medium at an angle to its surface, is excited by impact from a source not contacting directly with water. The impact excitation of a string is of interest because this mode of action allows both longitudinal and transverse waves to be excited, thus providing for the wave transport of the particles of the medium contacting with the string [3, 4].

The experiments were performed with a simple device comprising a metal string with a diameter of 0.62 mm and a length of L = 200 mm fixed in a metal (D16 duralumin) case with dimensions 220 × 15 × 3 mm. The string, made of 20Kh80N nichrome with a density of $\rho = 8.2 \times 10^3$ kg/m^3 and a Young modulus of $E = 228 \times 10^9$ Pa, was stretched with a tension force of F = 134 N. Impact excitation of the string was provided by a piezoelectric transducer (ZP-4 type) mounted in the 1-mm-wide gap between string and case, at a distance of 20 mm from the upper end of the string (Fig. 1). To study the interaction of the impact-excited string with a liquid medium, the device was partly immersed into water at an angle of 15°–45° to its surface. The piezoelectric transducer was excited with an electric signal of 60 V amplitude from a low-frequency generator.

The experiments showed that the string, partly immersed into liquid to a certain depth and excited by the piezoelectric actuator at a definite frequency, produces a vibrational-wave transport and spraying of water (Fig. 1). The most intensive spraying takes place when less than half of the string is immersed into liquid. Water is supplied from an area of the liquid surface confined between case and string and is transported in an 0.1–0.3 mm thick layer up along the string. Upon reaching a certain region of the string spaced 5–10 mm from the liquid surface, water is sprayed in the form of small droplets sized 10–40 μm. When the string is immersed to a depth of 8–12 mm, two regions of spraying spaced by 2–4 mm are observed. The spraying efficiency with a power supply of 0.6 W at a frequency of 4024 Hz was 300 cm^3/h.

The distance from the excitation source to spraying region was determined to within 0.5 mm. The spraying ceased when the frequency of the electric signal applied to the piezoelectric transducer was changed by more than ±3 Hz. The working frequencies of the piezoelectric transducer and the distances from this excitation source to various regions of the string from which effective spraying takes place are listed in the table below.

Effective string wave spraying parameters

m	0	1	2	3	4	5
f_m, Hz	3810	3862	3911	3951	3988	4024
x_m, mm	16	46	76	106	135	164(161)

1063-7850/03/2905-0438$24.00

Processing of these data showed that the oscillation frequencies and distances from the excitation source to spraying regions obey a simple relationship:

$$f_{m+n}x_{m+n}/f_m x_m = 1 + 2n/(2m+1). \quad (1)$$

This relation can be explained as follows. Impact excitation of a string gives rise to two pairs of longitudinal and transverse waves simultaneously outgoing from the point of impact and propagating along the string with the velocities $v_\xi = (E/\rho)^{1/2}$ and $v_\eta = (F/\rho S)^{1/2}$, where E is the Young modulus and ρ is the density of the string material, F is the string tension, and S is the string cross section area. Each pair of the longitudinal and transverse waves (denoted by subscripts ξ and η, respectively) is described by the following expressions;

$$\xi(t) = A_\xi \cos(\omega t + k_\xi x + \varphi_0), \quad (2)$$

$$\eta(t) = A_\eta \cos(\omega t + k_\eta x + \varphi_0), \quad (3)$$

where A_ξ and A_η are the amplitudes, ω is the common circular frequency, k_ξ and k_η are the wavenumbers, and φ_0 is the initial phase.

Oscillations at an arbitrary point of the string a given distance x from the source can be represented as a sum of longitudinal and transverse waves at this point, which obeys an expression corresponding to elliptically polarized oscillations:

$$[\xi^2(t)/A_\xi^2] + [\eta^2(t)/A_\eta^2] - [2\xi(t)\eta(t)/A_\xi A_\eta] \times \cos(k_\eta - k_\xi)x = \sin^2(k_\eta - k_\xi)x. \quad (4)$$

Here, the argument $(k_\eta - k_\xi)x$ represents the phase difference $\Delta\Phi$ of the longitudinal and transverse waves at the point of observation. Taking into account the relations $k_\eta = \omega/v_\eta$, $k_\xi = \omega/v_\xi$, and $\omega = 2\pi f$, where f is the source (and wave) frequency, this phase difference can be expressed as

$$\Delta\Phi = 2\pi[(1/v_\eta) - (1/v_\xi)]fx. \quad (5)$$

As can be seen from this formula, the phase difference between the longitudinal and transverse waves simultaneously propagating along the string depends on the frequency and the distance from the excitation source to the observation point. At a fixed frequency, the distance between two points of the string with given phase differences can be determined as

$$x_2 - x_1 = (\Delta\Phi_2 - \Delta\Phi_1)/2\pi[(1/v_\eta) - (1/v_\xi)]f. \quad (6)$$

At some frequencies, the phase difference between longitudinal and transverse waves in various regions of the string can acquire definite values determining the shape of oscillations in these regions (Fig. 2). For example, $\Delta\Phi = (2m+1)\pi/2$ ($m = 0, 1, 2, \ldots$) corresponds to an ellipse with one semiaxis oriented along the string and the other, perpendicular to the string:

$$[\xi^2(t)/A_\xi^2] + [\eta^2(t)/A_\eta^2] = 1. \quad (7)$$

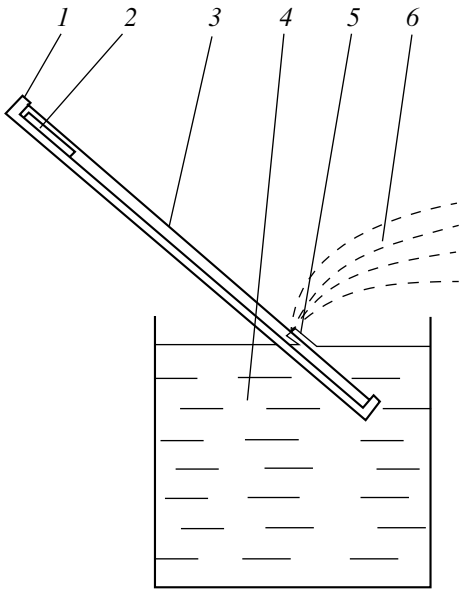

Fig. 1. Schematic diagram illustrating water spraying by an oscillating string: (*1*) metal case; (*2*) piezoelectric transducer; (*3*) metal string; (*4*) water; (*5*) transported liquid layer; (*6*) aerosol.

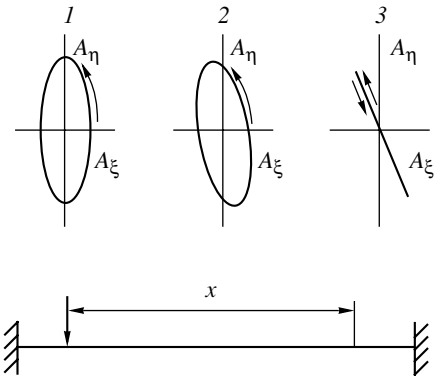

Fig. 2. Oscillations in various regions of the string for certain values of the phase difference between longitudinal and transverse waves: (*1*) $\Delta\Phi = (2m+1)\pi/2$; (*2*) $\Delta\Phi = [(2m+1)\pi/2] + \pi/4$; (*3*) $\Delta\Phi = m\pi$.

When the phase difference between longitudinal and transverse waves is $\Delta\Phi = [(2m+1)\pi/2] \pm \pi/4$, both semiaxes make oblique angles to the string, and at $\Delta\Phi = m\pi$, the ellipse degenerates into straight segments sloped at an angle of $\varphi = \arctan[(A_\eta/A_\xi)\cos m\pi]$.

Under the conditions of oscillations with $\Delta\Phi = (2m+1)\pi/2$ for various m, the ratio of phase differences of the longitudinal and transverse waves is

$$\Delta\Phi_{m+n}/\Delta\Phi_m = 1 + 2n/(2m+1). \quad (8)$$

Substituting expression (5) into this formula yields relation (1) between the experimentally determined

excitation source frequencies and distances to the regions of spraying.

From this we conclude that the experimentally observed phenomenon of spraying arises in certain regions of the string excited at frequencies such that the phase difference between longitudinal and transverse waves for these regions amounts to $\Delta\Phi = (2m + 1)\pi/2$.

Another necessary condition for the liquid spraying is the vibrational-wave transport of liquid from the surface to the regions of spraying. Using the experimentally determined distances from the surface of water to these regions (Δx = 5–10 mm), it is possible to estimate the phase differences between longitudinal and transverse waves for the string region occurring immediately on the surface. Using Eq. (6), we obtain for this region

$$\Delta\Phi = (1 + \Delta x/x_m)(2m + 1)\pi/2. \quad (9)$$

This value differs from that for the phase difference between longitudinal and transverse waves in the region of spraying by the factor $\Delta\varphi = (\Delta x/x_m)(2m + 1)\pi/2$. The experimental values of this factor fall within $(0.16–0.33)\pi$, the average being $\Delta\varphi = \pi/4$. Then, the phase difference between longitudinal and transverse waves for a string region near the surface under the conditions of vibrational-wave water transport obeys the relation $\Delta\Phi = [(2m + 1)\pi/2] \pm \pi/4$.

Under the experimental conditions studied, water spraying from the string was observed within a rather narrow interval of frequencies from 3810 to 4024 Hz. The distance between the regions from which spraying took place was about 30 mm. According to the formula $\lambda_\eta = v_\eta/f$, the transverse wavelength for the above frequencies is about 60 mm. The same value is obtained for all six regions of spraying observed over a 180-mm-long part of the string between the excitation source and the string end, provided that this length accommodates three transverse wavelengths. This result is indicative of the resonance character of the transverse oscillations in the string, the resonance peaks corresponding to the regions of liquid spraying. As the frequency changes in the vicinity of resonance values, the phase difference between longitudinal and transverse waves reaches the value $\Delta\Phi = \pi/2$ sequentially in each of these maxima.

The appearance of the second region of spraying at a distance of x_5 = 161 mm observed for f_5 = 4024 Hz is related to the formation of a longitudinal standing wave with $\lambda_\xi = 6L$ as a result of interference of the two counterpropagating waves. One antinode of this standing wave coincides with the source, while the second antinode is at a distance of x = 160 mm from the source. The antinodes feature local deformation of the string at the wave frequency. This gives rise to radial oscillations of the string, whereby the energy is transferred to liquid particles (provided that a layer of liquid is present on the string). The wavelength and velocity of the longitudinal wave determined for the given string are λ_ξ = 1200 mm and v_ξ = 4828 m/s, respectively. The difference between this longitudinal wave velocity and that determined from the Young modulus (v_ξ = 5273 m/s) is probably related to a dispersion caused by the transverse oscillations of the string.

Thus, the experimentally observed wave transport and spraying of liquid by an oscillating string is caused by the impact excitation of the string, which gives rise to longitudinal and transverse waves simultaneously propagating along the string. The relation between the parameters of oscillations corresponding to the liquid spraying by the string is explained by variation of the phase difference between longitudinal and transverse waves along the string. The regions where this phase difference is $\Delta\Phi = [(2m + 1)\pi/2] \pm \pi/4$ account for the wave transport of liquid, while the regions in which $\Delta\Phi = (2m + 1)\pi/2$ produce spraying of this liquid. The results of this investigation can be used in practice for the development of devices spraying various liquids.

REFERENCES

1. *Ultrasound: Concise Encyclopedia*, Ed. by I. P. Golyamina (Sov. Éntsiklopediya, Moscow, 1979).
2. *Vibrational Motion Converters* (Mashinostroenie, Leningrad, 1984).
3. *Vibrations in Technology: Handbook* (Mashinostroenie, Moscow, 1981), Vol. 4.
4. V. A. Aleksandrov, Datchiki Sist., No. 6, 35 (2001).

Translated by P. Pozdeev